Antiferromagnetic order and spin dynamics in iron-based superconductors

Pengcheng Dai*

Department of Physics and Astronomy, Rice University, Houston, Texas 77005, USA

(published 20 August 2015)

High-transition temperature (high-T_c) superconductivity in the iron pnictides or chalcogenides emerges from the suppression of the static antiferromagnetic order in their parent compounds, similar to copper oxide superconductors. This raises a fundamental question concerning the role of magnetism in the superconductivity of these materials. Neutron scattering, a powerful probe to study the magnetic order and spin dynamics, plays an essential role in determining the relationship between magnetism and superconductivity in high-T_c superconductors. The rapid development of modern neutron time-of-flight spectrometers allows a direct determination of the spin dynamical properties of iron-based superconductors throughout the entire Brillouin zone. In this paper, an overview is presented of the neutron scattering results on iron-based superconductors, focusing on the evolution of spin-excitation spectra as a function of electron and hole doping and isoelectronic substitution. Spin dynamical properties of iron-based superconductors are compared with those of copper oxide and heavy fermion superconductors and the common features of spin excitations in these three families of unconventional superconductors and their relationship with superconductivity are discussed.

DOI: 10.1103/RevModPhys.87.855 PACS numbers: 74.25.Ha, 74.25.Jb, 78.70.Nx

CONTENTS

I. INTRODUCTION

The interplay between magnetism and superconductivity has a long history. For example, it is well known that superconductivity in conventional Bardeen-Cooper-Schrieffer (BCS) superconductors (Bardeen, Cooper, and Schrieffer, 1957) such as the element lanthanum can be suppressed by as little as 1% gadolinium substitution as magnetic impurity (Mathias, Suhl, and Corenzwit, 1958). Within the BCS framework, magnetic impurities can act as pairing breaking agents rapidly suppressing superconductivity (Balatsky, Vekhter, and Zhu, 2006). In the case of unconventional superconductors such as heavy fermions (Steglich *et al.*, 1979; Stewart, 2001; Gegenwart, Si, and Steglich, 2008), copper oxides (Bednorz and Müller, 1986; Lee, Nagaosa, and Wen, 2006), and iron pnictides or chalcogenides (Kamihara *et al.*, 2006, 2008; Hsu *et al.*, 2008; Canfield and Bud'ko, 2010; Johnston, 2010; Paglione and Greene, 2010; Stewart, 2011; Wen *et al.*, 2011), the observation that superconductivity always appears near static antiferromagnetic (AF) order (Uemura, 2009) suggests that magnetism may be a common thread for understanding the microscopic origin of unconventional superconductors and high-transition temperature (high-T_c) superconductivity (Scalapino, 2012). Based on this premise, much work has focused on studying the interplay between magnetism and superconductivity, particularly the high-T_c copper oxide superconductors (cuprates) since its discovery in 1986 (Kastner *et al.*, 1998; Kivelson *et al.*, 2003; Armitage, Fournier, and Greene, 2010; Fujita *et al.*, 2012; Tranquada, Xu, and Zaliznyak, 2014). Although

*pdai@rice.edu

understanding the magnetism and its relationship with superconductivity in cuprates is still an area of active research (Fujita *et al.*, 2012; Tranquada, Xu, and Zaliznyak, 2014), the discovery of AF order in the parent compounds of iron-based superconductors in 2008 (Huang, Qiu *et al.*, 2008; Zhao *et al.*, 2008b; de la Cruz *et al.*, 2008) provided a new opportunity to study the interplay between magnetism and superconductivity. There are already several review articles summarizing the general progress in the field of iron-based superconductors (Canfield and Bud'ko, 2010; Johnston, 2010; Mazin, 2010; Paglione and Greene, 2010; Hirschfeld, Korshunov, and Mazin, 2011; Stewart, 2011; Wang and Lee, 2011; Wen *et al.*, 2011; Chubukov, 2012; Dagotto, 2013). The interplay between magnetism and superconductivity studied by neutron scattering has been briefly discussed as well (Lumsden and Christianson, 2010; Dai, Hu, and Dagotto, 2012).

The purpose of this review is to present a comprehensive account of the AF order, spin excitations, and their relationship with superconductivity in iron pnictides and chalcogenides. Since magnetism is generally believed to play an important role in the electron pairing mechanism of high-T_c superconductivity (Scalapino, 2012), it is important to summarize the progress in the field over the past several years and compare the outcome with previous work on high-T_c copper oxides and heavy fermion superconductors. Neutrons, with their wavelengths comparable to the atomic spacing and their spins directly probing the unpaired electrons in solids, have played a unique role in determining the magnetic properties of high-T_c superconductors. Soon after the discovery of iron pnictide superconductor $LaFeAsO_{1-x}F_x$ with $T_c =$ 26 K (Kamihara *et al.*, 2008), neutron and x-ray scattering experiments discovered that its parent compound LaFeAsO exhibits a tetragonal-to-orthorhombic structural distortion followed by a collinear AF order (Nomura *et al.*, 2008; de la Cruz *et al.*, 2008). Since the presence of a collinear AF structure in LaFeAsO was predicted earlier in band structure calculations as due to a spin-density-wave order arising from nesting of the hole and electron Fermi surfaces (Dong *et al.*, 2008), its confirmation by neutron scattering and the semimetallic nature of these materials (Kamihara *et al.*, 2008) provided strong evidence for the itinerant origin of the magnetism in the iron-based superconductors (Mazin, 2010; Hirschfeld, Korshunov, and Mazin, 2011). This is fundamentally different from the parent compounds of copper oxide superconductors, which are Mott insulators because the Coulomb repulsive energy cost U of having two electrons (or holes) on the same site is much larger than the electron hopping energy t (Lee, Nagaosa, and Wen, 2006). For a Mott insulator, the static AF order arises from a savings in energy of $4t^2/U$ via virtual hopping and is due to electron correlation effects. Since the Mott insulating state of copper oxides is believed to play an essential role in the pseudogap physics and mechanism of high-T_c superconductivity (Lee, Nagaosa, and Wen, 2006), it is interesting to ask whether iron-based superconductors are also close to a Mott insulator and determine the effect of electron correlations and local moments to their electronic properties and spin dynamics (Fang *et al.*, 2008; Haule, Shim, and Kotliar, 2008; Si and Abrahams, 2008; Xu, Müller, and Sachdev, 2008; Qazilbash *et al.*, 2009).

From the experimental point of view, a systematic determination of the magnetic structures and the doping evolution of spin excitations in different classes of iron-based superconductors and their associated materials will form the basis to establish whether magnetism is responsible for high-T_c superconductivity. For copper oxides, superconductivity can be induced by charge carrier doping (electrons or holes) into the CuO_2 plane, resulting in complicated phase diagrams with many incipient states competing with superconductivity (Kastner *et al.*, 1998; Kivelson *et al.*, 2003; Armitage, Fournier, and Greene, 2010; Fujita *et al.*, 2012; Tranquada, Xu, and Zaliznyak, 2014). The undoped copper oxides such as La_2CuO_4 (Vaknin *et al.*, 1987) and $YBa_2Cu_3O_{6+x}$ (Tranquada *et al.*, 1988) are simple antiferromagnets with neighboring spins oppositely aligned. When holes are doped into the parent compounds, the static AF order is gradually suppressed, but spin excitations (or short-range spin fluctuations) survive across the entire superconducting dome and couple with superconductivity via a collective magnetic excitation termed the neutron spin resonance (Eschrig, 2006; Fujita *et al.*, 2012; Tranquada, Xu, and Zaliznyak, 2014). However, inelastic neutron scattering experiments designed to study the doping evolution of spin excitations were carried out only on the $La_{2-x}Sr_xCuO_4$ family of cuprates across the entire phase diagram from the undoped parent compound to heavily overdoped nonsuperconducting samples (Lipscombe *et al.*, 2007; Wakimoto *et al.*, 2007). There are no comprehensive measurements throughout the entire phase diagram on other cuprates due to material limitations (for example, $YBa_2Cu_3O_{6+x}$ cannot be hole overdoped to completely suppress superconductivity) or the difficulty in growing large single crystals suitable for inelastic neutron scattering experiments.

In the case of iron-based superconductors, there are two major classes of materials, the iron pnictides and iron chalcogenides (Johnston, 2010; Stewart, 2011). Compared with the hole-doped $La_{2-x}Sr_xCuO_4$ copper oxide superconductors, where superconductivity can be induced only via substituting the trivalent La by the divalent element Ba or Sr, superconductivity in iron pnictides such as $BaFe_2As_2$ (Rotter *et al.*, 2008) can be induced by ionic substitution at any element site. These include Ba by K/Na to form hole-doped $Ba_{1-x}K_xFe_2As_2$ (Rotter, Tegel, and Johrendt, 2008; Pramanik *et al.*, 2011), Fe by Co or Ni to have electron-doped $BaFe_{2-x}T_xAs_2$ ($T =$ Co, Ni) (Sefat *et al.*, 2008; L. J. Li *et al.*, 2009), and As by P in the isovalent (or isoelectronic) doped compounds $BaFe_2As_{2-x}P_x$ (Jiang *et al.*, 2009). While K or Na doping to $BaFe_2As_2$ induces the same numbers of holes to the FeAs layer, the effect of Ni doping is expected to introduce twice the number of electrons into the FeAs layer as that of Co doping from a naïve electron counting point of view (Johnston, 2010; Stewart, 2011). Since large sized single crystals can be grown by self-flux methods in many of these cases (Canfield and Bud'ko, 2010), doped $BaFe_2As_2$ materials provide a unique opportunity to study the evolution of the static AF order and spin excitations as a function of hole, electron, and isovalent doping throughout the entire phase diagram spanning the superconductivity dome, and determine their connection with superconductivity. These experiments, together with neutron scattering studies of related materials

(Ishikado *et al.*, 2009; Singh *et al.*, 2009; Shamoto *et al.*, 2010; Wakimoto *et al.*, 2010; Johnston *et al.*, 2011; Kim *et al.*, 2011; Marty *et al.*, 2011; Simonson *et al.*, 2012; Inosov *et al.*, 2013; Lamsal *et al.*, 2013; Taylor *et al.*, 2013), will establish the common features in the magnetic order and spin excitations in different families of iron-based superconductors. The outcome, together with the results from high-T_c copper oxide and heavy fermion superconductors, can form a basis to determine if magnetism is indeed responsible for superconductivity in these materials (Scalapino, 2012).

Compared with other techniques suitable to study magnetism in solids including muon spin rotation (μSR) (Uemura, 2009; Carretta *et al.*, 2013), nuclear magnetic resonance (NMR) (Alloul *et al.*, 2009), and resonant inelastic x-ray scattering (RIXS) (Ament *et al.*, 2011), neutron scattering has several unique advantages: (1) The neutron itself is a charge 0 fermion with a spin $S = 1/2$, resulting in a magnetic dipole moment which can interact with unpaired electrons and magnetism in solids; (2) the charge neutrality of the neutron renders it a weakly interacting probe with well-known scattering cross sections; and (3) the available wavelength and energies of neutrons as a scattering probe are ideally suited to study static magnetic order and spin excitations in solids. The general scattering principle involved is simply to measure the number of neutrons scattered into a given solid angle at a known energy ($E = \hbar\omega$, where $\hbar$ is the reduced Planck's constant and ω is the angular frequency) and momentum transfer ($\mathbf{Q}$). The laws of conservation of momentum and energy are satisfied via $\mathbf{Q} = \mathbf{k}_i - \mathbf{k}_f$ and $E = \hbar\omega = E_i - E_f$, where k_i, $E_i = \hbar^2 k_i^2/2m$, k_f, and $E_f = \hbar^2 k_f^2/2m$ are the incident neutron wave vector, energy, outgoing neutron wave vector, and energy, respectively, and m is the mass of a neutron. The coherent magnetic scattering cross section from a system with a single species of magnetic atoms is then (Xu, Xu, and Tranquada, 2013)

$$\frac{d^2\sigma}{d\Omega dE} = \frac{N}{\hbar}\frac{k_f}{k_i} p^2 e^{-2W} \sum_{\alpha,\beta} (\delta_{\alpha,\beta} - \tilde{Q}_\alpha \tilde{Q}_\beta) S^{\alpha\beta}(\mathbf{Q},\omega).$$

Here N is the number of unit cells, $p = (\gamma r_0/2)^2 g^2 f(\mathbf{Q})^2$ [where $\gamma r_0/2 = 0.2695 \times 10^{-12}$ cm, $g \approx 2$ is the Landé electron spin g factor, and $f(\mathbf{Q})$ is the magnetic form factor], e^{-2W} is the Debye-Waller factor, α, β are the Cartesian coordinates x, y, and z, and $\tilde{Q}_\alpha$, $\tilde{Q}_\beta$ are the projections of the unit wave vector $\tilde{Q}$ onto the Cartesian axes. $S^{\alpha\beta}(\mathbf{Q},\omega)$ is the dynamic spin correlation function and is associated with the imaginary part of the dynamic susceptibility $\chi''_{\alpha\beta}(\mathbf{Q},\omega)$ via the fluctuation-dissipation theorem:

$$\chi''_{\alpha\beta}(\mathbf{Q},\omega) = g^2 \mu_B^2 \frac{\pi}{\hbar}(1 - e^{-\hbar\omega/k_B T}) S^{\alpha\beta}(\mathbf{Q},\omega).$$

For a paramagnet with isotropic spin excitations, $S^{xx}(\mathbf{Q},\omega) = S^{yy}(\mathbf{Q},\omega) = S^{zz}(\mathbf{Q},\omega)$. Since neutron scattering is sensitive only to the spin (fluctuations) direction perpendicular to the wave vector transfer $\mathbf{Q}$, $S(\mathbf{Q},\omega)$ of an isotropic paramagnet measured by unpolarized neutron scattering experiments (see Sec. III.F for neutron polarization analysis) is related to $S^{zz}(\mathbf{Q},\omega)$ via $S(\mathbf{Q},\omega) = 2S^{zz}(\mathbf{Q},\omega)$. By measuring $S(\mathbf{Q},\omega)$ in absolute units via phonon or vanadium normalization (Xu, Xu, and Tranquada, 2013), one can estimate the energy dependence of the $\mathbf{Q}$-averaged or the local dynamic susceptibility $\chi''(\omega) = \int \chi''(\mathbf{Q},\omega) d\mathbf{Q} / \int d\mathbf{Q}$ within sufficient Brillouin zones (BZ) to sample representative wave vectors of $\chi''(\mathbf{Q},\omega)$ (Lester *et al.*, 2010), where $\chi''(\mathbf{Q},\omega) = (1/3)\mathrm{tr}(\chi''_{\alpha\beta}(\mathbf{Q},\omega))$. The overall strength of the magnetic excitations, corresponding to the local fluctuating moment $\langle \mathbf{m}^2 \rangle$, can then be computed via (Lester *et al.*, 2010)

$$\langle \mathbf{m}^2 \rangle = \frac{3\hbar}{\pi} \int_{-\infty}^{\infty} \frac{\chi''(\omega) d\omega}{1 - \exp(-\hbar\omega/k_B T)}.$$

The total moment sum rule requires $M_0^2 = M^2 + \langle \mathbf{m}^2 \rangle = g^2 S(S+1)$, where M is the static ordered moment of the system. One of the central purposes of inelastic neutron scattering experiments is to determine the energy and wave vector dependence of $\chi''(\mathbf{Q},\omega)$ in absolute units for various iron pnictides and compare the outcome with those in copper oxide and heavy fermion superconductors. These measurements will also allow the determination of an effective spin S for the system.

In this article, we present a comprehensive review of recent neutron scattering results on iron-based superconductors, mainly focusing on the evolution of the static AF order and spin dynamics of iron pnictides and chalcogenides. In Sec. II, we summarize the static AF order for various iron pnictides and chalcogenides and its doping evolution. This includes the effects of electron and hole doping on the static AF order and tetragonal-to-orthorhombic structural transitions (Sec. II.A.); how impurity and isoelectronic substitution affect the magnetic and structural phase transitions (Sec. II.B). Section III summarizes spin excitations and their relationship with superconductivity. They include spin waves in the parent compounds of iron-based superconductors (Sec. III.A), as well as the neutron spin resonance and its relationship with superconductivity (Sec. III.B); the electron- and hole-doping evolution of the spin excitations in the $BaFe_2As_2$ family of iron pnictides (Sec. III.C); evolution of spin excitations in iron chalcogenides and alkali iron selenides (Sec. III.D); impurity effects on spin excitations of iron pnictide and chalcogenide superconductors (Sec. III.E); neutron polarization analysis of spin-excitation anisotropy in iron pnictides (Sec. III.F); the electronic nematic phase and neutron scattering experiments under uniaxial pressure (Sec. III.G); comparison with μSR, NMR, and RIXS measurements (Sec. III.H); and comparison of spin excitations in iron-based superconductors with those in copper oxide and heavy fermion superconductors (Sec. III.I). Section IV provides a brief account of current theoretical understanding of spin excitations in iron-based superconductors. Finally, we summarize the results and discuss possible future directions for the field.

II. STATIC ANTIFERROMAGNETIC ORDER AND ITS DOPING EVOLUTION

A. Lattice and magnetic order in the parent compounds of iron-based superconductors

From a crystal structure point of view, the parent compounds of iron-based superconductors can be classified into five different families: *R*FeAsO (R = La, Ce, Pr, Nd, Sm,…,

the 1111 system), AFe_2As_2 (A = Ba, Sr, Ca, K, the 122 system), $AFeAs$ (A = Li, Na, the 111 system), $Fe_{1+y}Te_{1-x}Se_x$ (the 11 system), and $A_xFe_{2-y}Se_2$ alkali iron selenides (A = K, Rb, Cs, Tl, …, including the insulating 245 phase $A_2Fe_4Se_5$ and the semiconducting 234 phase $A_2Fe_3Se_4$) (Sadovskii, 2008; Aswathy *et al.*, 2010; Johnston, 2010; Paglione and Greene, 2010; Stewart, 2011; Zhao *et al.*, 2012; Dagotto, 2013; Wang *et al.*, 2014), where the 122 and 245 compounds have two FeAs(Se) layers in the unit cell and other systems have single FeAs(Se) layer. A recent development in the field is the synthesis of iron selenide superconductors via intercalation of molecular complexes between layers of FeSe (Krzton-Maziopa *et al.*, 2012; Ying *et al.*, 2012; Burrard-Lucas *et al.*, 2013). The crystal structures at room temperature are all tetragonal except for the insulating 245 phase and some of them will become orthorhombic at low temperatures below T_s. Neutron diffraction measurements have established that the long-range AF order in the parent compounds of iron pnictide superconductors including the 1111, 122, 111 families is collinear with moment aligned along the a_o axis of the orthorhombic structure [Figs. 1(a), 1(d), and 1(e)] (Lynn and Dai, 2009), except for the stoichiometric LiFeAs system which is superconducting without a magnetically ordered parent compound (Pitcher *et al.*, 2008; Tapp *et al.*, 2008; Wang *et al.*, 2008). Although the in-plane collinear AF structures for different classes of iron pnictides are identical [Fig. 1(e)], the ordering along the c axis is material dependent. In the 122 system, which has two magnetic irons per formula unit, the ordering is AF within a unit cell along the c axis [Fig. 1(a)]. For the 111 system with one iron per unit cell, the magnetic structure doubles the chemical unit cell along the c axis [Fig. 1(d)]. While the collinear AF structure in iron pnictides is the so-called C-type antiferromagnet stemming from the original work of Wollan and Koehler on perovskite manganese oxides (Wollan and Koehler, 1955), the related pnictide materials such as $BaMn_2As_2$ (Singh *et al.*, 2009) and $CaCo_2As_2$ (Quirinale *et al.*, 2013) have the G- [Figs. 1(b) and 1(f)] and A-type [Fig. 1(c)] AF structures, respectively. Recently, another AF parent compound was found in the electron-overdoped $LaFeAsO_{1-x}H_x$ ($x \sim 0.5$) system in addition to the usual collinear AF structure at $x = 0$ (Hiraishi *et al.*, 2014).

For the iron chalcogenides (the 11 family) and alkali iron selenides, their crystal structures are shown in Figs. 2(a) and 2(b), respectively. Instead of a collinear AF structure, the parent compound of the 11 family has a bicollinear AF spin structure as shown in Fig. 2(c) (Fruchart *et al.*, 1975; Bao *et al.*, 2009; S. L. Li *et al.*, 2009). Compared to the collinear spin structure of the 122 family in Fig. 1(e), the iron spins are rotated 45° within the a_ob_o plane in the 11 system. The magnetic structure of the 11 family is sensitive to the excess iron population at the interstitial iron site (Rodriguez *et al.*, 2010, 2011). While the bicollinear magnetic order is commensurate for $Fe_{1+x}Te$ with $x \lesssim 9\%$, it exhibits incommensurate helical magnetic order that competes with the bicollinear commensurate ordering close to T_N for $x \gtrsim 12\%$ (Rodriguez *et al.*, 2010, 2011, 2013). The alkali iron selenides (the 245 family) (Guo *et al.*, 2010; Fang *et al.*, 2011) have two different iron vacancy structures including the insulating $\sqrt{5} \times \sqrt{5}$ iron vacancy ordered phase [Figs. 2(d), 2(f), and 2(g)] (Bao *et al.*, 2011; M. Wang *et al.*, 2011; Ye *et al.*, 2011) and the

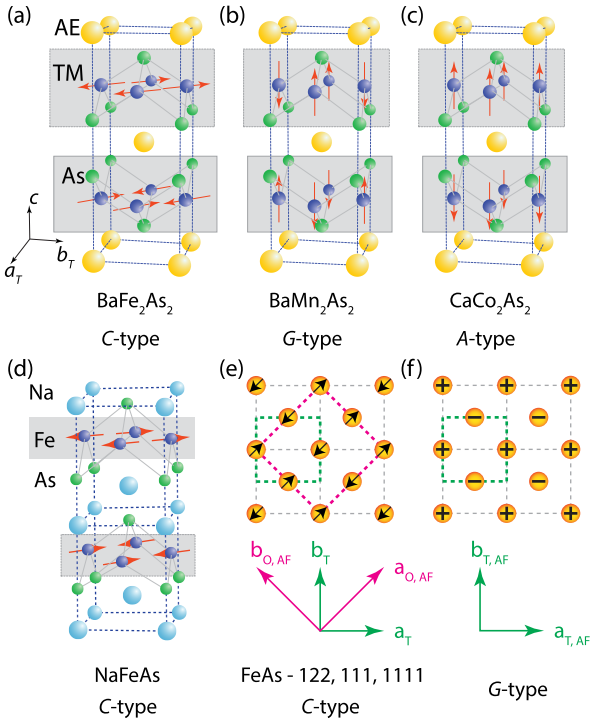

FIG. 1 (color online). Crystal structure and magnetic order in different families of pnictides. (a) The crystal and magnetic structures of the $BaFe_2As_2$ in the AF ordered phase. The colored balls indicate Ba, As, and Fe positions. The arrows mark the ordered moment directions of Fe in the AF ordered state (the C type). The a_T, b_T, and c show the Cartesian coordinate system suitable for the paramagnetic tetragonal phase of $BaFe_2As_2$. From Huang, Qiu *et al.*, 2008. (b) The AF structure of $BaMn_2As_2$, where the ordered moments on Mn are along the c-axis direction (the G type). From Singh *et al.*, 2009. (c) The crystal structure of $CaCo_2As_2$, where the ordered moments on Co form the A-type AF structure. From Quirinale *et al.*, 2013. (d) The collinear AF order in NaFeAs doubles the crystalline unit cell along the c axis. From Li, de la Cruz *et al.*, 2009. (e) The collinear C-type AF structure in the Fe plane, where the one dashed box marks the tetragonal crystalline unit cell in the paramagnetic state and the other dashed box indicates the orthorhombic magnetic unit cell. The $a_{o,AF}$ and $b_{o,AF}$ mark directions of the orthorhombic lattice. (f) The in-plane moment projections for the G-type antiferromagnets.

semiconducting rhombus iron vacancy ordered 234 phase [Fig. 2(e)] (Zhao *et al.*, 2012; Wang *et al.*, 2014). While the 234 phase has a AF structure similar to the parent compounds of the 122 family [Fig. 2(e)] (Zhao *et al.*, 2012), the insulating 245 phase has the block AF structure with moments along the c axis [Fig. 2(d)] (Bao *et al.*, 2011; M. Wang *et al.*, 2011; Ye *et al.*, 2011) and in the plane [Figs. 2(f) and 2(g)] (May *et al.*, 2012), respectively. Compared with the parent compounds of the 122 system, the ordered moments of the 11 and 245 systems are much larger. In Table I, we summarize the lattice parameters, structure transition temperature T_s, the AF phase transition temperature T_N, and the static ordered moments for the parent compounds of different iron-based superconductors. In the 1111, 111, and 245 systems, the structural transition occurs at a temperature higher than that of the

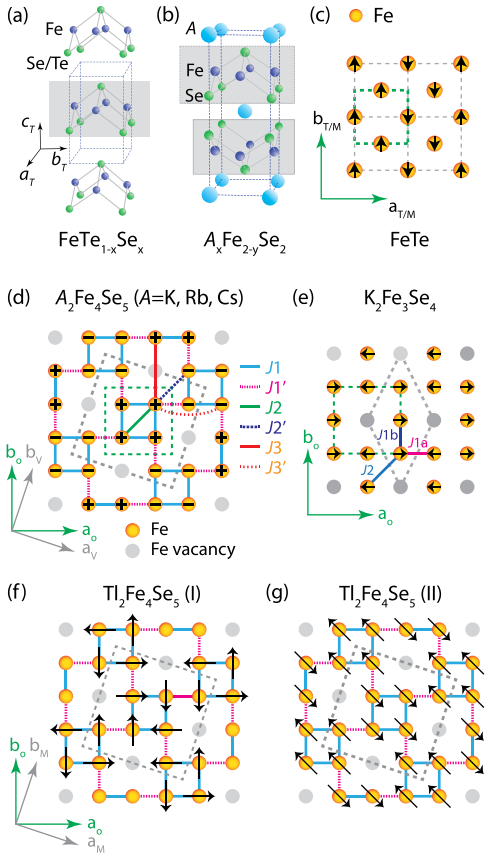

FIG. 2 (color online). Crystal and magnetic structures of iron chalcogenides and alkali iron selenides. (a) The crystal structure of the $FeTe_{1-x}Se_x$ iron chalcogenide, where Fe and Se/Te positions are marked. (b) The tetragonal phase crystal structure of $A_xFe_{2-y}Se_2$. The positions of A, Fe, and Se are marked. (c) The in-plane bicollinear magnetic structure of FeTe, where the arrows indicate the moment directions (Fruchart *et al.*, 1975; Bao *et al.*, 2009; S. L. Li *et al.*, 2009). (d) The in-plane crystal and magnetic structures of $A_2Fe_4Se_5$ in the vacancy ordered insulating phase. Only iron positions are plotted and the dashed lines mark the structural and magnetic unit cells. The colored (dashed) lines represent the nearest (J_1, J_1'), next nearest (J_2, J_2'), and next next nearest (J_3, J_3') neighbor exchange interactions, respectively (Bao *et al.*, 2011; M. Wang *et al.*, 2011; M. Y. Wang *et al.*, 2011; Ye *et al.*, 2011). (e) The crystal and magnetic structures of $A_2Fe_3Se_4$ in the vacancy ordered semiconducting phase (Zhao *et al.*, 2012). The nearest and next nearest neighbor exchange couplings are clearly marked. (f), (g) Other possible magnetic structures of $Tl_2Fe_4Se_5$ in the vacancy ordered phase (May *et al.*, 2012).

AF phase transition (Johnston, 2010; Stewart, 2011). In the 122 system, the structural and magnetic transitions occur almost simultaneously in the undoped parent compounds (Kim *et al.*, 2011), but are well separated upon electron doping (Canfield and Bud'ko, 2010).

B. The effect of electron, hole doping, impurity, and isoelectronic substitution on the AF and structural transitions

Before discussing the impact of electron and hole doping on the long-range AF order, we define momentum transfer in reciprocal space and compare the sizes of the Brillouin zones for the parent compounds of different families of high-T_c superconductors. Figures 3(a)–3(c) show spin arrangements within one layer of La_2CuO_4 (Vaknin *et al.*, 1987), $BaFe_2As_2$ (Huang, Qiu *et al.*, 2008), and FeTe (Fruchart *et al.*, 1975; Bao *et al.*, 2009; S. L. Li *et al.*, 2009), respectively. The chemical unit cells are marked as dashed lines and the magnetic unit cells are shaded. The positions of Cu^{2+}/Fe^{2+} and $O^{2-}/As^{3-}/Te^{2-}$ are also marked. The momentum transfer $\mathbf{Q}$ at (q_x, q_y, q_z) in $Å^{-1}$ can be defined as $(H, K, L) = (q_x a/2\pi, q_y b/2\pi, q_z c/2\pi)$ in reciprocal lattice units (rlu), where a (or a_o), b (or b_o), and c are lattice parameters of the orthorhombic unit cell. In this notation, the AF order in the parent compound of copper oxide superconductors occurs at $\mathbf{Q}_{AF} = (H, K) = (0.5 \pm m, 0.5 \pm n)$, where $m, n = 0, 1, 2, \ldots$ and a magnetic Brillouin zone is shown as a shaded box in Fig. 3(d). Another equivalent Brillouin zone near Γ is marked by the dashed lines, while the Brillouin zone of the chemical unit cell is the green dashed box. If the ordered moment is entirely on the iron site in $BaFe_2As_2$, the chemical unit cell is twice the size of the magnetic unit cell along the b_o axis direction due to out-of-plane positions of the As atoms [Fig. 3(b)]. In a completely detwinned sample, the magnetic Brillouin zone is the shaded area around $\mathbf{Q}_{AF} = (H, K, L) = (1 \pm 2m, 0 \pm 2n, L)$, where $L = \pm 1, 3, 5, \ldots$ rlu, larger in size than the chemical Brillouin zone in the dashed area. Because the AF order in iron pnictides is always preceded by a tetragonal-to-orthorhombic lattice distortion, the twinning effect in the orthorhombic state means that AF Bragg peaks from the twinned domains appear at positions rotated by 90° [dots in Fig. 3(g)]. Therefore, to properly account for the twin domain effect, one needs to carry out wave vector integration within the region marked by solid lines in Fig. 3(g). The local dynamic susceptibility $\chi''(\omega)$ is computed via dividing the integration outcome by the size of one Brillouin zone [the shaded area in Fig. 3(g)], and then average the results over several Brillouin zones. Alternatively, $\chi''(\omega)$ can simply be calculated through dividing the integration signal in the (0,0), (1,1), (2,0), (1, −1) box in Fig. 3(g) by the size of the box. Figures 3(c), 3(f), and 3(h) summarize the bicollinear spin structure of FeTe, its associated magnetic Bragg peaks in reciprocal space for detwinned, and twinned samples, respectively. Depending on the size of the unit cell, the same AF Bragg peak for collinear AF order in $BaFe_2As_2$ and bicollinear AF order in FeTe can appear with different Miller indices. For example, if we choose unit cells of $BaFe_2As_2$ with one [half the shaded area in Fig. 3(b) and ignoring As], two [similar to shaded area in Fig. 3(a)], and four irons [doubling the shaded area in Fig. 3(b) along the c axis], the same AF Bragg peak would occur at in-plane wave vectors (0.5,0), (0.5,0.5), and (1,0), respectively. For the bicollinear AF order FeTe, one iron and two irons per unit cell would have the same AF Bragg peak at the in-plane wave vectors (0.25,0.25) and (0.5,0), respectively.

Figures 4(a)–4(c) summarize the effective nearest neighbor and next nearest neighbor magnetic exchange couplings for La_2CuO_4, $BaFe_2As_2$, and FeTe, respectively. Figures 4(d)–4(f) show the corresponding reciprocal space with $\mathbf{Q}_{AF}$ positions marked as dots for the two different twin domains. While neutron scattering typically studies the shaded region of

TABLE I. Summary of the structure transition temperatures T_s, the magnetic transition temperatures T_N, and the ordered magnetic moment per iron for the AF ordered parent compounds of the iron-based superconductors. The lattice parameters in the paramagnetic tetragonal state are also listed.

Materials	$a_T \equiv b_T$ (Å)	c (Å)	T_s (K)	T_N (K)	Moment/Fe (μ_B)
LaFeAsO[a]	4.0301	8.7368	155	137	0.36–0.6
CeFeAsO[b]	3.9959	8.6522	158	140	0.8
PrFeAsO[c]	3.997	8.6057	153	127	0.48
NdFeAsO[d]	3.9611	8.5724	150	141	0.25
$LaFeAsO_{0.5}H_{0.5}$[e]	3.975	8.67	95	92	1.21
$CaFe_2As_2$[f]	3.912	11.667	173	173	0.80
$SrFe_2As_2$[g]	3.920	12.40	220	220	0.94
$BaFe_2As_2$[h]	3.957	12.968	~140	~140	0.87
$Na_{0.985}FeAs$[i]	3.9448	6.9968	49	39	0.09
$Fe_{1.068}Te$[j]	3.8123	6.2517	67	67	2.25
$K_2Fe_4Se_5$[k]	8.7306	14.113	578	559	3.31
$Rb_2Fe_4Se_5$[l]	8.788	14.597	515	502	3.3
$Cs_2Fe_4Se_5$[m]	8.865	15.289	500	471	3.4
$TlFe_{1.6}Se_2$[n]	~8.71	14.02	463	100	~3

[a]Huang, Zhao *et al.* (2008), McGuire *et al.* (2008), de la Cruz *et al.* (2008), and Qureshi *et al.* (2010).
[b]Zhao *et al.* (2008b) and Q. Zhang *et al.* (2013).
[c]Kimber *et al.* (2008) and Zhao *et al.* (2008c).
[d]Chen *et al.* (2008) and Qiu *et al.* (2008).
[e]Hiraishi *et al.* (2014).
[f]Goldman *et al.* (2008), Kreyssig *et al.* (2008), and Goldman *et al.* (2009).
[g]Jesche *et al.* (2008), Kaneko *et al.* (2008), and Zhao, Ratcliff-II *et al.* (2008).
[h]Huang, Qiu *et al.* (2008) and Kim *et al.* (2011).
[i]Li, de la Cruz *et al.* (2009).
[j]Bao *et al.* (2009) and S. L. Li *et al.* (2009).
[k]Bao *et al.* (2011).
[l]M. Wang *et al.* (2011) and Ye *et al.* (2011).
[m]Ye *et al.* (2011).
[n]May *et al.* (2012).

the reciprocal space within the Brillouin zone near $\mathbf{Q}_{\mathrm{AF}}$, RIXS can only probe spin excitations within the circles near the origin Γ due to kinematic constraints from energies of the incident and outgoing photons used to enhance the magnetic scattering at the Cu L_3 edge and the Fe L_3 edge (Tacon *et al.*, 2011; K.-J. Zhou *et al.*, 2013).

Although the field of iron-based superconductors started with the discovery of the 1111 family of materials (Kamihara *et al.*, 2008), a majority of recent neutron scattering work has focused on the 122 family due to the availability of high-quality single crystals (Canfield and Bud'ko, 2010). In the undoped state, a prototypical 122 compound such as $BaFe_2As_2$ exhibits tetragonal-to-orthorhombic lattice distortion and the AF order below $T_s \approx T_N \approx 138$ K (Huang, Qiu *et al.*, 2008). Figure 5 summarizes the evolution of the structural and magnetic phase transitions for the electron- and hole-doped $BaFe_2As_2$. From transport, neutron diffraction, and x-ray diffraction measurements (Christianson *et al.*, 2009; Chu *et al.*, 2009; Lester *et al.*, 2009; Pratt *et al.*, 2009; Canfield and Bud'ko, 2010; Nandi *et al.*, 2010), the phase diagram of electron-doped $Ba(Fe_{1-x}Co_x)_2As_2$ as shown in Fig. 5(b) has been established. Upon electron doping via Co substitution for Fe to suppress the static AF order and induce superconductivity, the structural and AF phase transitions are gradually separated with the structural transition occurring at higher temperatures than the magnetic one. The collinear static AF order coexists and competes with superconductivity in the underdoped regime marked as a shaded area in Fig. 5(b) (Christianson *et al.*, 2009; Pratt *et al.*, 2009). For electron-doping levels near optimal superconductivity, the orthorhombic lattice distortion $\delta = (a-b)/(a+b)$ initially increases with decreasing temperature below T_N, but then decreases dramatically below T_c. For $BaFe_{1.874}Co_{0.126}As_2$, the orthorhombic structure evolves smoothly back to a tetragonal structure below T_c and the system is believed to enter into a "reentrant" tetragonal phase as shown in Fig. 5(b) (Nandi *et al.*, 2010). Subsequent neutron diffraction experiments revealed that the static AF order in the underdoped regime changes from commensurate to transversely incommensurate for $Ba(Fe_{1-x}Co_x)_2As_2$ with $0.056 \leq x \leq 0.062$ (Pratt *et al.*, 2011). These results have been hailed as direct evidence for spin-density-wave order in iron pnictides (Pratt *et al.*, 2011), where the static AF order arises from the Fermi surface nesting between the hole and electron pockets at the Γ and M points of the reciprocal space, respectively (Dong *et al.*, 2008; Fink *et al.*, 2009; Vorontsov, Vavilov, and Chubukov, 2009).

Figure 5(d) shows the phase diagram of electron-doped $BaFe_{2-x}Ni_xAs_2$ obtained from x-ray and neutron scattering experiments (Luo *et al.*, 2012; Lu *et al.*, 2013). Here the AF order decreases with increasing Ni doping and disappears near optimal superconductivity in a first-order-like fashion with an avoided quantum critical point (Lu *et al.*, 2013). Similar to $Ba(Fe_{1-x}Co_x)_2As_2$ with $0.056 \leq x \leq 0.062$ (Pratt *et al.*, 2011), there is short-range (60 Å) incommensurate AF order

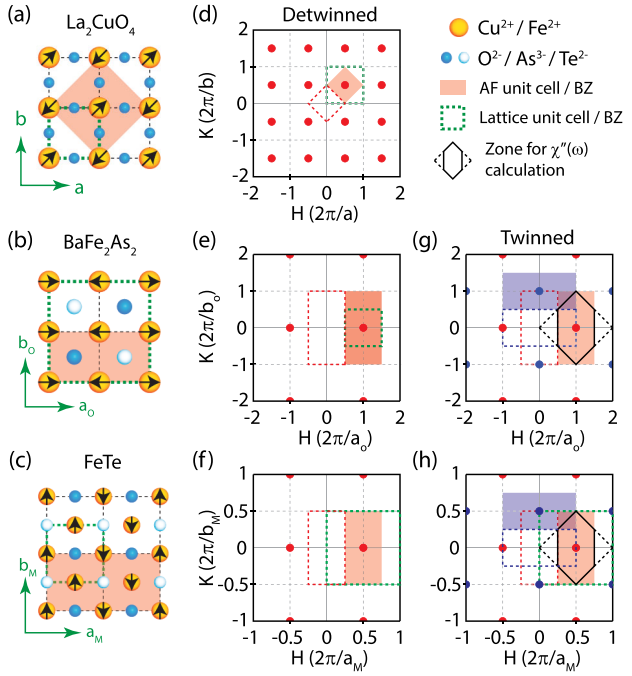

FIG. 3 (color online). Comparison of the AF structures of copper oxides and iron pnictides and chalcogenides, and the corresponding reciprocal lattice and the twinning effect. (a) The in-plane AF structure of the parent compound of copper oxide superconductors with chemical and magnetic unit cells marked as shaded area and dashed line. From Fujita *et al.*, 2012. (d) The reciprocal space where the solid dots represent the AF ordering wave vectors. The shaded area and the dashed lines indicate the size of the in-plane magnetic and chemical Brillouin zone, respectively. (b) The in-plane AF structure of $BaFe_2As_2$, where the open and filled circles indicate As positions below and above the iron plane, respectively. From Johnston, 2010. The magnetic and chemical unit cells are marked as a shaded area and dashed lines, respectively, and (e) the corresponding reciprocal space, where dots indicate $\mathbf{Q}_{AF}$. (g) The effect of twin domains for AF order and Brillouin zones. The solid lines mark the integration area in reciprocal space to obtain the total magnetic scattering within one Brillouin zone. (c) The in-plane AF structure of FeTe, and (f) the corresponding reciprocal space in a detwinned sample. (h) The effect of twin domain in reciprocal space. The shaded dashed boxes in (d), (e), and (f) indicate the AF Brillouin zones near the Γ point probed by RIXS.

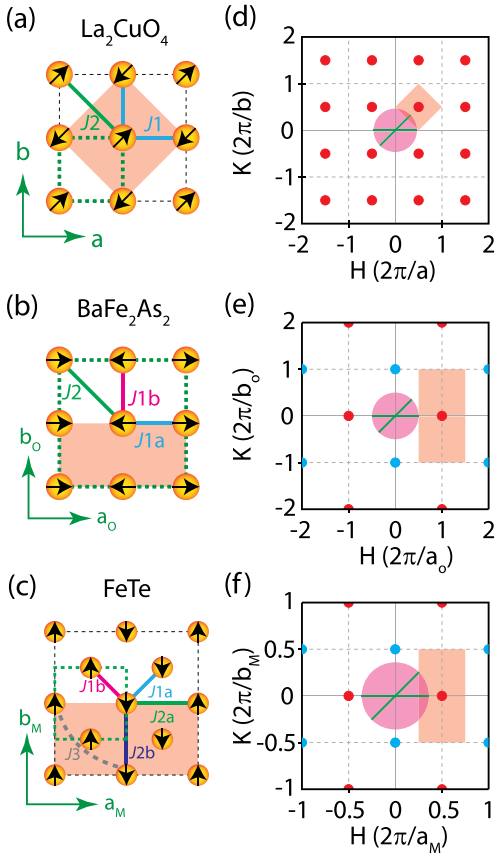

FIG. 4 (color online). Real and reciprocal space of La_2CuO_4, $BaFe_2As_2$, and FeTe with magnetic exchange couplings and regions of reciprocal space probed by neutron scattering and RIXS. (a) The in-plane AF structure of La_2CuO_4, where nearest and next nearest neighbor magnetic exchange couplings are marked as J_1 (solid line) and J_2 (solid line), respectively. (d) The reciprocal space where the solid dots represent the AF ordering wave vectors. The circular area at Γ indicates the region of reciprocal space that can be probed by RIXS using the Cu L_3 edge, while the AF Brillouin zone probed by neutron scattering is marked by the square. From Tacon *et al.*, 2011. (b) The in-plane AF structure of $BaFe_2As_2$ with the nearest neighbors (J_{1a}, J_{1b}) and second nearest neighbor J_2 magnetic exchange couplings. (e) The corresponding reciprocal space, where the circle indicates the reciprocal space area covered by RIXS using the Fe L_3 edge. From K.-J. Zhou *et al.*, 2013. (c) The in-plane AF structure of FeTe with the nearest neighbors (J_{1a}, J_{1b}) and second nearest neighbors (J_{2a}, J_{2b}) magnetic exchange couplings. (f) The corresponding reciprocal space with the circle showing the reciprocal space covered by RIXS.

for samples near optimal superconductivity (Luo *et al.*, 2012). Although these results indicate an avoided quantum critical point in $BaFe_{2-x}Ni_xAs_2$, they are in direct conflict with a recent NMR work suggesting the presence of two quantum critical points (R. Zhou *et al.*, 2013). However, these NMR results are inconsistent with systematic NMR and neutron scattering results on nearly optimally Co- and Ni-doped $BaFe_2As_2$ samples revealing a cluster spin-glass state for the magnetic order (Dioguardi *et al.*, 2013; Lu *et al.*, 2014). The spin-glass picture of the magnetic order near optimal superconductivity in electron-doped iron pnictides is clearly inconsistent with the spin-density-wave explanation of the transverse incommensurate magnetic order (Pratt *et al.*, 2011). These results suggest that the incommensurate AF order in electron-doped iron pnictides arises from localized moments (Fang *et al.*, 2008; Si and Abrahams, 2008; Xu, Müller, and Sachdev, 2008), instead of being a spin-density-wave order induced by nested Fermi surfaces like incommensurate AF order in pure chromium metal (Fawcett *et al.*, 1994).

The electronic phase diagrams of hole-doped $Ba_{1-x}K_xFe_2As_2$ and $Ba_{1-x}Na_xFe_2As_2$ determined from neutron scattering experiments on powder samples are summarized in Figs. 5(a) and 5(c), respectively (Avci *et al.*, 2012, 2013, 2014). Compared with electron-doped $BaFe_2As_2$, hole doping does not separate the structural and magnetic phase transitions and the AF and superconducting coexistence

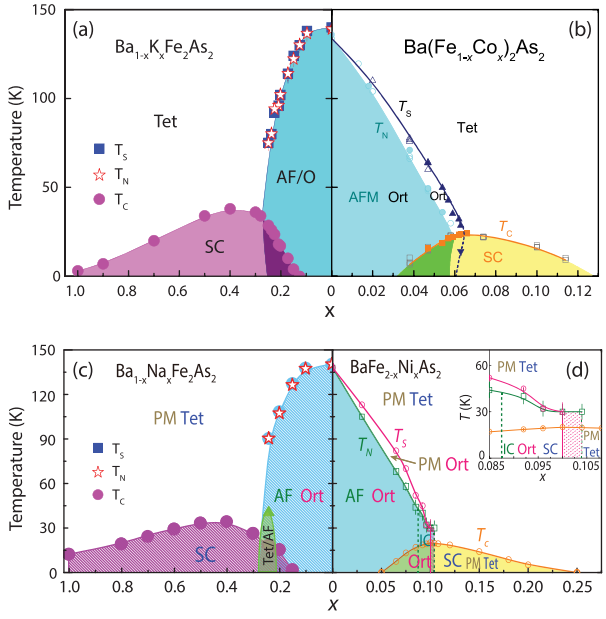

FIG. 5 (color online). The structural and magnetic phase diagrams of electron- and hole-doped $BaFe_2As_2$. (a) The coupled structural and AF phase transitions in hole-doped $Ba_{1-x}K_xFe_2As_2$ as determined from neutron powder diffraction experiments (Avci *et al.*, 2012). The structural and AF phase transitions are denoted as T_s and T_N, respectively. (b) The phase diagram of $Ba(Fe_{1-x}Co_x)_2As_2$ determined from x-ray and neutron diffraction experiments (Nandi *et al.*, 2010). (c) The structural and magnetic phase diagram of hole-doped $Ba_{1-x}Na_xFe_2As_2$ from neutron diffraction experiments (Avci *et al.*, 2013, 2014). The shaded region denotes the presence of a tetragonal AF phase. (d) Similar phase diagram for electron-doped $BaFe_{2-x}Ni_xAs_2$ (Luo *et al.*, 2012; Lu *et al.*, 2013). Here the incommensurate (IC) AF order is a spin-glass phase coexisting and competing with the superconducting phase (Lu *et al.*, 2014).

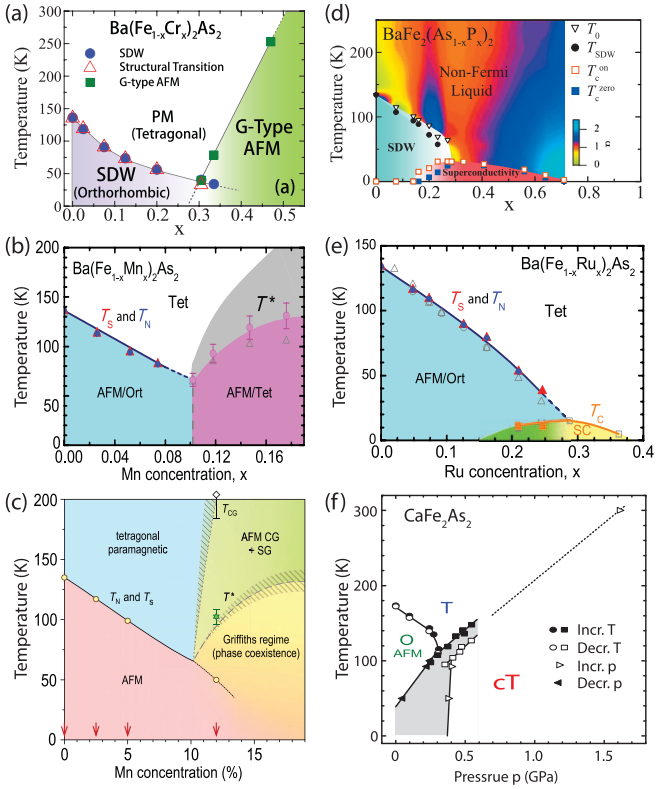

FIG. 6 (color online). The electronic phase diagrams of various other doped 122 family of iron pnictides. (a) The structural and magnetic phase diagram of Cr-doped $Ba(Fe_{1-x}Cr_x)_2As_2$ (Marty *et al.*, 2011). For $x \leq 0.2$, Cr doping suppresses the coupled structural and magnetic phase transition without inducing superconductivity. For $x > 0.3$, the system becomes a G-type antiferromagnet (see Fig. 1). (b) The structural and magnetic phase diagram for Mn-doped $Ba(Fe_{1-x}Mn_x)_2As_2$ (Kim *et al.*, 2010). (c) Similar phase diagram for $Ba(Fe_{1-x}Mn_x)_2As_2$ obtained by another group (Inosov *et al.*, 2013). Here the system is believed to form a disordered spin-glass (Griffiths) phase for $x > 0.1$. (d) The structural and magnetic phase diagram of isoelectronic doped $BaFe_2(As_{1-x}P_x)_2$ determined from transport and NMR measurement (Shibauchi, Carrington, and Matsuda, 2014). Recent neutron powder diffraction experiments indicate a coupled structural and magnetic phase transition (Allred *et al.*, 2014). (e) The structural and magnetic phase diagram of the isoelectronically doped $Ba(Fe_{1-x}Ru_x)_2As_2$ (Kim *et al.*, 2011). There is no evidence of a quantum critical point near optimal superconductivity. (f) The pressure dependence of the structural and magnetic phase transitions in $CaFe_2As_2$. The system enters into a collapsed tetragonal (cT) phase above ~0.4 GPa where magnetism disappears (Goldman *et al.*, 2009).

region is also present. In particular, for $Ba_{1-x}Na_xFe_2As_2$ near $x = 0.28$, a new magnetic ordered phase with C_4 tetragonal symmetry of the underlying lattice has been found (Avci *et al.*, 2014). In addition, superconductivity appears in heavily hole-doped regimes, much different from the electron-doped case.

In copper oxide superconductors, superconductivity can be induced only by electron and hole doping into the nearly perfect CuO_2 plane, and impurity substitution at the Cu sites by other elements dramatically suppresses superconductivity (Kastner *et al.*, 1998; Kivelson *et al.*, 2003; Armitage, Fournier, and Greene, 2010; Fujita *et al.*, 2012; Tranquada, Xu, and Zaliznyak, 2014). The situation is much different for iron pnictides. While impurities such as Cr and Mn substituted for Fe in $BaFe_2As_2$ suppress the static AF order in the parent compound without inducing superconductivity [Figs. 6(a)–6(c)] (Kim *et al.*, 2010; Marty *et al.*, 2011; Inosov *et al.*, 2013), isoelectronic substitution by replacing As with P [Fig. 6(d)] (Jiang *et al.*, 2009; Shibauchi, Carrington, and Matsuda, 2014) or Fe with Ru [Fig. 6(e)] in $BaFe_2As_2$ (Kim *et al.*, 2011) can induce superconductivity. For Cr-doped $Ba(Fe_{1-x}Cr_x)_2As_2$, neutron diffraction experiments on single crystals have established the structural and magnetic phase diagrams, showing a suppression of the collinear AF order for samples with $x < 0.3$. For $x > 0.3$, the system becomes a G-type antiferromagnet with a tetragonal structure as shown in Fig. 6(a) (Marty *et al.*, 2011). The situation in Mn-doped $Ba(Fe_{1-x}Mn_x)_2As_2$ is somewhat similar. With increasing Mn doping in $BaFe_2As_2$, the structural and AF phase transitions are gradually suppressed as shown in Figs. 6(b) and 6(c) (Kim *et al.*, 2010; Inosov *et al.*, 2013). For Mn concentration $x \geq 0.1$, the system goes into a mixed phase, possibly in

the Griffiths regime, with coexisting short-range spin correlations at AF wave vectors similar to those in $BaFe_2As_2$ [$\mathbf{Q}_{AF} = \mathbf{Q}_{stripe}$] and $BaMn_2As_2$ [$\mathbf{Q} = \mathbf{Q}_{Néel}$ rotated 45° from $\mathbf{Q}_{AF}$] (Inosov *et al.*, 2013).

In contrast to Cr and Mn doping, isoelectronic doping by replacing As with P in $BaFe_2(As_{1-x}P_x)_2$ induces optimal superconductivity near $x = 0.3$ (Jiang *et al.*, 2009). From the systematic transport and London penetration depth measurements on $BaFe_2(As_{1-x}P_x)_2$, a magnetic quantum critical point has been identified near optimal superconductivity at $x = 0.3$ [Fig. 6(d)] (Shibauchi, Carrington, and Matsuda, 2014). However, recent systematic NMR, x-ray, and neutron diffraction measurements on $BaFe_2(As_{1-x}P_x)_2$ indicate that the coupled T_s and T_N transitions vanish near $x = 0.3$ in a weakly

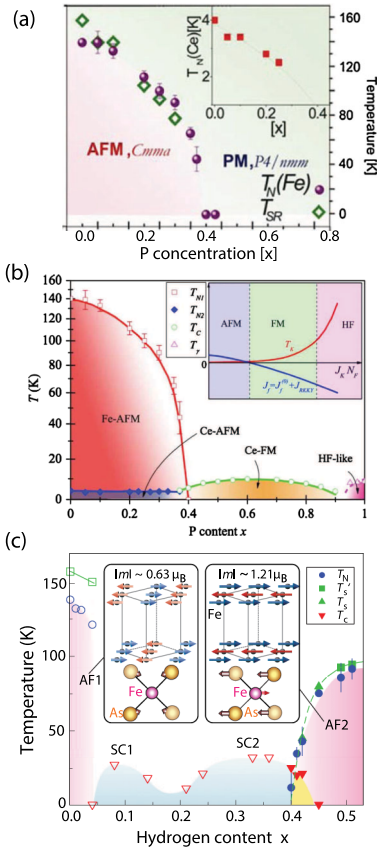

FIG. 7 (color online). The doping evolution of the electronic phase diagrams for P-doped $CeFeAs_{1-x}P_xO$ and H-doped $LaFeAsO_{1-x}H_x$. (a) The structural and magnetic phase diagram of $CeFeAs_{1-x}P_xO$ determined from neutron powder diffraction experiments (de la Cruz *et al.*, 2010). A quantum critical point is found near $x = 0.4$ without the presence of superconductivity. The inset shows the T_N from Ce magnetic ordering. (b) Phase diagram of $CeFeAs_{1-x}P_xO$ determined by transport measurements. In the underdoped regime, the data are consistent with the results of neutron powder diffraction (de la Cruz *et al.*, 2010). The system becomes a Ce-ordered ferromagnetic metal for $0.4 < x < 0.9$. For samples with $x > 0.9$, it becomes a heavy fermion-like metal (Luo *et al.*, 2010). (c) The structural, magnetic, and superconducting phase transitions in H-doped $LaFeAsO_{1-x}H_x$ (Hiraishi *et al.*, 2014). There are two AF phases with different magnetic structures near two superconducting domes.

first order fashion, much like the electron-doped iron pnictides with an avoided quantum critical point (Hu *et al.*, 2015). For isoelectronic $Ba(Fe_{1-x}Ru_x)_2As_2$, optimal superconductivity again appears near the Ru-doping level of $x = 0.3$ [Fig. 6(e)] (Kim *et al.*, 2011). However, there are no reports for the presence of a quantum critical point in this system. Figure 6(f) shows the pressure-temperature phase diagram of the $CaFe_2As_2$ (Goldman *et al.*, 2009). While superconductivity can be induced directly via applying hydrostatic pressure in $BaFe_2As_2$ and $SrFe_2As_2$ (Johnston, 2010; Stewart, 2011), external pressure exerted on $CaFe_2As_2$ results in a nonmagnetic collapsed tetragonal (cT) phase, eliminating the static AF ordered moment and spin excitations without inducing superconductivity (Goldman *et al.*, 2009).

Although a majority of neutron scattering work has focused on the 122 family of materials because of the availability of high-quality single crystals, there are also important phase diagram results in the 1111 family. For example, P doping in the CeFeAsO family of materials suppresses static AF order, but does not induce superconductivity (de la Cruz *et al.*, 2010). Systematic neutron scattering studies of the structural and magnetic phase transitions in powder samples of $CeFeAs_{1-x}P_xO$ suggest that the pnictogen height [the average Fe-As(P) distance] and orthorhombicity of the $CeFeAs_{1-x}P_xO$ unit cell critically control the iron AF ordered moment and Néel temperature of the system. Figure 7(a) shows the P-doping dependence of the structural and AF phase transition temperatures in $CeFeAs_{1-x}P_xO$, suggesting the presence of a magnetic quantum critical point near $x = 0.4$ (de la Cruz *et al.*, 2010). A complete mapping of the $CeFeAs_{1-x}P_xO$ phase diagram shown in Fig. 7(b) was obtained via transport and susceptibility measurements, which reveal that superconductivity does not appear in the entire phase diagram, possibly due to heavy fermion properties of the rare earth element Ce (Luo *et al.*, 2010). Another recent advance is the discovery of bipartite magnetic parent phases in the H-doped $LaFeAsO_{1-x}H_x$ family of materials (Hiraishi *et al.*, 2014). In contrast to the general phase diagram of iron pnictides, superconductivity in $LaFeAsO_{1-x}H_x$ appears in two domes adjacent to two different AF phases with different magnetic structures and Néel temperatures [Fig. 7(c)] (Hiraishi *et al.*, 2014). These results again confirm the notion that superconductivity in iron-based superconductors is intimately connected with the magnetic interactions.

III. SPIN EXCITATIONS AND THEIR RELATIONSHIP WITH SUPERCONDUCTIVITY

The rapid development of neutron time-of-flight chopper spectrometers in recent years has allowed measurements of spin excitations in high-T_c superconductors throughout the Brillouin zone for energy transfers up to 1 eV. In the case of copper oxides, spin waves in La_2CuO_4 have been mapped out throughout the Brillouin zone (Coldea *et al.*, 2001; Headings *et al.*, 2010). While the low-energy spin excitations are well described by theories based on the Heisenberg Hamiltonian, high-energy spin waves are damped near the $\mathbf{Q} = (1/2, 0)$ position in reciprocal space and merge into a momentum dependent continuum suggesting the decay of spin waves into other excitations (Coldea *et al.*, 2001; Headings *et al.*, 2010).

TABLE II. Comparison of the effective magnetic exchange couplings for parent compounds of copper-based and iron-based superconductors. Here the nearest, next nearest, next next nearest neighbor, and c axis exchange couplings are SJ_{1a} (SJ_{1b}), SJ_{2a}(SJ_{2b}), SJ_3, and SJ_c, respectively, where S is the spin of the system.

Materials	SJ_{1a} (meV)	SJ_{1b} (meV)	SJ_{2a} (meV)	SJ_{2b} (meV)	SJ_3 (meV)	SJ_c (meV)
La_2CuO_4[a]	55.9 ± 2	55.9 ± 2	-5.7 ± 1.5	-5.7 ± 1.5	0	0
NaFeAs[b]	40 ± 0.8	16 ± 0.6	19 ± 0.4	19 ± 0.4	0	1.8 ± 0.1
$CaFe_2As_2$[c]	49.9 ± 9.9	-5.7 ± 4.5	18.9 ± 3.4	18.9 ± 3.4	0	5.3 ± 1.3
$BaFe_2As_2$[d]	59.2 ± 2.0	-9.2 ± 1.2	13.6 ± 1	13.6 ± 1	0	1.8 ± 0.3
$SrFe_2As_2$ (L)[e]	30.8 ± 1	-5 ± 4.5	21.7 ± 0.4	21.7 ± 0.4	0	2.3 ± 0.1
$SrFe_2As_2$ (H)[f]	38.7 ± 2	-5 ± 5	27.3 ± 0.3	27.3 ± 0.3	0	2.3 ± 0.1
$Fe_{1.05}Te$[g]	-17.5 ± 5.7	-51.0 ± 3.4	21.7 ± 3.5	21.7 ± 3.5	6.8 ± 2.8	~ 1
$Rb_{0.89}Fe_{1.58}Se_2$[h]	-36 ± 2	15 ± 8	12 ± 2	16 ± 5	9 ± 5	1.4 ± 0.2
$(Tl, Rb)_2Fe_4Se_5$[i]	-30 ± 1	31 ± 13	10 ± 2	29 ± 6	0	0.8 ± 1
$K_{0.85}Fe_{1.54}Se_2$[j]	-37.9 ± 7.3	-11.2 ± 4.8	19.0 ± 2.4	19.0 ± 2.4	0	0.29 ± 0.06

[a]Coldea *et al.* (2001).
[b]Zhang *et al.* (2014a).
[c]Zhao *et al.* (2009).
[d]Harriger *et al.* (2011).
[e]Ewings *et al.* (2011).
[f]The L and H are fits using low- and high-energy spin waves, respectively.
[g]Lipscombe *et al.* (2011).
[h]M. Y. Wang *et al.* (2011).
[i]Chi *et al.* (2013).
[j]Zhao *et al.* (2014).

The effective magnetic exchange couplings of La_2CuO_4 determined from the Heisenberg model are summarized in Table II. The doping evolution of spin excitations as a function of electron and hole doping and their coupling to superconductivity have been reviewed recently (Armitage, Fournier, and Greene, 2010; Fujita *et al.*, 2012; Tranquada, Xu, and Zaliznyak, 2014). In the case of iron-based superconductors, the situation is more complicated. Of the 11, 111, 122, 1111, and 245 families of materials, spin waves in the AF parent compounds throughout the Brillouin zone were mapped out for the 11 (Lipscombe *et al.*, 2011; Zaliznyak *et al.*, 2011), 111 (Zhang *et al.*, 2014a), 122 (Diallo *et al.*, 2009; Zhao *et al.*, 2009; Ewings *et al.*, 2011; Harriger *et al.*, 2011), and 245 (M. Y. Wang *et al.*, 2011; Chi *et al.*, 2013; Xiao *et al.*, 2013) families of materials due to the availability of large single crystals needed for inelastic neutron scattering experiments. Although single crystals of the 1111 family of materials are still not large enough to allow a determination of the entire spin-wave spectra, measurements of low-energy spin waves reveal that the system is highly two dimensional with a weak magnetic exchange coupling along the c axis (Ramazanoglu *et al.*, 2013). In Secs. III.A and III.B, we describe spin-wave measurements in the parent compounds of different families of iron-based superconductors and discuss their relationship with superconductivity.

A. Spin waves in the parent compounds of iron-based superconductors

Inelastic neutron scattering studies of spin waves in the parent compounds of iron-based superconductors began soon after the availability of single crystals of the 122 family (Canfield and Bud'ko, 2010). For a magnetically ordered system, spin waves occur when the magnetic moments precess around their ordered configuration. Regardless of the microscopic origin of the magnetic order, spin waves of an ordered system should exhibit sharp excitations in the long wavelength limit (small $\mathbf{q}$ away from the AF ordering wave vector) and can be described by a suitable Hamiltonian using perturbation theory. For a spin Hamiltonian, one can start with a Heisenberg model where the energy of spin waves depends only on the relative orientation of neighboring spins. In the initial neutron scattering experiments on low-energy spin waves in $SrFe_2As_2$ (Zhao *et al.*, 2008a), $CaFe_2As_2$ (McQueeney *et al.*, 2008), and $BaFe_2As_2$ (Matan *et al.*, 2009), a spin gap due to magnetic iron anisotropy was identified. In addition, the low-energy spin waves were described by either a local-moment Heisenberg Hamiltonian (McQueeney *et al.*, 2008; Zhao *et al.*, 2008a) or the spin-excitation continuum from itinerant electrons (Diallo *et al.*, 2009; Matan *et al.*, 2009). However, these measurements were unable to reach spin waves near the zone boundary and thus did not allow a conclusive determination of the effective nearest and next nearest neighbor magnetic exchange couplings denoted as J_{1a}/J_{1b} and J_2, respectively [Fig. 4(b)]. In the itinerant picture of the magnetism in iron pnictides (Mazin, 2010; Hirschfeld, Korshunov, and Mazin, 2011), spin waves from the AF ordered phase should arise from quasiparticle excitations between the electron and hole Fermi surfaces and form a spin-excitation continuum at high energies (Kaneshita and Tohyama, 2010). In the initial neutron time-of-flight experiments on $CaFe_2As_2$, spin waves up to an energy of $\sim$100 meV were measured and found to fit a Heisenberg Hamiltonian (Diallo *et al.*, 2009). However, no spin-wave signals were found for energies above 100 meV consistent with *ab initio* calculations of the dynamic magnetic susceptibility, indicating that the high-energy spin excitations are dominated by the damping of spin waves through particle-hole excitations (Diallo *et al.*, 2009).

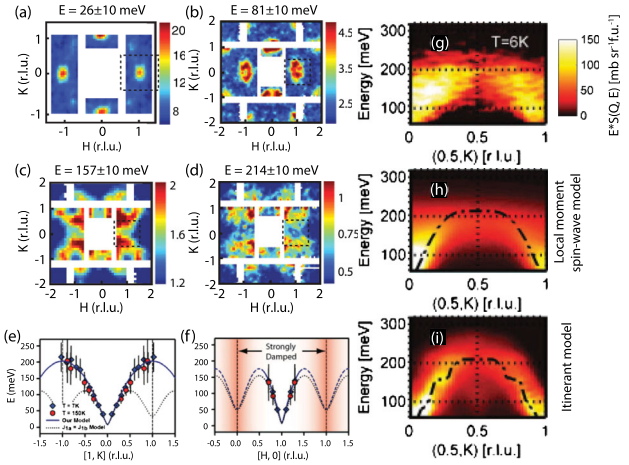

FIG. 8 (color online). Spin waves in $BaFe_2As_2$ and $SrFe_2As_2$ determined from neutron time-of-flight spectrometry. (a) Spin waves at $E = 26 \pm 10$ meV. The presence of peaks at wave vectors $\mathbf{Q}_{AF} = (\pm 1, 0)$ and $(0, \pm 1)$ is due to the twinning effect. The white regions are detector gaps. Similar spin waves at (b) $E = 81 \pm 10$, (c) 157 ± 10, and (d) 214 ± 10 meV (Harriger *et al.*, 2011). The color bars indicate magnetic scattering in absolute units of mbarn sr^{-1} meV^{-1} $\mathrm{f.u.}^{-1}$. (e) Spin-wave dispersion curves and fits using a Heisenberg Hamiltonian with different exchange couplings along the $[1, K]$ direction. (f) Similar Heisenberg Hamiltonian fits along the $[H, 0]$ direction (Harriger *et al.*, 2011). (g) Spin waves in the energy and wave vector cuts along the $[0.5, K]$ direction for $SrFe_2As_2$ (Ewings *et al.*, 2011). (h) The dashed line shows a fit of a Heisenberg Hamiltonian assuming one set of exchange coupling constants. (i) A RPA calculation of $\chi''(\mathbf{Q}, \omega)$ based on a five-band model (Ewings *et al.*, 2011). The reciprocal space notation in (g)–(i) is tetragonal where $\mathbf{Q}_{AF} = (0.5, 0.5)$, different from those in (a)–(f).

In subsequent neutron scattering experiments on $CaFe_2As_2$ (Zhao *et al.*, 2009), $BaFe_2As_2$ (Harriger *et al.*, 2011), and $SrFe_2As_2$ using more sample mass (Ewings *et al.*, 2011), spin waves were mapped out throughout the Brillouin zone and the zone boundary energy scales were found to be around 220 meV. Figures 8(a)–8(d) show images of spin waves in $BaFe_2As_2$ in the AF ordered state at energies of $E = 26 \pm 10$, 81 ± 10, 157 ± 10, and 214 ± 10 meV, respectively (Harriger *et al.*, 2011). With increasing energy, spin waves become diffusive but one can still see clear excitations near the zone boundary at $E = 214$ meV, different from the earlier experiment (Diallo *et al.*, 2009). Figures 8(e) and 8(f) show spin-wave dispersions of $BaFe_2As_2$ along the in-plane $[1, K]$ and $[H, 0]$ directions. Using a Heisenberg Hamiltonian with anisotropic spin-wave damping, one can fit the entire spin-wave spectrum with a large in-plane nearest neighbor magnetic exchange anisotropy ($J_{1a} > 0$, $J_{1b} < 0$) and finite next nearest neighbor exchange coupling ($J_2 > 0$) (Zhao *et al.*, 2009; Harriger *et al.*, 2011). The details of a Heisenberg Hamiltonian for spin waves have been discussed by Diallo *et al.* (2009), Zhao *et al.* (2009), and Harriger *et al.* (2011). The outcomes of the fits with anisotropic in-plane magnetic exchanges are shown as solid lines in Fig. 8(e), while the dashed lines are calculations assuming isotropic in-plane magnetic exchange couplings. The discovery of large in-plane exchange anisotropy is surprising given the small orthorhombic lattice distortion in the AF ordered state (Wysocki, Belashchenko, and Antropov, 2011). Only by probing spin waves at high energies near the zone boundary can one conclusively determine the effective magnetic exchange couplings in the system. Different magnetic structures and spin exchange couplings in iron-based materials have been studied using a localized moment model with different nearest and next nearest neighbor exchange couplings (Hu *et al.*, 2012).

Although spin waves in $CaFe_2As_2$ (Zhao *et al.*, 2009) and $BaFe_2As_2$ (Harriger *et al.*, 2011) can be modeled by a local-moment Heisenberg Hamiltonian, one still has to use anisotropic spin-wave damping characteristics of an itinerant electron system. In the neutron scattering work on spin waves of $SrFe_2As_2$ [Fig. 8(g)] (Ewings *et al.*, 2011), it was reported that a Heisenberg Hamiltonian that can fit the low-energy spin-wave data fails to describe the spectrum near the zone boundary [Fig. 8(h)]. The overall spin-wave spectrum is instead best described by an itinerant model with large spin-wave damping near the zone boundary [Fig. 8(i)] (Ewings *et al.*, 2011).

Similar to the 122 family of materials, NaFeAs, the parent compound of the 111 family of iron pnictides, has the collinear AF structure albeit with a greatly reduced ordered moment size (Li, de la Cruz *et al.*, 2009). Triple-axis neutron scattering experiments on single crystals of NaFeAs studied low-energy spin waves and found a small gap in the excitation

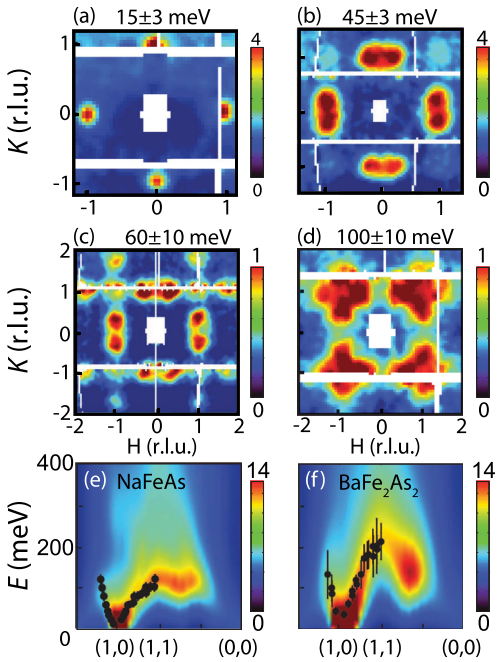

FIG. 9 (color online). Comparison of spin waves in NaFeAs and combined DFT and DMFT calculations. (a) Spin waves of NaFeAs at $E = 15 \pm 3$ meV. Similar spin waves at (b) $E = 45 \pm 3$, (c) 60 ± 10, and (d) 100 ± 10 meV. The magnetic intensities are in absolute units of mbarn sr^{-1} meV^{-1} $\mathrm{f.u.}^{-1}$. (e) The solid circles show the dispersion of spin waves, while the color plots are calculations from a combined DFT and DMFT theory. (f) Similar comparison for $BaFe_2As_2$. From Zhang *et al.*, 2014a.

spectrum (Park *et al.*, 2012; Song, Regnault *et al.*, 2013). Figure 9 summarizes the evolution of spin waves to the zone boundary as a function of increasing energy (Zhang *et al.*, 2014a). Compared with the spin-wave zone boundary energy of ∼220 meV in $BaFe_2As_2$ as shown in Fig. 8, spin waves in NaFeAs reach the zone boundary at the in-plane wave vector $\mathbf{Q} = (1, 1)$ around ∼110 meV [Fig. 9(d)]. This means that the overall magnetic excitation bandwidth in the 111 family is considerably lower than that of the 122 family of iron pnictides. Figures 9(e) and 9(f) compare the experimental and combined density functional theory and dynamical mean-field theory (DFT + DMFT) calculations of spin-wave dispersion of NaFeAs and $BaFe_2As_2$, respectively. The outcome suggests that the pnictogen height is correlated with the strength of electron-electron correlations and consequently the effective bandwidth of magnetic excitations in iron pnictides (Yin, Haule, and Kotliar, 2014; Zhang *et al.*, 2014a).

Figure 10 summarizes spin-wave measurements for the iron chalcogenide $Fe_{1+x}Te$ (Fruchart *et al.*, 1975; Bao *et al.*, 2009; S. L. Li *et al.*, 2009), the parent compound of the 11 family of iron-based superconductors (Lipscombe *et al.*, 2011; Zaliznyak *et al.*, 2011). The static magnetic order and spin excitations of $Fe_{1+x}Te$ are sensitive to the excess iron in the interstitial sites (Rodriguez *et al.*, 2010, 2011; Stock *et al.*, 2011; Wen *et al.*, 2011). This is rather different from the iron

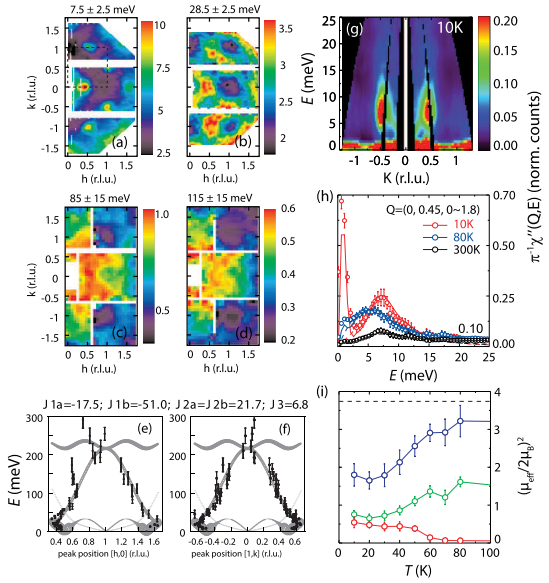

FIG. 10 (color online). Spin waves in $Fe_{1.05}Te$ and $Fe_{1.1}Te$. (a) Wave vector dependence of spin waves in $Fe_{1.05}Te$ at $E = 7.5 \pm 2.5$ meV. Similar spin waves at (b) $E = 28.5 \pm 2.5$, (c) 85 ± 15, and (d) 115 ± 15 meV (Lipscombe *et al.*, 2011). The diffusive nature of spin waves is clearly seen at high energies. (e), (f) Dispersion curves of spin waves along the $[H, 0]$ and $[1, K]$ directions and the Heisenberg Hamiltonian fits using nearest, next nearest, and next next nearest neighbor exchange couplings (Lipscombe *et al.*, 2011). (g) Energy and wave vector cut of spin waves in $Fe_{1.1}Te$. (h) Energy dependence of spin waves at different temperatures. (i) Temperature dependence of the integrated moments for $Fe_{1.1}Te$. The data suggest an increased total integrated moment on warming from 10 to 100 K across T_N and T_s. From Zaliznyak *et al.*, 2011.

pnictides, which cannot accommodate any excess iron in the crystal structure. For $Fe_{1.05}Te$ and $Fe_{1.1}Te$, the AF structure is commensurate bicollinear (Rodriguez *et al.*, 2011). Figures 10(a)–10(d) show the two-dimensional images of spin waves in $Fe_{1.05}Te$ at $E = 7.5 \pm 2.5$, 28.5 ± 2.5, 85 ± 15, and 115 ± 15 meV, respectively (Lipscombe *et al.*, 2011). The dispersion of spin waves is different from those of the 122 and 111 families and becomes diffuse for energies above 85 meV without well-defined excitations [Figs. 10(c) and 10(d)]. The solid lines in Figs. 10(e) and 10(f) show fits of the dispersion using a Heisenberg Hamiltonian assuming exchange couplings J_{1a}, J_{1b}, J_2, and J_3 (Lipscombe *et al.*, 2011). In a separate neutron scattering experiment, Zaliznyak *et al.* (2011) found that the low-energy spin excitations can be well described by liquidlike spin plaquette correlations [Fig. 10(g)]. Furthermore, the integrated magnetic excitation intensity increases on warming [Fig. 10(h)]. The effective spin per Fe $S \approx 1$ at $T \approx 10$ K in the AF ordered phase grows to $S \approx 3/2$ at $T = 80$ K in the paramagnetic phase, suggesting that the local magnetic moments are entangled with the itinerant electrons in the system [Fig. 10(i)] (Zaliznyak *et al.*, 2011).

Of all the iron-based superconductors, alkali iron selenides $A_xFe_{2-y}Se_2$ (Guo *et al.*, 2010; Fang *et al.*, 2011) are unique in that superconductivity in this class of materials always coexists with a static long-range AF order with a large moment and high Néel temperature (Bao *et al.*, 2011; M. Wang *et al.*, 2011; Ye *et al.*, 2011; May *et al.*, 2012; Zhao *et al.*, 2012). Although there is ample evidence indicating that the superconducting alkali iron selenides are mesoscopically phase separated from the insulating $A_2Fe_4Se_5$ phase with the $\sqrt{5} \times \sqrt{5}$ block AF structure as shown in Fig. 2(d) (Ksenofontov *et al.*, 2011; W. Li *et al.*, 2011; Ricci *et al.*, 2011; Charnukha *et al.*, 2012; Shermadini *et al.*, 2012; Shoemaker *et al.*, 2012; Speller *et al.*, 2012; Texier *et al.*, 2012; Z. W. Wang *et al.*, 2012; Carr *et al.*, 2014), there is still no consensus on the chemical and magnetic structures of their parent compounds (M. Wang *et al.*, 2011; Ye *et al.*, 2011; May *et al.*, 2012; Zhao *et al.*, 2012). Assuming that the insulating $A_2Fe_4Se_5$ phase is the parent compound of the superconducting $A_xFe_{2-y}Se_2$, its spin waves have been mapped out by several groups (M. Y. Wang *et al.*, 2011; Chi *et al.*, 2013; Xiao *et al.*, 2013). Compared with spin waves in iron pnictides and iron chalcogenides (Figs. 7–10), the dispersion of the spin waves in insulating $A_2Fe_4Se_5$ has two optical branches at high energies and one acoustic branch at low energy, where the arrows are wave vector scales and the thin dashed line separates the vertical energy scale for the acoustic and low-energy optical spin waves from the high-energy optical spin waves [Figs. 11(a)–11(c)] (M. Y. Wang *et al.*, 2011). By integrating the energy dependence of the local dynamic susceptibility in $Rb_{0.89}Fe_{1.58}Se_2$ [Fig. 11(d)], it was found that the total moment sum rule is exhausted for magnetic scattering at energies below 250 meV. Therefore, spin waves in insulating $Rb_{0.89}Fe_{1.58}Se_2$ can be regarded as a classic local-moment system where a Heisenberg Hamiltonian is an appropriate description of the spin-wave spectrum.

On the other hand, if the semiconducting AF phase with rhombus iron vacancy order [Fig. 2(e)] is the parent compound (Zhao *et al.*, 2012; Wang *et al.*, 2014), one finds that spin

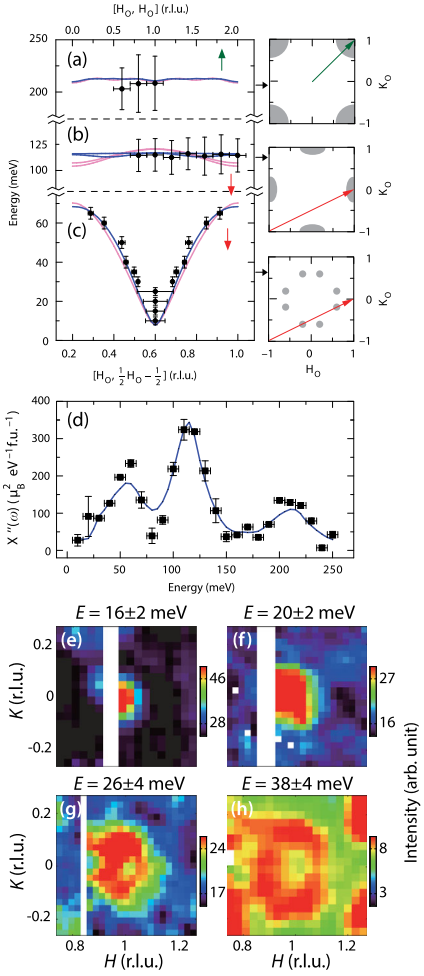

FIG. 11 (color online). Spin waves in the insulating 245 and semiconducting 234 phases. (a)–(c) Spin-wave dispersions in the insulating $Rb_{0.89}Fe_{1.58}Se_2$ (M. Y. Wang *et al.*, 2011). The solid circles are data from the cut directions marked by the arrows in the right panels of (a)–(c). The solid lines are fits from a Heisenberg Hamiltonian considering nearest, the next nearest, and next next nearest neighbor exchange couplings (M. Y. Wang *et al.*, 2011). (d) The energy dependence of the local dynamic susceptibility, where the solid line is the calculated value from the Heisenberg Hamiltonian. The total moment sum rule appears to be satisfied (M. Y. Wang *et al.*, 2011). (e)–(h) The wave vector dependence of spin waves from the semiconducting $K_{0.85}Fe_{1.54}Se_2$ (Zhao *et al.*, 2014).

waves of the system are rather close to those of iron pnictides. Figures 11(e)–11(h) show the evolution of spin waves as a function of increasing energy for the semiconducting $K_{0.85}Fe_{1.54}Se_2$ with collinear AF order and $T_N = 280$ K (Zhao *et al.*, 2014). The data agree well with calculations using a Heisenberg Hamiltonian. A comparison of the observed spin-wave spectrum in this system with those of $CaFe_2As_2$ single crystals (Zhao *et al.*, 2009) reveals remarkable similarities, thus suggesting similar effective magnetic exchange couplings in these systems (Zhao *et al.*, 2014).

Table II summarizes the effective magnetic exchange couplings for the parent compounds of known iron-based superconductors. We also list the effective magnetic exchange couplings for La_2CuO_4, the parent compound of copper oxide superconductors. They are dominated by the large nearest neighbor and weak next nearest neighbor magnetic exchange couplings (Fig. 4). For the parent compounds of iron-based superconductors, it is instructive to compare their effective magnetic exchange couplings. In spite of their dramatically different AF structures summarized in Figs. 1–3, they all appear to have similar next nearest neighbor magnetic exchange couplings (see Table II). This is consistent with the idea that the next nearest neighbor coupling J_2 is mainly determined by a local superexchange mechanism mediated by As or Se/Te, regardless of their metallic or insulating ground states (Abrahams and Si, 2011; Hu and Ding, 2012).

B. Neutron spin resonance and its relationship with superconductivity

The neutron spin resonance is a collective magnetic excitation occurring below T_c with a temperature dependence similar to the superconducting order parameter (Eschrig, 2006). First discovered in hole-doped $YBa_2Cu_3O_{6+x}$ copper oxide superconductors (Rossat-Mignod *et al.*, 1991), the resonance is located near the AF ordering wave vector $\mathbf{Q}_{AF}$ of the nonsuperconducting parent compound and occurs at an energy related to the superconducting T_c (Dai *et al.*, 2000; Wilson, Dai *et al.*, 2006) or gap energy (Yu *et al.*, 2009). It has been argued that the mode is a signature of the d-wave pairing as a result of quasiparticle excitations between the sign reversed d-wave superconducting gaps (Eschrig, 2006). Soon after the discovery of iron pnictide superconductors (Kamihara *et al.*, 2008), a neutron spin resonance was found in powder samples of $Ba_{0.6}K_{0.4}Fe_2As_2$ (Christianson *et al.*, 2008). Since the resonance occurs below T_c at the momentum transfer ($Q = 1.15$ Å^{-1}) close to $\mathbf{Q}_{AF}$ in $BaFe_2As_2$ [Figs. 12(a) and 12(b)] (Christianson *et al.*, 2008), the mode is believed to arise from the sign reversed quasiparticle excitations between the hole and electron Fermi surfaces near the Γ and M points in reciprocal space, respectively (Figs. 12–14) (Mazin, 2010; Hirschfeld, Korshunov, and Mazin, 2011). In subsequent inelastic neutron scattering experiments on single crystals of electron-doped $Ba(Fe_{1-x}Co_x)_2As_2$ (Lumsden *et al.*, 2009; Inosov *et al.*, 2010) and $BaFe_{2-x}Ni_xAs_2$ superconductors (Chi *et al.*, 2009; Li, Chen *et al.*, 2009), the resonance was indeed found at the in-plane AF ordering wave vector $\mathbf{Q}_{AF} = (1, 0)$ [Fig. 12(a)]. Similar measurements on powder samples of $LaFeAsO_{1-x}F_x$ (Ishikado *et al.*, 2009; Shamoto *et al.*, 2010; Wakimoto *et al.*, 2010) and molecular-intercalated FeSe (Taylor *et al.*, 2013) also revealed resonancelike spin excitations below T_c. Figure 12(c) shows the temperature dependence of the imaginary part of the dynamic susceptibility $\chi''(\mathbf{Q}_{AF}, \omega)$ for energies below ($E = \hbar\omega = 3$ meV), at ($E = 9.5$ meV), and above ($E = 16$ meV) the resonance in superconducting $BaFe_{1.85}Co_{0.15}As_2$ ($T_c = 25$ K). It is clear that the intensity gain of the resonance below T_c is at the expense of opening a spin gap at energies below it. By carefully monitoring the temperature dependence of the resonance, Inosov *et al.* (2010) suggested that the energy of the mode decreases with increasing temperature and may be directly correlated with the temperature dependence of the superconducting gap energy [Fig. 12(d)]. However,

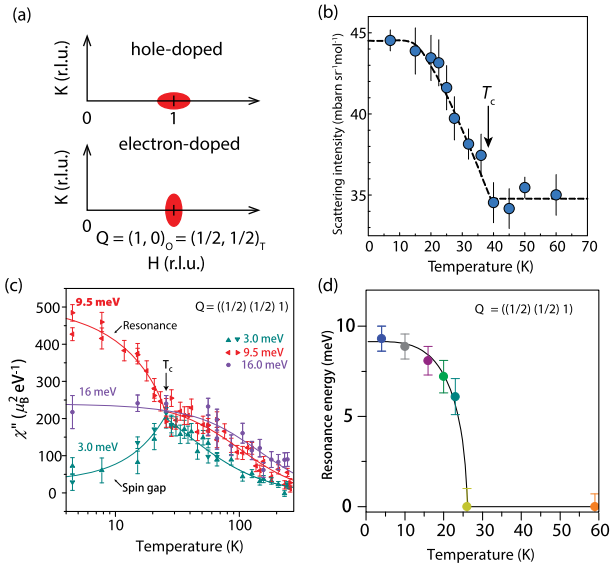

FIG. 12 (color online). Neutron spin resonance in electron- and hole-doped iron pnictides. (a) The schematic drawings of the wave vector dependence of the low-energy spin excitations in optimal hole- (upper panel) and electron-doped (lower panel) superconducting iron pnictides. (b) Temperature dependence of the resonance at $E = 16$ meV, showing clear superconducting order parameterlike enhancement below T_c for a powder sample of $Ba_{0.6}K_{0.4}Fe_2As_2$ (Christianson *et al.*, 2008). (c) Temperature dependence of the magnetic scattering at energies $E = 3.0$, 9.5, and 16 meV for optimally electron-doped superconducting $BaFe_{1.85}Co_{0.15}As_2$ ($T_c = 25$ K) (Inosov *et al.*, 2010). While magnetic intensity at the resonance energy ($E = 9.5$ meV) shows a clear enhancement below T_c at the expense of opening a spin gap at $E = 3.0$ meV, the scattering at $E = 16$ meV is not sensitive to superconductivity. (d) Temperature dependence of the resonance energy for $BaFe_{1.85}Co_{0.15}As_2$ (Inosov *et al.*, 2010).

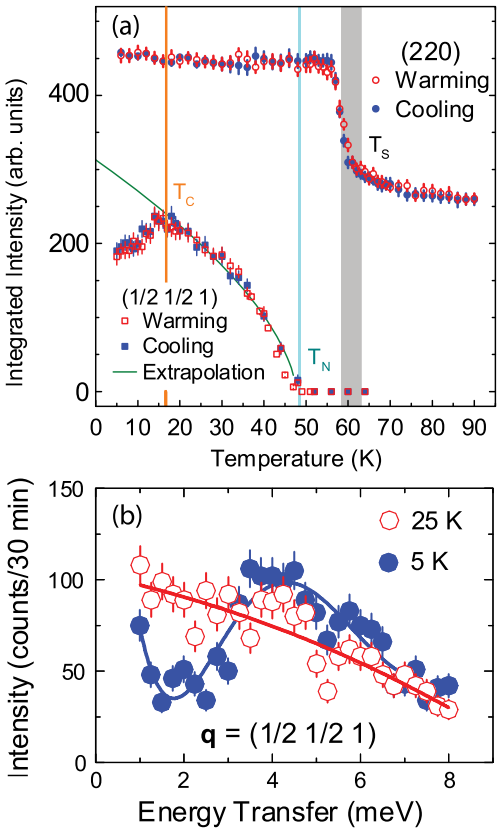

FIG. 13 (color online). Effect of electron doping on magnetism and superconductivity in electron underdoped iron pnictides. (a) Temperature dependence of the nuclear (2,2,0) and $(1/2, 1/2, 1)$ (in tetragonal notation) magnetic scattering in the electron underdoped $Ba(Fe_{0.953}Co_{0.047})_2As_2$ ($T_c = 17$ K). The structural, magnetic, and superconducting transitions are clearly marked. (b) A weak resonance appears below T_c at $E = 4$ meV. From Pratt *et al.*, 2009.

recent experiments on the nearly optimally doped $BaFe_{1.904}Ni_{0.096}As_2$ superconductor found that the resonance energy is essentially temperature independent on warming (Luo, Lu *et al.*, 2013), different from that of $BaFe_{1.85}Co_{0.15}As_2$ (Inosov *et al.*, 2010).

In the electron underdoped regime where static AF order coexists and competes with superconductivity [Figs. 5(b) and 5(d)], the static AF order occurs at a lower temperature than T_s. Figure 13(a) shows the temperature dependence of the nuclear peak intensity at (2,2,0) and magnetic Bragg scattering at $\mathbf{Q}_{\mathrm{AF}}$ for underdoped $Ba(Fe_{0.953}Co_{0.047})_2As_2$ ($T_c = 17$ K) (Pratt *et al.*, 2009). In the high temperature tetragonal state, the observed neutron scattering intensity from a strong nuclear Bragg peak (2,2,0) is lower than that expected from the structure factor calculation due to multiple scattering effects, termed the neutron extinction effect (Hamilton, 1957). When the symmetry of the system is reduced from tegragonal to orthorhombic, there is a dramatic intensity gain below ~60 K arising from the release of the neutron extinction effect and the AF order occurs below $T_N \approx 48$ K. Upon entering into the superconducting state, the intensity of the static AF order decreases. Simultaneously, a weak neutron spin resonance appears at $E = 4$ meV [Fig. 13(b)], suggesting that the intensity gain of the mode arises from suppression of the static AF order and spin excitations at energies below the resonance (Christianson *et al.*, 2009; Pratt *et al.*, 2009). Application of a magnetic field which partially suppresses superconductivity will enhance the intensity of the static AF order and suppress the resonance (M. Y. Wang, Luo *et al.*, 2011). These results further suggest that the static AF order coexists and competes with superconductivity in electron underdoped iron pnictides.

From density functional theory calculations (Kuroki *et al.*, 2008; Mazin *et al.*, 2008) and angle resolved photoemission spectroscopy (ARPES) experiments on electron- and hole-doped iron pnictides (Richard *et al.*, 2011; Chen *et al.*, 2014), we know that Fermi surfaces in most of these materials are composed of hole-like pockets near Γ and electron-like pockets near M point at $\mathbf{Q}_{\mathrm{AF}} = (1, 0)$. The neutron spin resonance in iron pnictides at $\mathbf{Q}_{\mathrm{AF}} = (1, 0)$ can arise from the sign reversed quasiparticle excitations between the hole and electron Fermi surfaces in an s^{+-}-wave superconductor as shown in Fig. 14 (Mazin, 2010; Hirschfeld, Korshunov, and Mazin, 2011), exhibiting the same signature as the sign changed superconducting gap function in the d-wave copper oxides (Eschrig, 2006). With increasing electron doping, the hole and electron Fermi surfaces decrease and increase in size,

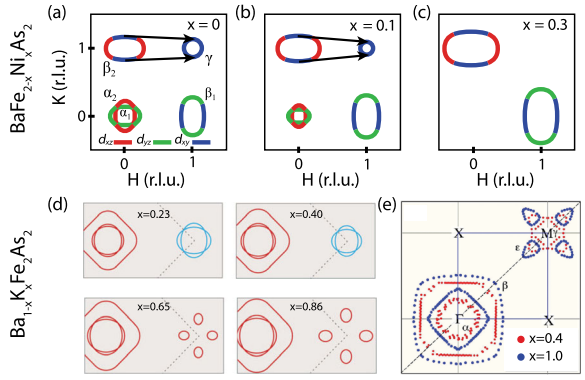

FIG. 14 (color online). The evolution of Fermi surfaces in electron- and hole-doped $BaFe_2As_2$. (a) Schematics of Fermi surfaces corresponding to $BaFe_2As_2$ with possible nesting vectors marked with arrows (Dai, Hu, and Dagotto, 2012). The d_{xz}, d_{yz}, and d_{xy} orbitals for different Fermi surfaces are shown. (b) Fermi surfaces when 10% electrons are doped into $BaFe_2As_2$ to form optimal superconductivity. (c) Fermi surfaces with 30% electron doping when superconductivity is suppressed (M. Wang *et al.*, 2013). (d) Schematics of Fermi surfaces for hole-doped $Ba_{1-x}K_xFe_2As_2$ with increasing K doping to $x = 0.23$ (upper left panel), 0.40 (upper right panel), 0.65 (lower left), and 0.86 (lower right panel) (Richard *et al.*, 2011). (e) A comparison of the Fermi surfaces for $x = 0.4$ and 1 in the folded Brillouin zone (Richard *et al.*, 2011).

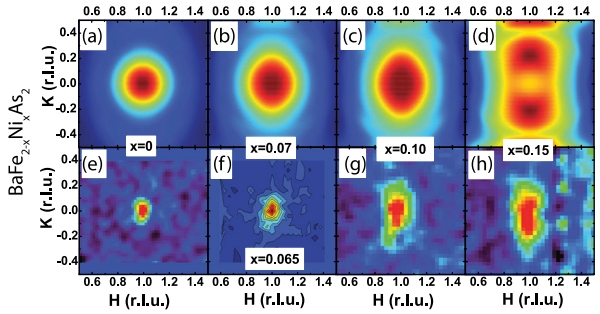

FIG. 15 (color online). Comparison of wave vector evolution of the low-energy spin excitations in electron-doped $BaFe_{2-x}Ni_xAs_2$ with the RPA calculation based on a rigid band shift model. (a)–(d) RPA calculation results obtained for an energy $E = 8$ meV for electron dopings of $x = 0, 0.07, 0.1$, and 0.15, respectively. As the doping increases from (a) to (d), one clearly sees an enhancement of the anisotropy in spin excitations (transverse elongation). (e)–(h) In-plane wave vector dependence of the spin excitations at $E = 8$ meV for $x = 0, 0.065, 0.1$, and 0.15, respectively (Luo *et al.*, 2012). For the electron-overdoped $x = 0.15$ sample, two transverse incommensurate peaks are expected from the RPA calculation. This is indeed observed in neutron scattering experiments (Luo, Lu *et al.*, 2013).

respectively [Figs. 14(a)–14(c)]. Similarly, the hole Fermi pockets at the Γ point increase in size with increasing hole doping, while the electron Fermi surfaces exhibit a Lifshitz transition at M point before becoming hole overdoped KFe_2As_2 [Figs. 14(d)–14(f)] (Chen *et al.*, 2014).

Using the random phase approximation (RPA) based on a three-dimensional tight-binding model in the local density approximation (Graser *et al.*, 2010), calculations can predict the momentum anisotropy of the low-energy spin excitations and the resonance (Park *et al.*, 2010). For electron-doped $BaFe_{2-x}T_xAs_2$, low-energy spin excitations become progressively elongated ellipses along the transverse direction relative to the spin waves in $BaFe_2As_2$ due to the enhancement of the intraorbital, but interband, pair scattering process between the d_{xy} orbitals [Figs. 14(a) and 14(b)] (Zhang, Sknepnek, and Schmalian, 2010). Figure 15 shows the comparison of the RPA calculations and experimentally measured in-plane spin-excitation anisotropy in $BaFe_{2-x}Ni_xAs_2$ superconductors (Luo, Yamani *et al.*, 2012), confirming that the quasiparticle excitations between the hole and electron Fermi surfaces are consistent with the wave vector evolution of the low-energy spin excitations (Luo, Lu *et al.*, 2013).

In the case of hole-doped materials, RPA calculations predicted that spin excitations should be longitudinally elongated and thus rotated 90° from those of the electron-doped $BaFe_{2-x}T_xAs_2$ (Park *et al.*, 2010). Inelastic neutron scattering experiments on hole-doped single crystals of superconducting $Ba_{0.67}Ka_{0.33}Fe_2As_2$ ($T_c = 38$ K) reveal longitudinally elongated spin excitations for energies near the resonance, consistent with RPA calculations (C. L. Zhang *et al.*, 2011). Figures 16(a)–16(h) plot the hole-doping dependence of the resonance obtained using high-quality powder samples of $Ba_{1-x}K_xFe_2As_2$ (Avci *et al.*, 2011; Castellan *et al.*, 2011). Although these measurements do not provide precise information concerning the wave vector dependence of the spin excitations, they do give the hole-doping evolution of the total momentum transfer of the mode. With increasing hole doping, the sharp resonance centered at $Q \approx 1.25$ Å^{-1} for $x = 0.3$ [Figs. 16(a) and 16(c)] becomes broader in Q and splits into two peaks for $x = 0.7$ and 0.9 [Figs. 16(e)–16(h)] (Castellan *et al.*, 2011). This is consistent with the RPA result that hole doping induces longitudinal incommensurate spin excitations (Castellan *et al.*, 2011). Indeed, neutron scattering experiments on hole-overdoped KFe_2As_2 found two incommensurate spin-excitation peaks located longitudinally away from $\mathbf{Q}_{AF}$ [Figs. 16(i)–16(k)], again confirming the notion that low-energy spin excitations in hole- and electron-doped iron pnictides are controlled by quasiparticle excitations between the hole and electron Fermi surfaces (Lee *et al.*, 2011).

In addition to electron or hole doping to $BaFe_2As_2$, isoelectronic substitution to $BaFe_2As_2$ by replacing Fe with Ru (Thaler *et al.*, 2010) or As with P (Jiang *et al.*, 2009) can also induce superconductivity. Compared with the electron-doped $BaFe_{2-x}T_xAs_2$, isoelectronic substitution is much less effective in suppressing AF order and inducing superconductivity. Inelastic neutron scattering experiments on $BaFe_{2-x}Ru_xAs_2$ near optimal superconductivity reveal a neutron spin resonance similar to electron-doped $BaFe_{2-x}T_xAs_2$, but with greatly damped intensity, possibly due to the weakening of the electron-electron correlations by Ru doping (Zhao *et al.*, 2013). In the case of $BaFe_2(As_{1-x}P_x)_2$, initial neutron scattering experiments on powder samples with $T_c = 30$ K revealed the presence of a resonance at $E \approx 12$ meV (Ishikado *et al.*, 2011). Figures 17(a) and 17(b) show the energy dependence of $\chi''(\mathbf{Q}, \omega)$ above and below T_c, respectively, obtained for

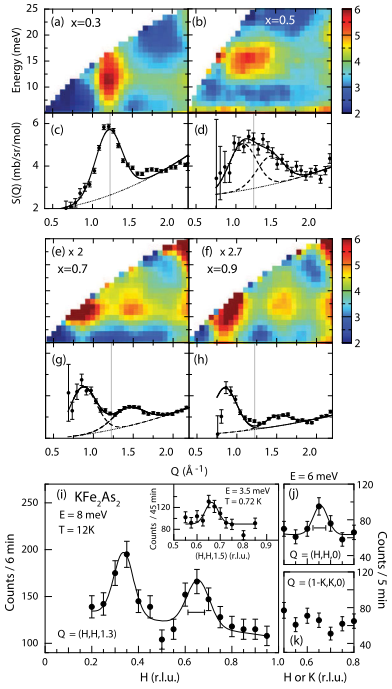

FIG. 16 (color online). The K-doping evolution of the neutron spin resonance and low-energy spin excitations in $Ba_{1-x}K_xFe_2As_2$. (a) Inelastic neutron scattering experiments on superconductivity-induced low-energy spin excitations of powder samples in $Ba_{1-x}K_xFe_2As_2$ at $x = 0.3$. A clear resonance is seen around 12 meV and $Q = 1.25$ Å^{-1} as shown in (c). (b), (d) The resonance becomes broader in Q at $x = 0.5$ and splits into two peaks at different wave vectors at (e), (g) $x = 0.7$ and (f), (h) $x = 0.9$ due to the changing Fermi surfaces (Castellan *et al.*, 2011). (i) Longitudinal scans along the $[H, H, 1.3]$ direction above T_c at $E = 8$ meV for single crystals of KFe_2As_2. Two incommensurate peaks are seen. The inset shows a similar scan below T_c at $E = 3.5$ meV. (j) Longitudinal and (k) transverse scans at $E = 6$ meV (Lee *et al.*, 2011).

single crystals of $BaFe_2As_{1.32}P_{0.68}$ ($T_c = 29.5$ K) (C. H. Lee *et al.*, 2013). In the normal state, $\chi''(\mathbf{Q}, \omega)$ is featureless and changes only slightly at different momentum transfers along the c axis ($L = 0, 0.25, 0.5, 0.75, 1$). Upon entering into the superconducting state, a neutron spin resonance is formed and its energy is significantly dispersive along the c axis [Fig. 17(b)] (C. H. Lee *et al.*, 2013). Since the bandwidth of the dispersion becomes larger upon approaching the AF ordered phase, the dispersive feature may arise from the three-dimensional AF spin correlations in the undoped parent (C. H. Lee *et al.*, 2013).

So far, most of the neutron scattering work has focused on single crystals of the electron- or hole-doped $BaFe_2As_2$ family of materials. For the $NaFe_{1-x}Co_xAs$ family of materials (Parker *et al.*, 2010; Tan *et al.*, 2013), the air sensitive nature of these materials makes it difficult to perform inelastic neutron scattering experiments (Tanatar *et al.*, 2012). By using hydrogen free glue to coat the samples, neutron scattering experiments can be carried out to study the evolution of spin excitations in $NaFe_{1-x}Co_xAs$ (Park *et al.*, 2012; Song, Regnault *et al.*, 2013). From ARPES experiments (Liu *et al.*, 2011; Ge *et al.*, 2013), it was found that the

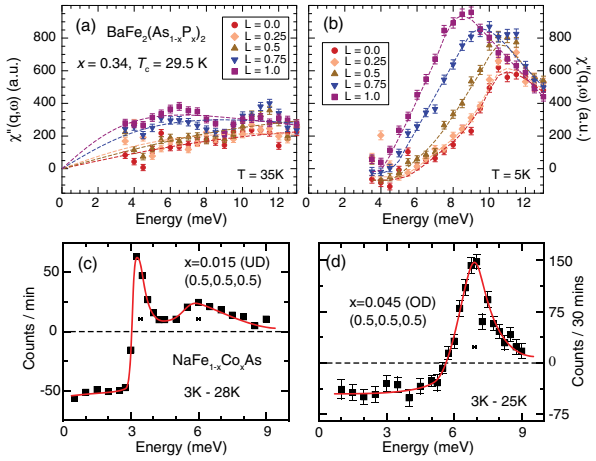

FIG. 17 (color online). The wave vector and energy dependence of the neutron spin resonance for $BaFe_2(As_{1-x}P_x)_2$ and $NaFe_{1-x}Co_xAs$. (a) The energy dependence of the dynamic susceptibility at the in-plane AF wave vector position and different L values above T_c for $BaFe_2(As_{1-x}P_x)_2$ with $x = 0.34$. (b) Identical scans at temperature $T = 5$ K well below T_c. The resonance shows clear dispersion for different values of L (C. H. Lee *et al.*, 2013). (c) The energy dependence of the superconductivity-induced double resonance for an underdoped (UD) $NaFe_{1-x}Co_xAs$ with $x = 0.015$. There are two peaks in the energy scan at $E = 3.5$ and 6 meV. (d) The double resonance in the underdoped sample becomes a single resonance for electron-overdoped $NaFe_{1-x}Co_xAs$ with $x = 0.045$ (C. L. Zhang *et al.*, 2013b).

superconducting gap in the electron Fermi pockets of the underdoped regime near $x = 0.0175$ has a large anisotropy, which is absent in the hole Fermi pocket. The superconducting gap anisotropy disappears upon increasing x to 0.045. Figures 17(c) and 17(d) show the intensity gain of the resonance below T_c for underdoped $x = 0.015$ (C. L. Zhang *et al.*, 2013b) and overdoped $x = 0.045$ (Zhang *et al.*, 2013a), respectively. Instead of a single resonance peak, superconductivity induces a sharp resonance at $E_{r1} = 3.25$ meV and a broad resonance at $E_{r2} = 6$ meV (C. L. Zhang *et al.*, 2013b). Similar measurements on electron-overdoped $x = 0.045$ reveal only one sharp resonance (Zhang *et al.*, 2013a). The appearance of the double resonance and the superconducting gap anisotropy in the underdoped sample was interpreted as originating from either the orbital dependence of the superconducting pairing (C. L. Zhang *et al.*, 2013b; Yu, Zhu, and Si, 2014) or superconductivity coexisting with static AF order in the iron pnictides (Rowe *et al.*, 2012; Lv, Moreo, and Dagotto, 2014).

C. The electron and hole-doping evolution of the spin excitations in the $BaFe_2As_2$ family of iron pnictides

To understand the interplay between magnetism and superconductivity in iron pnictides, one must first determine the electron and hole-doping evolution of the spin-excitation spectra throughout the Brillouin zone. Since single crystals of electron and hole-doped $BaFe_2As_2$ are available, one can systematically map out the evolution of spin excitations at

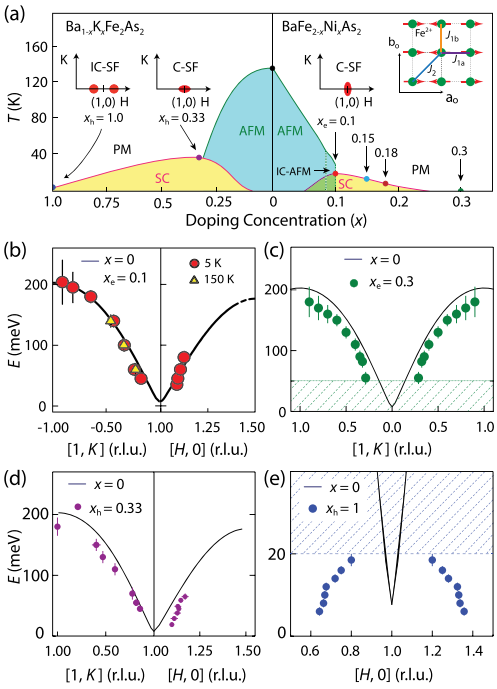

FIG. 18 (color online). The evolution of spin-excitation dispersions for hole- and electron-doped $BaFe_2As_2$. (a) The electronic phase diagram of electron- and hole-doped $BaFe_2As_2$, where the arrows indicate the doping levels of inelastic neutron scattering experiments. The right inset shows the crystal and AF spin structures of $BaFe_2As_2$. The inset above $x_e = 0.1$ shows the transversely elongated ellipse representing the low-energy spin excitations in electron-doped $BaFe_{2-x}Ni_xAs_2$ in the (H, K) plane of reciprocal space. The left insets show the evolution of low-energy spin excitations in hole-doped $Ba_{1-x}K_xFe_2As_2$ in the (H, K) plane. C-SF and IC-SF indicate commensurate and incommensurate spin fluctuations, respectively. (b)–(e) The solid lines in the figure are spin-wave dispersions of the undoped $BaFe_2As_2$ along the two high-symmetry directions. The symbols in (b)–(e) are dispersions of spin excitations for $BaFe_{1.9}Ni_{0.1}As_2$, $BaFe_{1.7}Ni_{0.3}As_2$, $Ba_{0.67}K_{0.33}Fe_2As_2$, and KFe_2As_2, respectively. The shaded areas indicate vanishing spin excitations. From M. Wang *et al.*, 2013.

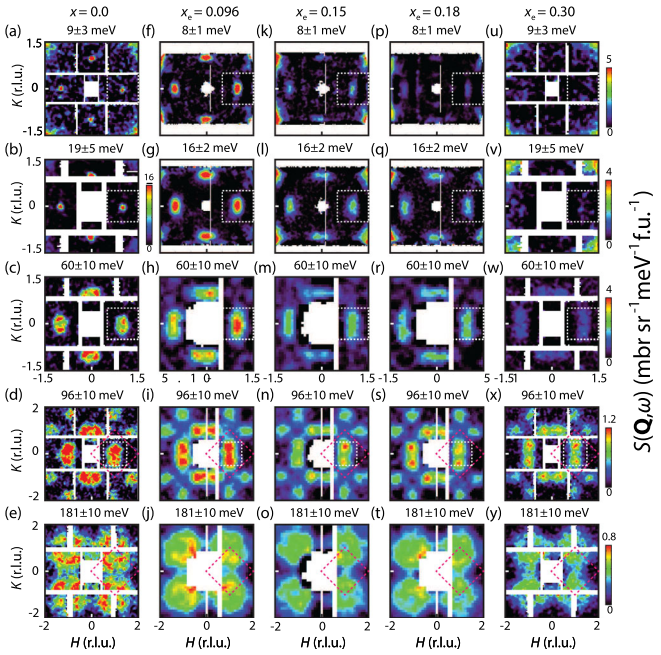

FIG. 19 (color online). Constant-energy slices through magnetic excitations of electron-doped $BaFe_{2-x}Ni_xAs_2$ iron pnictides at different energies. The color bars represent the vanadium normalized absolute spin-excitation intensity in the units of mbarn sr^{-1} meV^{-1} f u^{-1}. (a)–(e) Spin waves in $BaFe_2As_2$ at excitation energies of $E = 9 \pm 3$, 19 ± 5, 60 ± 10, 96 ± 10, and 180 ± 10 meV (Harriger *et al.*, 2011). Spin waves peak at the AF ordering wave vectors $\mathbf{Q}_{AF} = (\pm 1, 0)$ in the orthorhombic notation. Spin waves are also seen at $\mathbf{Q}_{AF} = (0, \pm 1)$ due to the twin domains of the orthorhombic structure. (f)–(j) Two-dimensional images of spin excitations for $BaFe_{1.904}Ni_{0.096}As_2$ at $E = 8 \pm 1$, 16 ± 2, 60 ± 10, 96 ± 10, and 181 ± 10 meV. Identical slices to those of (f)–(j) for (k)–(o) $BaFe_{1.85}Ni_{0.15}As_2$ and (p)–(t) $BaFe_{1.82}Ni_{0.18}As_2$ (Luo, Yamani *et al.*, 2012). (u)–(y) Constant-energy slices through magnetic excitations of electron-overdoped doped nonsuperconducting $BaFe_{1.7}Ni_{0.3}As_2$ at $E = 9 \pm 3$, 19 ± 5, 60 ± 10, 96 ± 10, and 181 ± 10 meV (M. Wang *et al.*, 2013). The white dashed boxes indicate wave vector integration range at low energies, while the colored dashed boxes in (d)–(h) mark the integration range for high-energy spin excitations.

different electron or hole-doping levels marked with arrows in the phase diagram [Fig. 18(a)] (Harriger *et al.*, 2011; Lee *et al.*, 2011; Liu *et al.*, 2012; Tucker *et al.*, 2012a; Luo, Lu *et al.*, 2013; M. Wang *et al.*, 2013; Chen *et al.*, 2014). The solid lines in Figs. 18(b)–18(e) show the dispersion of spin waves in $BaFe_2As_2$ along the $[1, K]$ and $[H, 0]$ directions (Harriger *et al.*, 2011). Upon electron doping to induce optimal superconductivity, spin excitations become broader at low energies ($E \leq 80$ meV) and couple to superconductivity via the resonance while remaining almost unchanged at high energies ($E > 80$ meV) (Liu *et al.*, 2012; Tucker *et al.*, 2012a). The circles and triangles in Fig. 18(b) show spin-excitation dispersions of the optimally electron-doped $BaFe_{1.9}Ni_{0.1}As_2$ at $T = 5$ and 150 K, respectively (Liu *et al.*, 2012). Figure 18(c) shows the dispersions of spin excitations of the electron-overdoped nonsuperconducting $BaFe_{1.7}Ni_{0.3}As_2$, where a large spin gap forms for energies below ~50 meV (M. Wang *et al.*, 2013). Figures 18(d) and 18(e) show the dispersions of spin excitations for optimally hole-doped $Ba_{0.67}K_{0.33}Fe_2As_2$ and hole-overdoped KFe_2As_2, respectively (M. Wang *et al.*, 2013). While electron doping does not much affect the high-energy spin excitations and dispersion, hole doping suppresses the high-energy spin excitations.

Figure 19 reveals the evolution of the two-dimensional constant-energy images of spin excitations in the (H, K) plane at different energies as a function of electron doping for $BaFe_{2-x}Ni_xAs_2$ (Harriger *et al.*, 2011; Luo, Lu *et al.*, 2013; M. Wang *et al.*, 2013). In undoped $BaFe_2As_2$, there is an anisotropy spin gap below ~15 meV, thus there is essentially no signal at $E = 9 \pm 3$ meV [Fig. 19(a)] (Matan *et al.*, 2009). For nearly optimally electron-doped $x = 0.096$, the spin gap is suppressed and low-energy spin excitations are dominated by the resonance [Fig. 19(f)] (Chi *et al.*, 2009; Li, Chen *et al.*, 2009; Lumsden *et al.*, 2009; Inosov *et al.*, 2010; Luo, Yamani

et al., 2012). In electron-overdoped $BaFe_{2-x}Ni_xAs_2$ with $x = 0.15$ ($T_c = 14$ K) and 0.18 ($T_c = 8$ K), spin excitations at $E = 8 \pm 1$ meV become weaker and more transversely elongated [Figs. 19(k) and 19(p)] (Luo, Lu *et al.*, 2013). For the nonsuperconducting $x = 0.3$ sample, a large spin gap forms in the low-energy excitation spectra [Fig. 19(u)]. Figures 19(b)–19(e), 19(g)–19(j), 19(q)–19(t), and 19(v)–19(y) show the evolution of spin excitations at different energies for $BaFe_{2-x}Ni_xAs_2$ with $x = 0, 0.096, 0.15, 0.18$, and 0.30, respectively. While electron doping modifies spin excitations at energies below $E = 96 \pm 10$ meV, high-energy spin excitations remain similar and soften only slightly.

Figure 20 shows the constant-energy images of spin excitations as a function of hole doping. For pure KFe_2As_2, incommensurate spin excitations along the longitudinal direction are seen at $E = 8 \pm 3$ meV [Fig. 20(a)] and 13 ± 3 meV [Fig. 20(b)] (Lee *et al.*, 2011). However, spin excitations become much weaker at $E = 53 \pm 8$ meV (M. Wang *et al.*, 2013). For optimally hole-doped $Ba_{0.67}K_{0.33}Fe_2As_2$, the low-energy spin excitations change from longitudinally elongated ellipses at $E = 5 \pm 1$ meV [Fig. 20(d)] to transversely elongated ellipses at $E = 50 \pm 2$ meV [Fig. 20(f)]. At the neutron spin resonance energy of $E = 15 \pm 1$ meV, spin excitations change from longitudinally elongated ellipses above T_c (not shown) to isotropic circles

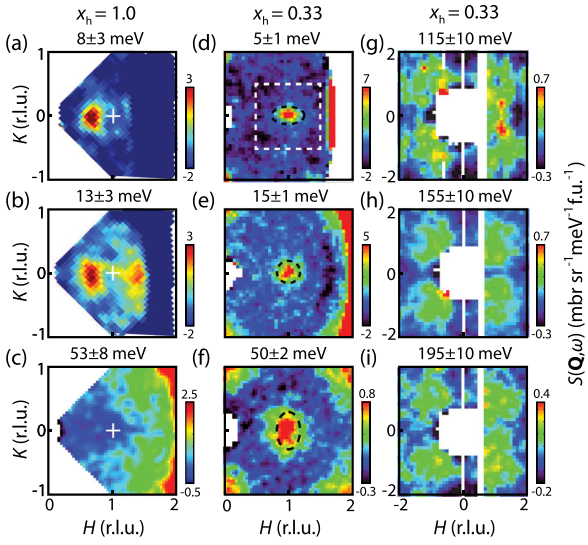

FIG. 20 (color online). Wave vector dependence of spin excitations in hole-doped $Ba_{1-x}K_xFe_2As_2$ from single crystal measurements. Two-dimensional images of spin excitations at different energies for hole-doped KFe_2As_2 at 5 K. (a) $E = 8 \pm 3$ meV obtained with $E_i = 20$ meV along the c axis. The right side incommensurate peak is obscured by background scattering. (b) 13 ± 3 meV with $E_i = 35$ meV, and (c) 53 ± 8 meV with $E_i = 80$ meV. For $Ba_{0.67}K_{0.33}Fe_2As_2$ at $T = 45$ K, images of spin excitations at (d) $E = 5 \pm 1$ meV obtained with $E_i = 20$ meV, (e) 15 ± 1 meV with $E_i = 35$ meV, and (f) 50 ± 2 meV obtained with $E_i = 80$ meV. Spin excitations in $Ba_{0.67}K_{0.33}Fe_2As_2$ at energy transfers (g) 115 ± 10 meV; (h) 155 ± 10 meV; (i) 195 ± 10 meV obtained with $E_i = 450$ meV, all at 9 K. Wave vector dependent backgrounds have been subtracted from the images. From M. Wang *et al.*, 2013.

below T_c in reciprocal space [Fig. 20(e)]. For energies above 100 meV, spin excitations in hole-doped $Ba_{0.67}K_{0.33}Fe_2As_2$ [Figs. 20(g)–20(i)] behave similarly to those of electron-doped $BaFe_{2-x}Ni_xAs_2$ (Fig. 19) (M. Wang *et al.*, 2013).

To quantitatively determine the electron- and hole-doping evolution of the spin excitations in iron pnictides, one can estimate the energy dependence of the local dynamic susceptibility per formula unit $\chi''(\omega)$ (Lester *et al.*, 2010; Liu *et al.*, 2012). The dashed boxes in Figs. 19 and 20 show the integration region of the local dynamic susceptibility in reciprocal space. At low energies, we integrate the scattering only within the white dashed box since it includes all magnetic responses in the Brillouin zone. Approaching the zone boundary, we integrate the response within the dashed boxes in Fig. 19 as discussed in Sec. II.A (Fig. 3). The energy dependence of the local dynamic susceptibility for hole- and electron-doped iron pnictides are plotted in Figs. 21(a) and 21(b), respectively. We see that the effect of hole doping near optimal superconductivity is to suppress high-energy spin excitations and transfer spectral weight to low energies. The intensity changes across T_c for hole-doped $Ba_{0.67}K_{0.33}Fe_2As_2$ are much larger than those of the electron-doped $BaFe_{1.9}Ni_{0.1}As_2$ (Liu *et al.*, 2012). As a function of increasing electron doping, the local dynamic susceptibility at low energies decreases and finally vanishes for electron-overdoped nonsuperconducting $BaFe_{1.7}Ni_{0.3}As_2$ (Luo, Lu *et al.*, 2013; M. Wang *et al.*, 2013).

D. Evolution of spin excitations in iron chalcogenides and alkali iron selenides

Compared with iron pnictides, iron chalcogenide ($Fe_{1+y}Te_{1-x}Se_x$) superconductors have a different static AF

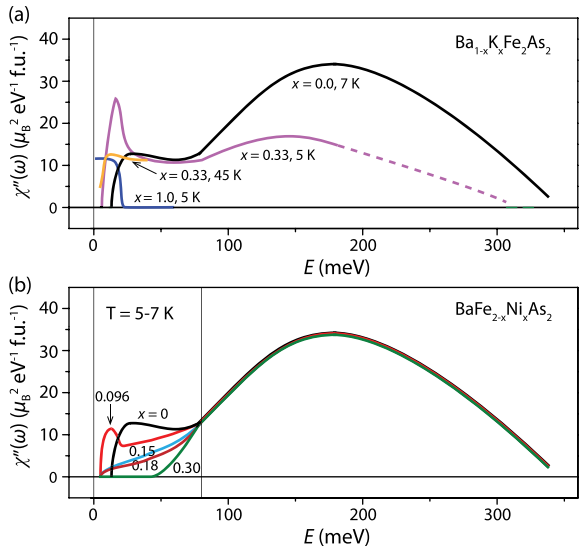

FIG. 21 (color online). Energy and temperature dependence of the local dynamic susceptibility $\chi''(\omega)$ for (a) $BaFe_2As_2$ (black solid line), $Ba_{0.67}K_{0.33}Fe_2As_2$ (solid lines for below and above T_c), KFe_2As_2 (solid line), and (b) $BaFe_{2-x}Ni_xAs_2$ with $x = 0, 0.096, 0.15, 0.18, 0.3$. The intensity is in absolute units of $\mu_B^2 eV^{-1} f u^{-1}$ obtained by integrating the $\chi''(Q, \omega)$ in the dashed regions specified in Figs. 18 and 19. From Liu *et al.*, 2012 and M. Wang *et al.*, 2013.

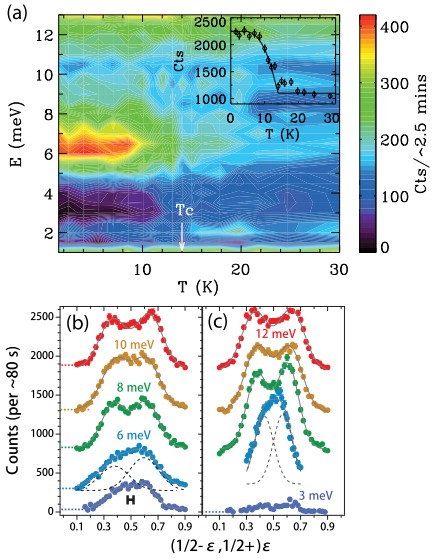

FIG. 22 (color online). Temperature and wave vector dependence of the resonance and low-energy spin excitations in iron chalcogenide superconductors. (a) Temperature dependence of the resonance energy for optimally doped $FeTe_{0.6}Se_{0.4}$. The mode energy is essentially temperature independent (Qiu *et al.*, 2009). The inset shows the temperature dependence of the resonance intensity. The wave vector dependence of the spin excitations at different energies along the transverse direction (b) above and (c) below T_c for $FeTe_{0.6}Se_{0.4}$. From Argyriou *et al.*, 2010.

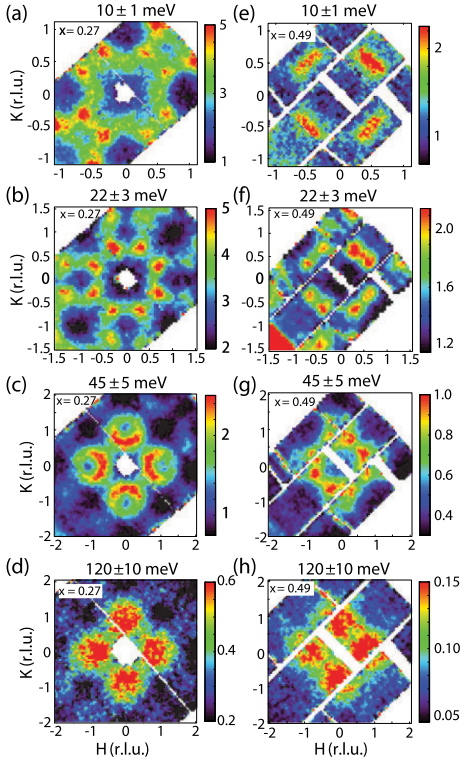

FIG. 23 (color online). Wave vector evolution of the spin excitations in $FeTe_{1-x}Se_x$ throughout the Brillouin zone. The in-plane wave vector dependence of the spin excitations in $FeTe_{0.73}Se_{0.27}$ at (a) $E = 10 \pm 1$, (b) 22 ± 3, (c) 45 ± 5, (d) 120 ± 10 meV. Identical scans for $FeTe_{0.51}Se_{0.49}$ at (e) $E = 10 \pm 1$, (f) 22 ± 3, (g) 45 ± 5, (h) 120 ± 10 meV. From Lumsden *et al.*, 2010.

ordered (bicollinear instead of collinear) parent compound (Fruchart *et al.*, 1975; Bao *et al.*, 2009; S. L. Li *et al.*, 2009), but a similar Fermi surface topology (Subedi *et al.*, 2008; F. Chen *et al.*, 2010; Nakayama *et al.*, 2010). If the resonance originates from the hole and electron Fermi surface nesting, one would also expect a resonance at a wave vector similar to that of the iron pnictides. The neutron scattering experiments on $FeTe_{0.6}Se_{0.4}$ reveal that this is indeed the case (Qiu *et al.*, 2009; Babkevich *et al.*, 2010; Mook *et al.*, 2010). Figure 22(a) shows that the resonance energy is weakly temperature dependent and suddenly vanishes above T_c (Qiu *et al.*, 2009; Harriger *et al.*, 2012). Another interesting aspect of $Fe_{1+y}Te_{1-x}Se_x$ is the presence of transverse incommensurate spin excitations at different energies [Figs. 22(b) and 22(c)] (Argyriou *et al.*, 2010; Lee *et al.*, 2010; Li *et al.*, 2010; Lumsden *et al.*, 2010). Since the parent compound of iron chalcogenide superconductors has bicollinear spin structure, the AF Bragg peaks and associated spin excitations in nonsuperconducting iron chalcogenides stem from wave vector positions rotated 45° from those of the resonance in reciprocal space. The enhancement of the resonance in superconducting $Fe_{1+y}Te_{1-x}Se_x$ occurs at the expense of the spin excitations associated with the AF nonsuperconducting parent compound (Liu *et al.*, 2010; Xu *et al.*, 2010; Chi *et al.*, 2011).

Figure 23 compares the wave vector dependence of spin excitations at different energies within the (H, K) plane for nonsuperconducting $Fe_{1+y}Te_{0.73}Se_{0.27}$ and superconducting $Fe_{1+y}Te_{0.51}Se_{0.49}$ (Lumsden *et al.*, 2010). Using the tetragonal crystalline lattice unit cell, the reciprocal lattice units in $Fe_{1+y}Te_{1-x}Se_x$ are rotated 45° from that for the AF ordered orthorhombic iron pnictides (Fig. 3). In this notation, spin waves from the bicollinear AF ordered $Fe_{1+y}Te$ stem from $\mathbf{Q}_{AF} = (\pm 0.5, 0)$ in reciprocal space while the resonance occurs at (0.5,0.5) (Lumsden *et al.*, 2010). For the nonsuperconducting $Fe_{1+y}Te_{0.73}Se_{0.27}$, spin excitations at low energies ($E = 10 \pm 1$, 22 ± 3 meV) peak at transversely incommensurate positions from (0.5,0.5) [Figs. 23(a) and 23(b)]. Increasing the energies to $E = 45 \pm 5$ [Fig. 23(c)] and 120 ± 10 meV [Fig. 23(d)], spin excitations become fourfold symmetric and move to positions near $(\pm 1, 0)$ and $(0, \pm 1)$ (Lumsden *et al.*, 2010). For superconducting $Fe_{1+y}Te_{0.51}Se_{0.49}$, the transverse incommensurate spin excitations in the nonsuperconducting sample at $E = 10 \pm 1$ and 22 ± 3 meV are replaced by the resonance and transversely elongated spin excitations near $(\pm 0.5, \pm 0.5)$ [Figs. 23(e) and 23(f)]. Spin excitations at $E = 45 \pm 5$ [Fig. 23(g)] and 120 ± 10 meV [Fig. 23(h)] are not greatly affected by superconductivity. These results are similar to spin excitations in electron-doped iron pnictides (Liu *et al.*, 2012), suggesting that superconductivity in iron chalcogenides affects only low-energy spin excitations and has commensurate spin excitations consistent with the hole and electron Fermi surface nesting (Liu *et al.*, 2010; Chi *et al.*, 2011).

In iron pnictide and iron chalcogenide superconductors, the neutron spin resonance is believed to arise from quasiparticle excitations between the hole and electron Fermi pockets near the Γ and M points, respectively (Mazin, 2010; Hirschfeld,

Korshunov, and Mazin, 2011). Since alkali iron selenide superconductors $A_xFe_{2-y}Se_2$ (Guo *et al.*, 2010; Fang *et al.*, 2011) do not have hole pockets near the Fermi energy (Mou *et al.*, 2011; Qian *et al.*, 2011; Y. Zhang *et al.*, 2011), it is important to determine if the system also has a resonance arising from quasiparticle excitations between the two electronlike Fermi pockets near the $(\pm 1, 0)$ and $(0, \pm 1)$ positions in reciprocal space (Maier *et al.*, 2011). From the earlier work on copper oxide superconductors, it is generally believed that the resonance arises from sign reversed quasiparticle excitations between two different parts of the Fermi surfaces (Eschrig, 2006). As there are no hole Fermi surfaces in superconducting $A_xFe_{2-y}Se_2$, a determination of the location of the resonance in reciprocal space will directly test the prediction from the RPA and weak-coupling calculation concerning the nature of the superconducting pairing interaction (Maier *et al.*, 2011). If a resonance is seen approximately at a wave vector connecting the two electron Fermi pockets, one would expect a sign change between the two Fermi pockets reminiscent of the *d*-wave pairing symmetry state of the copper oxide superconductors (Das and Balatsky, 2011; Maier *et al.*, 2011; F. Wang *et al.*, 2011).

Experimentally, a neutron spin resonance has been observed at an energy of $E_r = 14$ meV in the superconducting $Rb_2Fe_4Se_5$ with $T_c = 32$ K [Fig. 24(a)] (Park *et al.*, 2011). A complete mapping of the reciprocal space within the (H, K) scattering plane of the system reveals that the mode occurs near the wave vector (0.5,0.25,0.5) in the tetragonal unit cell notation (Friemel *et al.*, 2012). Figures 24(a) and 24(b) plot the temperature difference between 1.5 K ($< T_c$) and 35 K ($> T_c$) showing the superconductivity-induced resonance in energy and wave vector scans, respectively. Figure 24(c) shows the Fermi surfaces in the $(H, K, 0)$ plane corresponding to the doping level of 0.18 electron/Fe. The arrows are the in-plane nesting wave vectors consistent with the resonance (Friemel *et al.*, 2012). Figure 24(d) plots the difference of the RPA calculated dynamic susceptibility between the superconducting and normal states at the resonance energy (Friemel *et al.*, 2012). The calculated results are in qualitative agreement with the neutron scattering experiments, thus suggesting that the mode arises from quasiparticle excitations between the electron pockets (Friemel, Liu *et al.*, 2012; Friemel *et al.*, 2012). Subsequent neutron scattering experiments on superconducting $Rb_{0.82}Fe_{1.68}Se_2$ ($T_c = 32$ K) (M. Y. Wang *et al.*, 2012) and $Cs_xFe_{2y}Se_2$ (Taylor *et al.*, 2012) also found the resonance at wave vector positions connecting the two electron Fermi surfaces, thus confirming this is a general feature of the superconducting alkali iron selenides. Although the resonance mode energy in molecular-intercalated FeSe superconductors (Krzton-Maziopa *et al.*, 2012; Ying *et al.*, 2012; Burrard-Lucas *et al.*, 2013) approximately follows $\sim 5k_BT_c$ consistent with other iron-based superconductors (Inosov *et al.*, 2011), its wave vector is better matched to those of the superconducting component of $A_xFe_{2-y}Se_2$ (Taylor *et al.*, 2013).

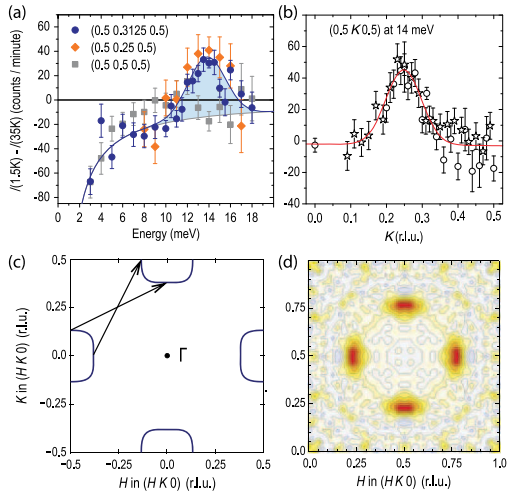

FIG. 24 (color online). Energy and wave vector dependence of the resonance in the superconducting alkali iron selenides. (a) Superconductivity-induced neutron scattering intensity changes in the superconducting $Rb_2Fe_4Se_5$ with $T_c = 32$ K. A resonancelike feature is seen below T_c at $E = 14$ meV. (b) The temperature differences in wave vector scans across the resonance along the $[0.5, K, 0.5]$ direction. (c) Possible nesting wave vectors connecting the two electronlike Fermi surfaces. (d) The temperature difference plot in the in-plane reciprocal space reveals the location of the resonance in the superconducting alkali iron selenides. From Park *et al.*, 2011, Friemel, Liu *et al.*, 2012, and Friemel *et al.*, 2012.

E. Impurity effect on spin excitations of iron pnictide and chalcogenide superconductors

As described earlier, low-energy spin excitations in high-T_c copper oxide and iron-based superconductors are coupled to superconductivity via the opening of a spin gap and redistributing the weight to a neutron spin resonance, both at the AF ordering wave vector of their parent compounds (Eschrig, 2006). Since superconductivity in high-T_c superconductors can be altered rather dramatically with impurity doping, it is important to determine the effect of impurities on spin excitations. In the case of the copper oxide superconductors, the resonance and low-energy spin excitations respond to magnetic and nonmagnetic impurity doping differently (Sidis *et al.*, 2000). When magnetic impurities such as Ni are doped into optimally superconducting $YBa_2Cu_2O_7$, the resonance peak shifts to lower energy with a preserved energy-to-T_c ratio (Sidis *et al.*, 2000). In contrast, nonmagnetic impurity Zn doping to $YBa_2Cu_2O_7$ restores normal state spin excitations but hardly changes the energy of the resonance (Sidis *et al.*, 2000). Similar Zn substitution in the underdoped $YBa_2Cu_2O_{6.6}$ induces static magnetic order at low temperatures and triggers a spectral-weight redistribution from the resonance to the low-energy incommensurate spin excitations (Suchaneck *et al.*, 2010).

To see the impurity effect on the resonance and low-energy spin excitations in iron-based superconductors, inelastic neutron scattering experiments were carried out on Ni- and Cu-doped superconducting $Fe_{1+y}Te_{0.5}Se_{0.5}$ (Xu *et al.*, 2012). Figure 25 shows temperature dependence of the spin excitations at different energies for $Fe_{1+y-0.04}Ni_{0.04}Te_{0.5}Se_{0.5}$ (Xu *et al.*, 2012). In addition to reducing the energy of the resonance, the spin excitations at $E = 3.5$ [Fig. 25(a)], 5 [Fig. 25(b)], and 6.5 meV [Fig. 25(c)] change from

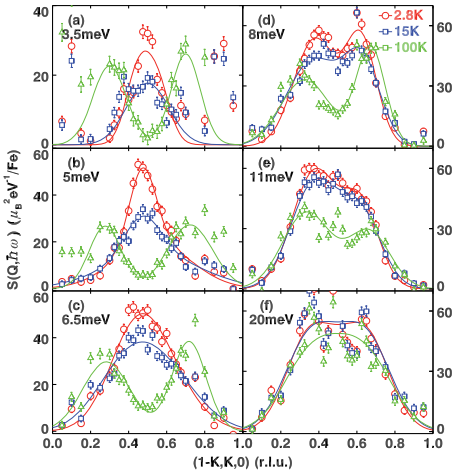

FIG. 25 (color online). Temperature dependence of the low-energy spin excitations in $Fe_{1+y-x}(Ni/Cu)_xTe_{0.5}Se_{0.5}$ family of iron chalcogenides. Wave vector dependence of the spin excitations along the transverse direction through the AF ordering wave vector $\mathbf{Q}_{AF}$ for the Ni-doped sample with $x = 0.04$ at $T = 2.8$ K (circles), 15 K (squares), and 100 K (triangles), obtained at (a) $E = 3.5$, (b) 5, (c) 6.5, (d) 8, (e) 11, and (f) 20 meV [which was measured in a higher zone, near $\mathbf{Q} = (1.5, 0.5, 0)$]. The low-energy spin excitations change from commensurate at low temperature ($T = 2, 15$ K) to transversely incommensurate at 100 K. Solid lines are guides to the eye. From Xu *et al.*, 2012.

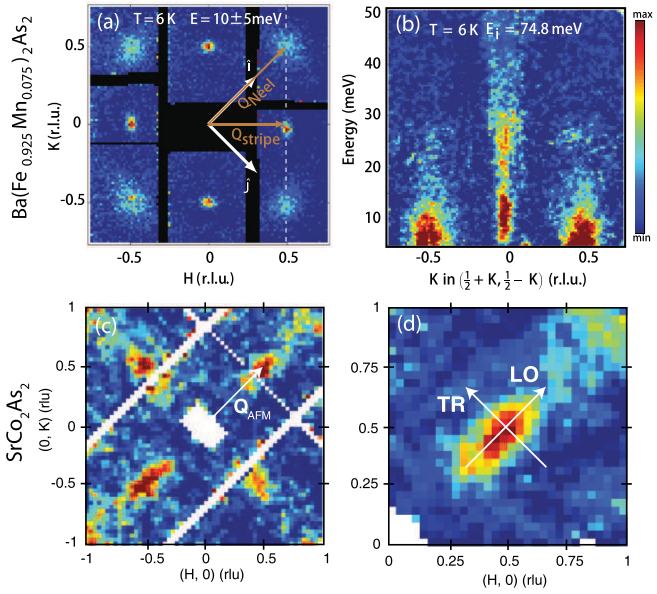

FIG. 26 (color online). Spin excitations in Mn impurity doped $BaFe_2As_2$ and $SrCo_2As_2$ pnictides. (a) Spin excitations in $Ba(Fe_{0.925}Mn_{0.075})_2As_2$ with incident beam ($E_i = 74.8$ meV) parallel to the crystallographic c axis. Data are displayed in the $(H + K, H - K)$ plane and averaged over an energy transfer of $E = 5 - 15$ meV. In addition to the usual spin excitations from the collinear AF ordered phase at $\mathbf{Q}_{stripe}$, there are spin excitations at $\mathbf{Q}_{Néel}$. (b) Spin excitations emanating from $\mathbf{Q}_{Néel}$ and $\mathbf{Q}_{stripe}$ after averaging over the range $H = 0.50 \pm 0.05$ (Tucker *et al.*, 2012b). (c) Wave vector dependence of the spin excitations in $SrCo_2As_2$ measured with incident beam along the c axis and $E_i = 75$ meV at $T = 5$ K. The energy integration range is between $E = 15$ and 25 meV, highlighting anisotropic spin excitations centered at $\mathbf{Q}_{AF}$. (d) The same data as in (c), but symmetry-equivalent quadrants have been averaged together. The wave vector anisotropy becomes even more apparent. From Jayasekara *et al.*, 2013.

commensurate below T_c to transversely incommensurate around 100 K. Wave vector scans at $E = 8$ [Fig. 25(d)], 11 [Fig. 25(e)], and 20 meV [Fig. 25(f)] have similar line shapes on warming from 2.8 to 100 K. Such a dramatic spectral reconstruction for temperatures up to $\sim 3T_c$ is not seen in copper oxide and iron pnictide superconductors and may indicate the presence of strong electron correlations in iron chalcogenide superconductors (Xu *et al.*, 2012). In subsequent transport and neutron scattering experiments on Cu-doped $Fe_{0.98-z}Cu_zTe_{0.5}Se_{0.5}$ with $z = 0, 0.02$, and 0.1 (Wen *et al.*, 2013), a metal-insulator transition was found for $z > 0.02$. In addition, low-energy spin excitations of the system are enhanced with increasing Cu doping. These results suggest that localization of the conducting states and electron correlations induced by the Cu doping may play an important role (Wen *et al.*, 2013).

While it is well known that hole doping via K substitution for Ba in $BaFe_2As_2$ induces high-T_c superconductivity (Rotter, Tegel, and Johrendt, 2008), substitution of Mn and Cr for Fe in $BaFe_2As_2$ never induces superconductivity (Sefat *et al.*, 2009; Thaler *et al.*, 2011). In the case of Cr doping, the system adopts a checkerboard G-type AF structure for $Ba(Fe_{1x}Cr_x)_2As_2$ with $x > 0.3$ [Fig. 6(a)] (Marty *et al.*, 2011). How spin excitations in the parent compound $BaFe_2As_2$ are modified by Cr doping is unclear. On the other hand, Mn-doped $BaFe_2As_2$ represents a more complicated situation: while $BaMn_2As_2$ forms a simple AF structure with the ordered moment along the c axis (Singh *et al.*, 2009), Mn doping of $BaFe_2As_2$ may induce a Griffiths regime associated with the suppression of the collinear AF order in $BaFe_2As_2$ by the randomly introduced localized Mn moments acting as strong magnetic impurities (Inosov *et al.*, 2013). Inelastic neutron scattering experiments were carried out on single crystals of $Ba(Fe_{1-x}Mn_x)_2As_2$ with $x = 0.075$, which has a tetragonal-to-orthorhombic lattice distortion and orders into a collinear AF structure simultaneously below $T_s = T_N = 80$ K (Tucker *et al.*, 2012b). Figure 26(a) shows spin excitations of the system measured with the crystallographic c axis parallel to the incident neutron beam at $E_i = 74.8$ meV. In addition to spin excitations associated with the collinear AF structure denoted as $\mathbf{Q}_{stripe} = \mathbf{Q}_{AF}$, there are excitations at the AF wave vector positions of $BaMn_2As_2$ ($\mathbf{Q}_{Néel}$) (Tucker *et al.*, 2012b). At present, it is unclear if this is an intrinsic effect of the system or if there is real space phase separation between Mn and Fe. Figure 26(b) shows energy dependence of the scattering at $\mathbf{Q}_{stripe}$ and $\mathbf{Q}_{Néel}$. While spin excitations at $\mathbf{Q}_{stripe}$ extend well above 50 meV, they are limited to below ~ 30 meV at $\mathbf{Q}_{Néel}$ [Fig. 26(b)].

In the study of electron-doping evolution of the spin excitations in iron pnictides, it was found that electron doping via Co or Ni substitution for Fe in $BaFe_2As_2$ induces transversely elongated spin excitations near $\mathbf{Q}_{stripe}$ due to the mismatched hole and electron Fermi surfaces (Figs. 15 and 16) (Zhang, Sknepnek, and Schmalian, 2010). If this scenario

is correct for all electron-doping levels, one would expect transversely elongated spin excitations in heavily Co-doped $BaFe_2As_2$ or $SrFe_2As_2$. Figures 26(c) and 26(d) show the wave vector dependence of spin excitations in $SrCo_2As_2$ (Jayasekara *et al.*, 2013). Although spin excitations still appear at the same wave vector positions as those of $BaFe_2As_2$, they are longitudinally elongated. As $SrCo_2As_2$ may have complicated Fermi surfaces like that of $BaCo_2As_2$ (N. Xu *et al.*, 2013), Fermi surface nesting could potentially explain the line shape of the spin excitations. It will be interesting to sort out how spin excitations evolve from transversely elongated to longitudinally elongated in reciprocal space as a function of Co doping for $BaFe_{2-x}Co_xAs_2$ and $SrFe_{2-x}Co_xAs_2$.

Another iron pnictide worthy of mention is LiFeAs (Pitcher *et al.*, 2008; Tapp *et al.*, 2008; Wang *et al.*, 2008). Although this material has the same crystal structure as that of NaFeAs [Fig. 1(d)], it is a superconductor without static AF order in stoichiometric LiFeAs and Li deficiency tends to suppress superconductivity. Initial inelastic neutron scattering measurements on powder samples indicate the presence of superconductivity-induced resonance near the usual AF ordering wave vector $\mathbf{Q}_{AF}$ (Taylor *et al.*, 2011). Subsequent neutron scattering experiments on single crystals showed that spin excitations in this system are transversely incommensurate away from the $\mathbf{Q}_{AF}$ for both the superconducting LiFeAs [Fig. 27(a)] (Qureshi *et al.*, 2012) and nonsuperconducting $Li_{1-x}FeAs$ [Fig. 27(b)] (M. Wang *et al.*, 2012). The absence of the static AF order has been interpreted as due to poor Fermi surface nesting between Γ and M consistent with ARPES measurements [Fig. 27(c)] (Borisenko *et al.*, 2010; Brydon *et al.*, 2011). However, the quasiparticle scattering between the hole pockets near Γ and electron pocket M should give rise to transverse incommensurate spin fluctuations and this is indeed the case [Fig. 27(a)] (Qureshi *et al.*, 2012; M. Wang *et al.*, 2012; Qureshi, Steffens *et al.*, 2014). Furthermore, the incommensurate spin excitations are weakly energy dependent and only broaden slightly for nonsuperconducting $Li_{1-x}FeAs$ [Fig. 27(d)] (M. Wang *et al.*, 2012). These results suggest that spin excitations in LiFeAs have the same origin as other iron pnictides, and the low-energy spin excitations in the system follow the nested Fermi surface scenario.

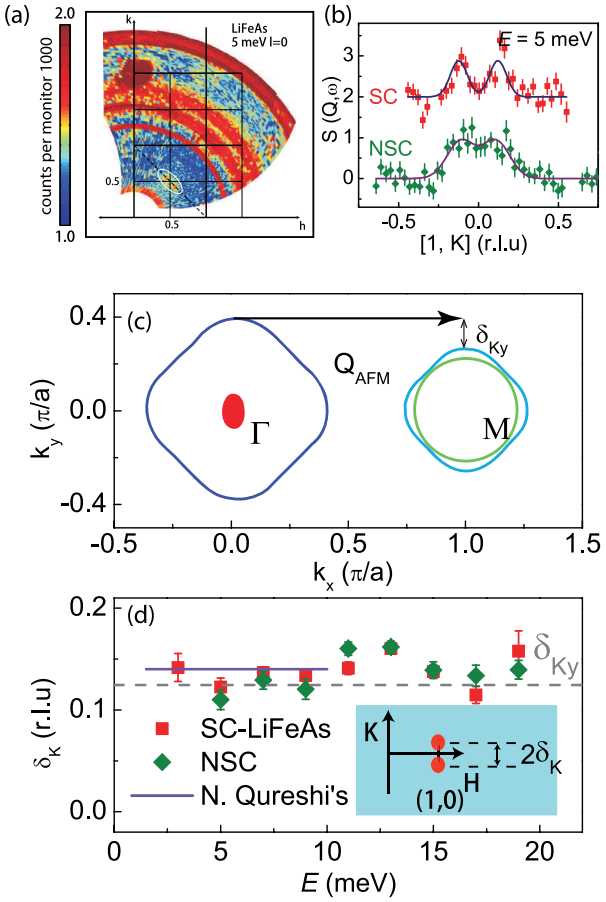

FIG. 27 (color online). Spin excitations in superconducting and nonsuperconducting LiFeAs without static AF order. (a) Mapping of inelastic neutron scattering intensity at $E = 5$ meV in the (H, K) reciprocal space of LiFeAs in the tetragonal notation. Note the transverse incommensurate peaks away from the $\mathbf{Q}_{AF} = (0.5, 0.5)$ position (Qureshi *et al.*, 2012). (b) Comparison of incommensurate spin excitations for the superconducting (SC) and nonsuperconducting (NSC) LiFeAs at $E = 5$ meV (M. Wang *et al.*, 2012). (c) Hole and electron Fermi surfaces in LiFeAs from ARPES (Borisenko *et al.*, 2010). The arrow indicates a possible nesting condition between hole and electron Fermi surfaces. The δ_{Ky} indicates the expected transverse incommensurability. (d) The experimentally observed transverse incommensurate spin fluctuations and its energy dependence for SC and NSC LiFeAs (Qureshi *et al.*, 2012; M. Wang *et al.*, 2012; Qureshi, Steffens *et al.*, 2014). The δ_K is the observed transverse incommensurability.

F. Neutron polarization analysis of spin-excitation anisotropy in iron pnictides

Although most neutron scattering experiments are carried out with unpolarized neutrons, neutron polarization analysis can provide some unique information concerning the nature of the ordered moment and the anisotropy of spin excitations. The neutron polarization analysis was first developed at Oak Ridge National Laboratory in the pioneering work of Moon, Riste, and Koehler (1969). This technique was used to unambiguously identify the magnetic nature of the neutron spin resonance in optimally doped high-T_c copper oxide $YBa_2Cu_3O_7$ (Mook *et al.*, 1993). In modern polarized neutron scattering experiments on high-T_c superconductors at the Institut Laue-Langevin, the Cryopad capability (Leliévre-Berna *et al.*, 2005) is typically used to ensure that the sample is in a strictly zero magnetic field environment, thus avoiding errors due to flux inclusion and field expulsion in the superconducting phase of the sample. The Cryopad device can also be used for spherical neutron polarimetry in which an arbitrary incident and scattered neutron beam polarization can be measured (Leliévre-Berna *et al.*, 2005).

Polarized neutrons were produced using a focusing Heusler monochromator and analyzed using a focusing Heusler analyzer. Polarization analysis can be used to separate magnetic (e.g., spin excitations) and nuclear (e.g., phonon) scattering because the former has a tendency to flip the spin of the neutron, whereas the latter leaves the neutron spin unchanged. More specifically, the spin of the neutron is

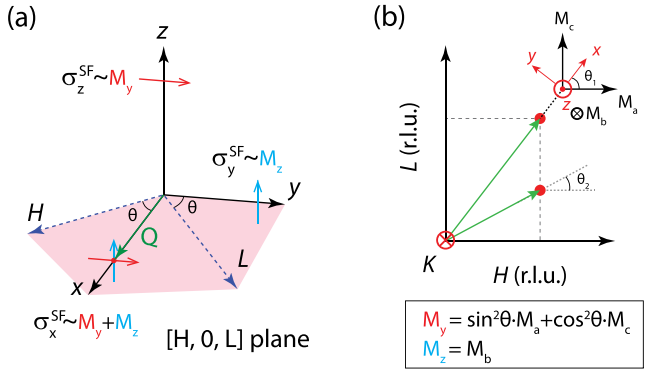

FIG. 28 (color online). Neutron polarization analysis used to determine the magnitude of spin excitations along the crystallographic a (M_a), b (M_b), and c (M_c) axis directions. (a) Incident beam neutrons are polarized along the x, y, and z directions, corresponding to directions along the momentum transfer $\mathbf{Q}$, perpendicular to $\mathbf{Q}$ but in the horizontal scattering plane, and perpendicular to $\mathbf{Q}$ and the horizontal scattering plane, respectively. In this geometry, neutron spin-flip scattering $\sigma_x^{SF} \sim M_y + M_z$, where M_y and M_z are magnitudes of spin excitations along the y and z directions, respectively. Similarly, $\sigma_y^{SF} \sim M_z$ and $\sigma_z^{SF} \sim M_y$. If the angle between the x direction and the H axis is θ, we have $M_y = \sin^2\theta M_a + \cos^2\theta M_c$ and $M_z = M_b$. (b) Since M_a, M_b, and M_c should be the same at equivalent wave vectors in reciprocal space except for the magnetic form factor, we can conclusively determine M_a, M_b, and M_c by measuring σ_α^{SF} at two or more equivalent reciprocal lattice vectors. From Luo, Wang *et al.*, 2013.

always flipped in a magnetic interaction where the neutron polarization is parallel to the wave vector transfer $\mathbf{Q}$ and the magnetic moment or excitation polarization in the sample is transverse to $\mathbf{Q}$. We therefore describe the neutron polarization in a coordinate system where x is parallel to $\mathbf{Q}$. For convenience, we then define the other orthogonal directions with y in the scattering plane and z out of plane [see Fig. 28(a)]. There are then six independent channels in which the instrument can be configured at a specific wave vector and energy point: three neutron polarization directions x, y, and z, each of which can be measured to detect neutrons that flip or do not flip their spins when scattering at the sample. The measured neutron cross sections are labeled by the experimental configuration in which they were measured and are written σ_α^{SF}, σ_α^{NSF}, where α is the neutron polarization direction (x, y or z) and the superscript represents either spin-flip (SF) or non-spin-flip (NSF) scattering.

Magnetic neutron scattering probes only the magnetic moment perpendicular to $\mathbf{Q}$. The cross sections can therefore be written in terms of M_y and M_z [see Fig. 28(a)], the two spatial components (perpendicular to $\mathbf{Q}$) of the spin direction of the magnetic excitations, and the nuclear scattering strength N. However, a measured cross-section component on an imperfect instrument contains a leakage between SF and NSF channels due to imperfect neutron polarization. This leakage can be quantified by measuring the nuclear Bragg peak contamination into the spin-flip channel, the "instrumental flipping ratio" $R = \mathrm{NSF}_N/\mathrm{SF}_N$ (for an unpolarized neutron scattering experiment $R = 1$, and $R \to \infty$ in an ideal polarized neutron scattering experiment). The measured cross-section components can then be written (Moon, Riste, and Koehler, 1969; Lipscombe *et al.*, 2010)

$$\begin{pmatrix} \sigma_x^{SF} \\ \sigma_y^{SF} \\ \sigma_z^{SF} \\ \sigma_x^{NSF} \\ \sigma_y^{NSF} \\ \sigma_z^{NSF} \end{pmatrix} = \frac{1}{(R+1)} \begin{pmatrix} R & R & 1 & 2R/3+1/3 & (R+1) \\ 1 & R & 1 & 2R/3+1/3 & (R+1) \\ R & 1 & 1 & 2R/3+1/3 & (R+1) \\ 1 & 1 & R & R/3+2/3 & (R+1) \\ R & 1 & R & R/3+2/3 & (R+1) \\ 1 & R & R & R/3+2/3 & (R+1) \end{pmatrix} \begin{pmatrix} M_y \\ M_z \\ N \\ \mathrm{NSI} \\ B \end{pmatrix}, \tag{1}$$

where B is a background term to take account of instrumental background and the nonmagnetic nuclear incoherent scattering from the sample, which is assumed to be equal in all six cross sections when measured at the same wave vector and energy. NSI is the nuclear spin incoherent scattering caused by moments within the nuclei of the isotopes in the sample. NSI is independent of $\mathbf{Q}$ and typically is negligible in magnitude compared with the nuclear coherent cross section N. Furthermore, in the case where only SF (or only NSF) cross-section components are collected, NSI would be absorbed into the B term.

For SF neutron scattering measurements at $\mathbf{Q}$, one can conclusively determine the magnetic components M_y and M_z. If the magnetic components of the system along the x, y, and z are M_x, M_y, and M_z, respectively, we have $M_y = M_b$ and $M_z = M_a \sin^2\theta + M_c \cos^2\theta$ if the sample is aligned in the $[H, 0, L]$ scattering plane, where M_a, M_b, and M_c are magnitudes of spin excitations along the orthorhombic a-, b-, and c-axis directions of the lattice, respectively, and θ is the angle between M_a and x axis [Fig. 28(b)] (Lipscombe *et al.*, 2010). Since there are three unknowns (M_a, M_b, M_c) and only two equations with known M_y and M_z, one can determine only the values of M_a, M_b, and M_c by measuring at least two equivalent reciprocal lattice vectors with different θ angle as illustrated in Fig. 28(b). In the initial polarized neutron scattering experiments on optimally electron-doped superconducting $BaFe_{1.9}Ni_{0.1}As_2$, spin-excitation anisotropy near the resonance energy was observed (Lipscombe *et al.*, 2010). Similar results were also found for the resonance in optimal superconducting Fe(Se,Te) (Babkevich *et al.*, 2011). For electron-overdoped $BaFe_{1.85}Ni_{0.15}As_2$, the resonance and spin excitations at all energies probed are isotropic with $M_y = M_z$ (Liu, Lester *et al.*, 2012).

Figure 29 summarizes the outcome from polarized neutron scattering experiments on $BaFe_2As_2$. From unpolarized neutron scattering experiments, it is well known that spin waves in the AF ordered state are gapped below about ~15 meV at the magnetic Brillouin-zone center $\mathbf{Q}_{AF}$ (Matan *et al.*, 2009; Park *et al.*, 2012). Figures 29(a)–29(d) show neutron SF inelastic constant-$\mathbf{Q}$ scans at the zone center $(1, 0, L)$ for different L values and at (1,0,0). The dots represent the magnitude of magnetic scattering along the y axis direction, or M_y, while the squares depict M_z, where $\sigma_{y,z} = (R+1)[\sigma_x^{SF} - \sigma_{y,z}^{SF}]/(R-1) \approx M_{y,z}$ (Qureshi, Steffens *et al.*, 2012). Consistent with unpolarized measurements (Matan *et al.*, 2009; Park *et al.*, 2012), there are large spin gaps at (1,0,0) and (1,0,1).

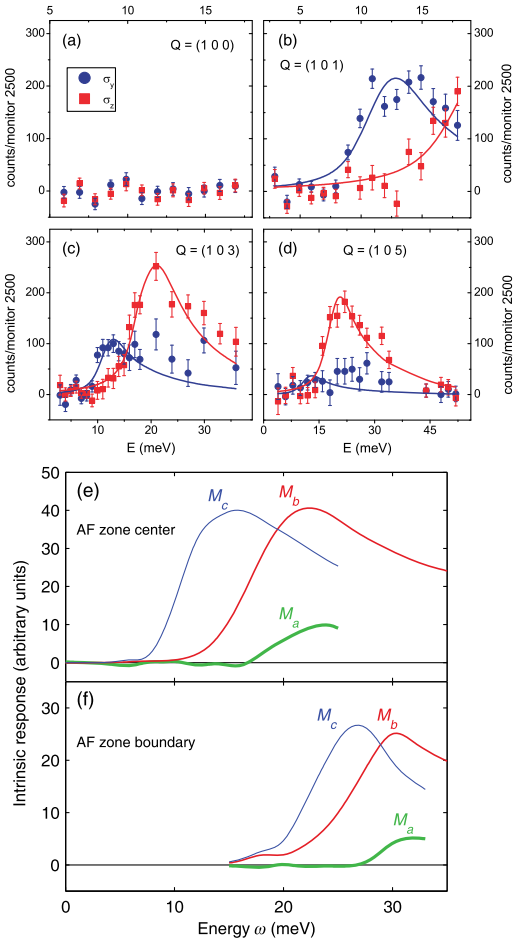

FIG. 29 (color online). Polarized neutron scattering study of spin waves in $BaFe_2As_2$. The AF ordering Brillouin-zone centers are at $\mathbf{Q}_{AF} = (1, 0, L)$ with $L = 1, 3, \ldots$. The magnetic zone boundaries are at $\mathbf{Q} = (1, 0, L)$ with $L = 0, 2, \ldots$. (a) Inelastic constant-$\mathbf{Q}$ scans at the AF zone boundary $\mathbf{Q} = (1, 0, 0)$. Here the dots are the magnetic scattering along the y direction, or $\sigma_y \sim \sigma_x^{SF} - \sigma_y^{SF} \sim M_y$, while the squares depict $\sigma_z \sim \sigma_x^{SF} - \sigma_z^{SF} \sim M_z$. (b)–(d) Similar scans at $\mathbf{Q}_{AF} = (1, 0, L)$ with $L = 1, 3$, and 5, respectively. The solid lines are spline-interpolated spin-wave theory calculations folded with the experimental resolution (Qureshi, Steffens *et al.*, 2012). Using an identical experimental setup as that of Qureshi, Steffens *et al.* (2012) but with much more sample mass, the energy dependence of M_a, M_b, and M_c is determined at the (e) magnetic Brillouin-zone center and (f) zone boundary. The presence of longitudinal spin excitations, or nonzero M_a, is seen above 20 meV at $\mathbf{Q}_{AF} = (1, 0, 1)$ and above 30 meV at $\mathbf{Q} = (1, 0, 0)$ (C. Wang *et al.*, 2013).

However, the gap value for σ_z^{SF} is significantly larger than that for σ_y^{SF} [Figs. 29(b)–29(d)]. These results indicate strong single-iron anisotropy within the layer, suggesting that it costs more energy to rotate a spin within the orthorhombic a-b plane than to rotate it perpendicular to the FeAs layers (Qureshi, Steffens *et al.*, 2012). In addition, there is no evidence for longitudinal spin fluctuations typically associated with itinerant electrons and nested Fermi surfaces like in the spin-density-wave state of pure chromium metal (Fawcett *et al.*, 1994; Qureshi, Steffens *et al.*, 2012).

In subsequent polarized neutron scattering experiments on $BaFe_2As_2$ with greater sample mass (C. Wang *et al.*, 2013), three distinct spin-excitation components, M_a, M_b, and M_c, with magnetic moments fluctuating along the three crystallographic axes are identified at the AF Brillouin-zone center [Fig. 29(e)] and zone boundary [Fig. 29(f)]. The data reveal the presence of finite M_a at the AF zone center for energies above ~20 meV [Fig. 29(e)]. Similar measurements at the AF zone boundary suggest nonzero values of M_a above ~30 meV [Fig. 28(f)]. While M_b and M_c, the two transverse components of spin waves, can be described by a linear spin-wave theory with magnetic anisotropy and interlayer coupling, the presence of M_a, the longitudinal component of spin waves, is generically incompatible with transverse spin waves at low $\mathbf{Q}$ from a local-moment Heisenberg Hamiltonian. These results suggest a contribution of itinerant electrons to the magnetism that is already in the parent compound of this family of Fe-based superconductors. This means that one cannot account for spin waves in the parents of iron pnictides with a purely local-moment picture and must take the contribution from itinerant electrons into account to understand the magnetism in these materials (C. Wang *et al.*, 2013).

In a polarized inelastic neutron scattering experiment on optimal electron-doped $BaFe_{1.88}Co_{0.12}As_2$ ($T_c = 24$ K), two resonance-like excitations were found in the superconducting state (Steffens *et al.*, 2013). While the high-energy mode occurring at $E = 8$ meV is an isotropic resonance with weak dispersion along the c axis, there is a 4 meV spin excitation that appears only in the c axis polarized channel and whose intensity modulates along the c axis similar to spin waves in the undoped $BaFe_2As_2$ [Figs. 30(a) and 30(b)]. These results suggest that spin excitations in undoped and optimal electron-doped $BaFe_2As_2$ have similar features, different from what one might expect for superconducting and AF phases of iron pnictides (Steffens *et al.*, 2013).

In a separate polarized inelastic neutron scattering experiment on electron underdoped $BaFe_{1.904}Ni_{0.096}As_2$, where the system exhibits an AF order and tetragonal-to-orthorhombic lattice distortion temperatures near $T_N \approx T_s = 33 \pm 2$ K, and superconductivity below $T_c = 19.8$ K, neutron SF cross sections have been measured at various energies and wave vectors. Figures 30(c) and 30(d) show the energy dependence of M_y and M_z in the normal and superconducting states at the AF wave vector (Luo, Wang *et al.*, 2013). In addition to confirming that the low-energy spin excitations are highly anisotropic below ~5 meV in the superconducting state [Fig. 30(d)], the magnetic scattering appears to be anisotropic in the normal state with $M_z > M_y$ [Fig. 30(c)]. Figure 30(e) shows that the magnitudes of M_y and M_z become different below T^*, illustrating the fact that the magnetic anisotropy first appears below the temperature where transport measurements on uniaxial strain detwinned samples display in-plane resistivity anisotropy (Chu *et al.*, 2010; Tanatar *et al.*, 2010; Fisher, Degiorgi, and Shen, 2011). To quantitatively determine if the spin-excitation anisotropy is indeed within the a-b plane, neutron SF cross sections were measured at multiple equivalent wave vectors. The outcome suggests that the presence of in-plane spin-excitation anisotropy is associated with resistivity anisotropy in a strain-induced sample [Fig. 30(f)]. Therefore, spin-excitation anisotropy in iron

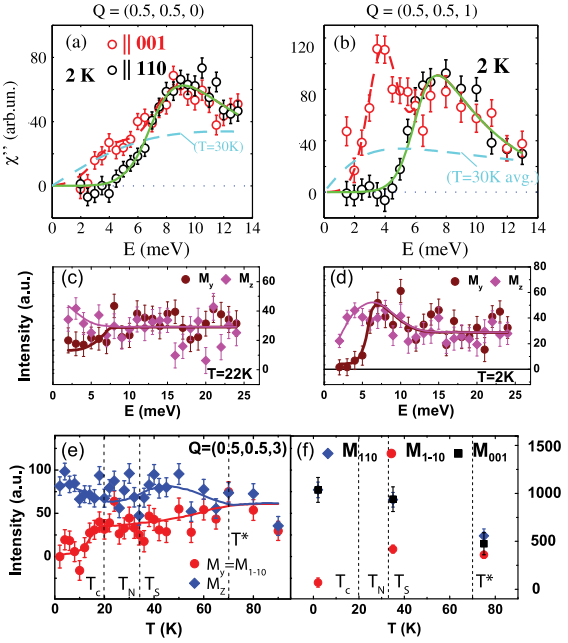

FIG. 30 (color online). Neutron polarization analysis of the spin-excitation anisotropy in electron-doped iron pnictide superconductors. (a) Energy dependence of the imaginary part of the out-of-plane (M_c) and in-plane (M_b) generalized magnetic susceptibilities at $\mathbf{Q} = (0.5, 0.5, 0)$ in tetragonal notation for $Ba(Fe_{0.94}Co_{0.06})_2As_2$ at $T = 2$ K. The dashed line shows isotropic paramagnetic scattering at $T = 30$ K. (b) Similar data at $\mathbf{Q}_{AF} = (0.5, 0.5, 1)$, where the mostly c axis polarized susceptibility exhibits a peak in the superconducting phase. From Steffens *et al.*, 2013. (c) Energy dependence of M_y and M_z in the normal state at $\mathbf{Q}_{AF} = (0.5, 0.5, 3)$ for $BaFe_{1.904}Ni_{0.096}As_2$ ($T_c = 19.8$ K, $T_N \approx T_s = 33 \pm 2$ K). (d) Similar data at $T = 2$ K. The data show clear low-energy spin-excitation anisotropy in both the normal and superconducting states. (e) Temperature dependence of M_y and M_z, where T^* marks the temperature of the in-plane resistivity anisotropy. (f) Temperature dependence of $M_a = M_{110}$, $M_b = M_{1-10}$, and $M_c = M_{001}$. Vertical dashed lines mark temperatures for T^*, T_s, T_N, and T_c. From Luo, Wang *et al.*, 2013.

pnictides is a direct probe of the spin-orbit coupling in these materials (Luo, Wang *et al.*, 2013). Recent polarized inelastic neutron scattering experiments on superconducting $Ba_{0.67}K_{0.33}Fe_2As_2$ (C. L. Zhang, Liu *et al.*, 2013) and $Ba_{0.5}K_{0.5}Fe_2As_2$ (Qureshi, Lee *et al.*, 2014) reveal that the low-energy spin-excitation anisotropy persists to hole-overdoped iron pnictides far away from the AF ordered phase. Similar polarized neutron scattering experiments on underdoped $NaFe_{0.985}Co_{0.015}As$ with double resonances [Fig. 17(c)] suggest that the first resonance is highly anisotropic and polarized along the a and c axes, while the second mode is isotropic similar to that of electron-overdoped $NaFe_{0.935}Co_{0.045}As$. Since the a-axis polarized spin excitations of the first resonance appear below T_c, the itinerant electrons contributing to the magnetism may also be coupled to the superconductivity (Zhang *et al.*, 2014b).

Polarized neutron scattering is not only useful for determining the spin-excitation anisotropy, it can also be used to measure the susceptibility and induced magnetization in the normal and superconducting states of a superconductor. The technique of using polarized neutron diffraction to study the magnetization of the paramagnetic crystal by an externally applied magnetic field was developed by Shull and Wedgewood (1966) in their study of electron-spin pairing of a BCS superconductor V_3Si. Instead of the full neutron polarization analysis as described earlier, the magnetization measurements are performed under a magnetic field using a polarized incident beam of neutrons (Brown *et al.*, 2010; Lester *et al.*, 2011). The flipping ratio R, defined as the ratio of the neutron scattering cross sections with neutrons parallel and antiparallel to the applied magnetic field, is associated with the nuclear structure factors $F_N(\mathbf{G})$ and the Fourier transform of the real-space magnetization density $\mathbf{M}(\mathbf{G})$ via $R \approx 1 - 2\gamma r_0 M(\mathbf{G})/\mu_B F_N(\mathbf{G})$, where $\gamma r_0 = 5.36 \times 10^{-15}$ m and $\mathbf{G}$ is the reciprocal lattice vector (Lester *et al.*, 2011). In a conventional BCS superconductor such as V_3Si, where electrons below T_c form singlet Cooper pairs, the temperature dependence of the field-induced magnetization shows the characteristic Yosida drop below T_c expected for singlet pairing [Fig. 31(a)] (Shull and Wedgewood, 1966). For a spin-triplet superconductor such as Sr_2RuO_4 (Mackenzie and Maeno, 2003), there is no change in the field-induced magnetization across T_c (Duffy *et al.*, 2000). Temperature dependence of the field-induced magnetization shows a clear drop below T_c in nearly optimally electron-doped $BaFe_{1.87}Co_{0.13}As_2$ [Fig. 31(b)] (Lester *et al.*, 2011), consistent with measurements of the NMR Knight shift in the same compound (Ning *et al.*, 2008; Oh *et al.*, 2011). The large

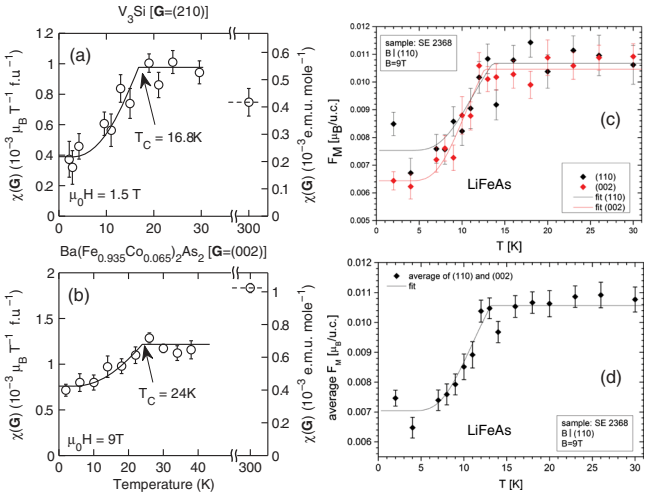

FIG. 31 (color online). Polarized neutron diffraction studies of the induced magnetization density for different iron pnictide superconductors. The temperature dependence of the susceptibility and induced moment for (a) the conventional BCS superconductor V_3Si, and (b) iron pnictide superconductor $Ba(Fe_{0.935}Co_{0.065})_2As_2$. The solid lines are the Yosida behavior expected for a singlet order parameter. From Lester *et al.*, 2011. (c) The temperature dependence of the field-induced magnetization for superconducting LiFeAs obtained using the (1,1,0) and (0,0,2) nuclear Bragg peaks under a 9-T magnetic field. (d) The average of the (1,1,0) and (0,0,2) shows a clear drop below T_c, suggesting spin singlet pairing for LiFeAs. From Brand *et al.*, 2014.

residual contribution of the field-induced magnetization below T_c seen in both V_3Si (Shull and Wedgewood, 1966) and $BaFe_{1.87}Co_{0.13}As_2$ (Lester *et al.*, 2011) has been attributed to the van Vleck or orbital contribution to the susceptibility.

Similar polarized neutron diffraction experiments have also been carried out on superconducting LiFeAs (Brand *et al.*, 2014), which does not have a static AF ordered parent compound (Pitcher *et al.*, 2008; Tapp *et al.*, 2008; Wang *et al.*, 2008) and may have triplet electron pairing due to a large density of states near the Fermi level favoring a ferromagnetic instability (Brydon *et al.*, 2011). Figure 31(c) shows temperature dependence of the field-induced magnetization at wave vectors (1,1,0) and (0,0,2). The average of the (1,1,0) and (0,0,2) is shown in Fig. 31(d). Different from the spin-triplet superconductor Sr_2RuO_4 (Duffy *et al.*, 2000), the field-induced magnetization clearly decreases at the onset of T_c, consistent with the spin singlet electron pairing (Brand *et al.*, 2014). Therefore, the mechanism of superconductivity in LiFeAs is likely the same as all other iron-based superconductors.

G. Electronic nematic phase and neutron scattering experiments under uniaxial strain

As mentioned in Sec. III.F, transport measurements on uniaxial strain detwinned electron-doped $BaFe_2As_2$ reveal clear evidence for in-plane resistivity anisotropy first occurring at a temperature above the zero pressures T_N and T_s (Chu *et al.*, 2010; Tanatar *et al.*, 2010; Fisher, Degiorgi, and Shen, 2011). As a function of increasing electron doping, the resistivity anisotropy first increases and then vanishes near optimal superconductivity (Fisher, Degiorgi, and Shen, 2011), consistent with a signature of the spin nematic phase that breaks the in-plane fourfold rotational symmetry (C_4) of the underlying tetragonal lattice (Fang *et al.*, 2008; Dai *et al.*, 2009; Fernandes, Chubukov, and Schmalian, 2014). NMR experiments on the 1111 family of materials also indicate the presence of a nematic phase below T_s (Fu *et al.*, 2012). However, recent scanning tunneling microscopy (Allan *et al.*, 2013) and transport measurements (Ishida *et al.*, 2013) suggest that the resistivity anisotropy in Co-doped $BaFe_2As_2$ arises from Co-impurity scattering and is not an intrinsic property of these materials. On the other hand, ARPES measurements on Co-doped $BaFe_2As_2$ (Yi *et al.*, 2011) and NaFeAs (Y. Zhang *et al.*, 2012) reveal a splitting in energy between two orthogonal bands with dominant d_{xz} and d_{yz} character at the temperature of resistivity anisotropy in uniaxial strain detwinned samples, thereby suggesting that orbital ordering is also important for the electronic properties of iron pnictides (Krüger *et al.*, 2009; Lee, Yin, and Ku, 2009; Lv, Wu, and Phillips, 2009). Finally, since transport measurements were carried out on uniaxial strain detwinned samples (Fisher, Degiorgi, and Shen, 2011), it is unclear if the uniaxial strain can modify the structural and magnetic phase transitions in these materials.

The first neutron scattering experiment carried out under uniaxial strain was on as-grown $BaFe_2As_2$ (Dhital *et al.*, 2012). The data show that modest strain fields along the in-plane orthorhombic b_o axis as shown in Fig. 32(a) can induce significant changes in the structural and magnetic phase

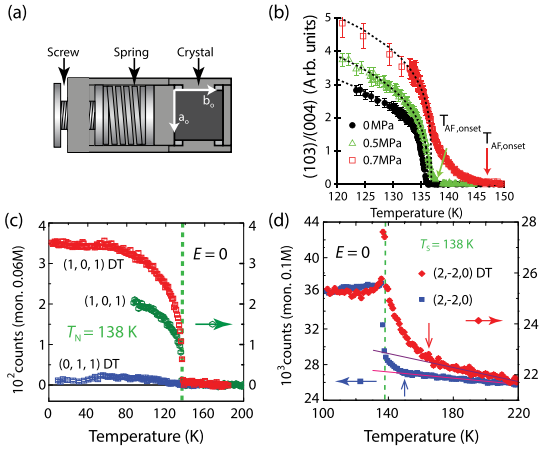

FIG. 32 (color online). The effect of uniaxial strain on structural and magnetic phase transitions in the as-grown and annealed $BaFe_2As_2$. (a) Schematic of the device used to apply uniaxial strain to detwin single crystals of $BaFe_2As_2$. The sample is cut into a square shape with a_o/b_o parallel to the applied pressure direction. (b) Temperature dependence of the magnetic order parameters under different applied unaixial strain for the as-grown $BaFe_2As_2$. The onset of the AF ordering temperature increases with increasing uniaxial pressure. From Dhital *et al.*, 2012. (c) Magnetic Bragg peak intensity at the (1,0,1) and (0,1,1) positions for the annealed $BaFe_2As_2$ at zero pressure and $P \sim 15$ MPa uniaxial pressure along the b_o axis. No large shift in T_N is seen under uniaxial pressure. (d) The squares show the temperature dependence of the $(2,-2,0)$ nuclear Bragg peak at zero pressure. The sharp step at T_s is caused by releasing of the neutron extinction due to tetragonal-to-orthorhombic lattice distortion. The identical scan under $P \sim 15$ MPa uniaxial pressure is shown as diamonds. From Lu, Park *et al.*, 2014.

behavior simultaneous with the removal of structural twinning effects. Both the structural lattice distortion and long-range spin ordering occur at temperatures far exceeding the strain free phase transition temperatures [Fig. 32(b)], thus suggesting that the resistivity anisotropy in transport measurements is a consequence of the shift in T_N and T_s under uniaxial strain (Dhital *et al.*, 2012). In a subsequent neutron scattering study of the effect of uniaxial pressure on T_N and T_s in NaFeAs, as-grown and annealed $BaFe_2As_2$ (Song, Carr *et al.*, 2013), it was found that while the uniaxial strain necessary to detwin the sample indeed induces a significant increase in T_N and T_s for as-grown $BaFe_2As_2$, similar uniaxial pressure used to detwin NaFeAs and annealed $BaFe_2As_2$ has a very small effect on their T_N and T_s. These results suggest that resistivity anisotropy observed in transport measurements (Fisher, Degiorgi, and Shen, 2011) is an intrinsic property of these materials (Song, Carr *et al.*, 2013).

In a recent systematic study of magnetic and structural transitions of the as-grown parent and lightly Co-doped $Ba(Fe_{1-x}Co_x)_2As_2$ under uniaxial pressure (Dhital *et al.*, 2014), it was found that the uniaxial strain induces a thermal shift in the onset of AF order that grows as a percentage of T_N as Co doping is increased and the superconducting phase is approached. In addition, they found a decoupling between the onsets of the T_s and T_N under uniaxial strain for parent and

lightly doped $Ba(Fe_{1-x}Co_x)_2As_2$ on the first order side of the tricritical point (Dhital *et al.*, 2014).

At around the same time, elastic and inelastic neutron scattering experiments were carried out on the annealed $BaFe_2As_2$ ($T_N = 138$ K), $BaFe_{1.915}Ni_{0.085}As_2$ ($T_c = 16.5$ K, $T_N = 44$ K), and $BaFe_{1.88}Ni_{0.12}As_2$ ($T_c = 18.6$ K, tetragonal structure without static AF order) to study the temperature dependence of the spin-excitation anisotropy at the in-plane wave vectors (1,0) and (0,1) (Lu, Park *et al.*, 2014). By comparing the temperature dependence of the magnetic order parameters at wave vectors (1,0,1) and (0,1,1) in zero and ~15 MPa uniaxial pressure on annealed $BaFe_2As_2$ [Fig. 32(c)], it was concluded that the applied uniaxial strain is sufficient to completely detwin the sample and does not affect much T_N. Furthermore, temperature dependence of the intensity at the $(2, -2, 0)$ nuclear Bragg reflection for the twinned and detwinned samples both show a dramatic jump at $T_s = 138$ K arising from the neutron extinction release that occurs due to strain and domain formation related to the orthorhombic lattice distortion, indicating that the uniaxial pressure does not change the tetragonal-to-orthorhombic structural transition temperature [Fig. 32(d)]. Since the measurable extinction release at temperatures well above T_s was suggested to arise from significant structural fluctuations related to the orthorhombic distortion (Kreyssig *et al.*, 2010), data for the detwinned sample indicate that the applied uniaxial pressure pushes structural fluctuations to a temperature similar to that at which resistivity anisotropy emerges. These results are different from those of Dhital *et al.* (2014) carried out on as-grown $BaFe_2As_2$. It remains to be seen how the different results in these experiments can be reconciled (Dhital *et al.*, 2012, 2014; Song, Carr *et al.*, 2013; Lu, Park *et al.*, 2014).

In addition to determining the effect of uniaxial strain on the structural and magnetic phase transitions in annealed $BaFe_2As_2$, inelastic neutron scattering experiments on $BaFe_{2-x}Ni_xAs_2$ also reveal that low-energy spin excitations in these materials change from fourfold symmetric to twofold symmetric in the uniaxial-strained tetragonal phase at temperatures approximately corresponding to the onset of in-plane resistivity anisotropy (Lu, Park *et al.*, 2014). The inset in Fig. 33(a) shows the in-plane resistivity anisotropy on annealed $BaFe_2As_2$ under uniaxial strain. Temperature dependence of the $E = 6$ meV spin excitations (signal above background scattering) at (1,0,1) and (0,1,1) is shown in Fig. 33(a). In the AF ordered state, there are only spin waves at the AF wave vector $\mathbf{Q}_{AF} = (1, 0, 1)$. On warming to the paramagnetic tetragonal state above T_N and T_s, we see clear differences between (1,0,1) and (0,1,1) that vanish above ~160 K, the same temperature below which anisotropy is observed in the in-plane resistivity [inset in Fig. 33(a)]. Similar measurements on underdoped $BaFe_{1.915}Ni_{0.085}As_2$ reveal that the $E = 6$ meV spin excitations at the (1,0,1) and (0,1,1) wave vectors become anisotropic below ~80 K [Fig. 33(b)], again consistent with the in-plane resistivity anisotropy from uniaxial strain detwinned $BaFe_{2-x}Ni_xAs_2$ [Fig. 33(c)] (Fisher, Degiorgi, and Shen, 2011). Finally, uniaxial strain on electron-overdoped $BaFe_{1.88}Ni_{0.12}As_2$ induces neither spin excitations nor in-plane resistivity anisotropy at all temperatures (Fisher, Degiorgi, and Shen, 2011; Lu, Park *et al.*, 2014). Therefore, resistivity and spin-excitation anisotropies both vanish near optimal superconductivity and are likely intimately connected, consistent with spin nematic phase induced electronic anisotropy (Fernandes, Chubukov, and Schmalian, 2014).

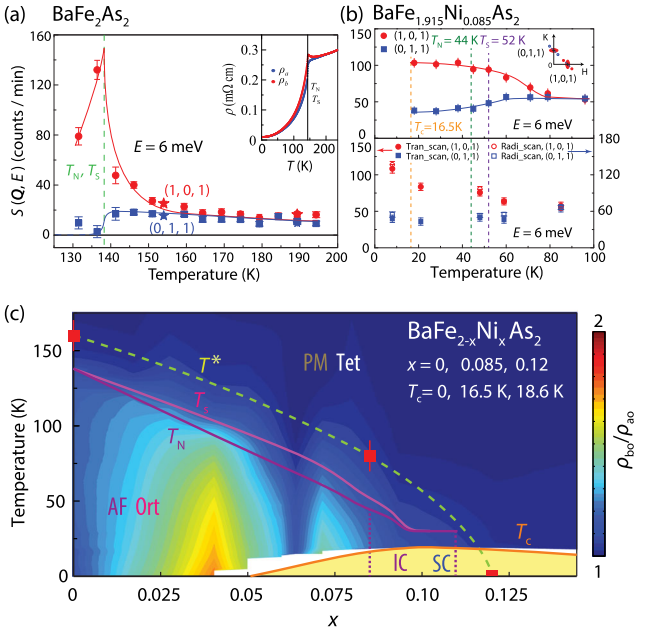

FIG. 33 (color online). Temperature dependence of the spin-excitation anisotropy at wave vectors (1,0,1) and (0,1,1) and its comparison with transport measurements for $BaFe_{2-x}Ni_xAs_2$. (a) Temperature dependence of spin excitations at $E = 6$ meV for (1,0,1) and (0,1,1) under $P \sim 15$ MPa uniaxial pressure. The anisotropy in spin excitations vanishes around $T = 160 \pm 10$ K. The inset shows the transport measurement of the in-plane resistivity anisotropy for the annealed $BaFe_2As_2$. (b) Temperature dependence of $E = 6$ meV spin excitations at (1,0,1) and (0,1,1) for $BaFe_{1.915}Ni_{0.085}As_2$. The data in the top panel were obtained by subtracting the background intensity from the peak intensity at every temperature; the data in the bottom panel were obtained by fitting the wave vector scans. (c) The electronic phase diagram of $BaFe_{2-x}Ni_xAs_2$ from resistivity anisotropy ratio ρ_{bo}/ρ_{ao} obtained under uniaxial pressure. The spin-excitation anisotropy temperatures are marked as T^*. The AF orthorhombic (Ort), incommensurate AF (IC), paramagnetic tetragonal (PM Tet), and superconductivity (SC) phases are marked. From Lu, Park *et al.*, 2014.

H. Comparison of magnetic order and spin excitations from neutron scattering

In the previous discussions, we summarized recent progress in the AF order and spin dynamics in iron-based high temperature superconductors determined from elastic and inelastic neutron scattering. However, neutron scattering is not the only technique to study magnetism in these materials. Other probes such as μSR, NMR, and RIXS experiments have also been used to investigate their magnetic properties. Compared with neutron scattering, which is a bulk probe determining the average magnetic properties of the solids, the μSR technique is a local probe measuring the magnitude of the static random field experienced by muons that reside on

interstitial lattice sites of the studied material. In addition to being able to detect static AF order and superfluid density, it can determine the volume fractions of the magnetic and superconducting phases and their temperature dependence (Uemura, 2009; Carretta *et al.*, 2013). Similarly, NMR is also a local probe that can detect magnetic and superconducting properties of the studied materials (Alloul *et al.*, 2009). In this section, we briefly summarize recent results from these techniques and compare them with results obtained from neutron scattering.

We begin by comparing the electronic phase diagrams of electron-doped $Ba(Fe_{1-x}Co_x)_2As_2$ determined from x-ray and neutron scattering (Nandi *et al.*, 2010; Pratt *et al.*, 2011) with those determined from the μSR measurements [Fig. 34(a)] (Bernhard *et al.*, 2012). For Co-doped samples in the underdoped regime ($x \leq 0.045$), the μSR results find a full volume AF ordered phase coexisting and competing with superconductivity. This is consistent with neutron diffraction results indicating static commensurate AF order coexists and competes with superconductivity in the underdoped regime (Fig. 13) (Christianson *et al.*, 2009; Pratt *et al.*, 2009). For $Ba(Fe_{1-x}Co_x)_2As_2$ near optimal superconductivity with $x \geq 0.05$, magnetic order develops only in parts of the sample volume, and the normalized values of the average magnetic field at the muon site B_μ are reduced dramatically [Fig. 34(b)].

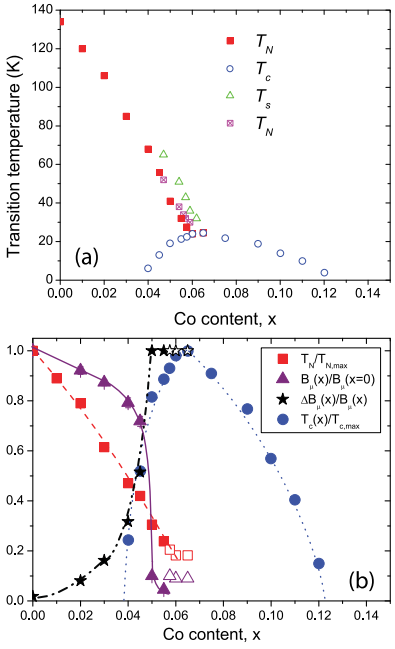

FIG. 34 (color online). The electronic phase diagram of $Ba(Fe_{1-x}Co_x)_2As_2$ as determined from combined μSR and neutron diffraction experiments. (a) Phase diagram of T_N, as determined with μSR and T_c, obtained from resistivity and magnetic susceptibility measurements as well as from the specific heat data. (b) The Co dependence of the normalized T_N and T_c, and the normalized values of the average magnetic field at the muon site B_μ and of its relative spread ΔB_μ. The open symbols show the magnetic properties in the spatially inhomogeneous magnetic state near optimum doping. From Bernhard *et al.*, 2012.

In addition, the AF Néel temperature of the system saturates to a value near or slightly above T_c before vanishing in a first order fashion with increasing Co doping [Fig. 34(b)] (Bernhard *et al.*, 2012). This region of Co doping is consistent with the appearance of the transverse incommensurate AF order seen in neutron diffraction experiments (Pratt *et al.*, 2011). However, instead of a uniform incommensurate spin-density-wave ordered phase, the μSR data indicate a spatially inhomogeneous magnetic state for which the volume fraction of the ordered phase decreases with increasing Co doping (Bernhard *et al.*, 2012). The NMR measurements on $Ba(Fe_{1-x}Co_x)_2As_2$ samples near optimal superconductivity reveal that the system is in the spin-glass state which competes with superconductivity (Dioguardi *et al.*, 2013). Instead of being a consequence of Fermi surface nesting (Pratt *et al.*, 2011), the incommensurate magnetic order in Co-doped $BaFe_2As_2$ may arise from inhomogeneous short-range magnetic order similar to the moment modulating cluster spin glass in Ni-doped $BaFe_2As_2$ (Lu *et al.*, 2014). Therefore, the electronic phase diagrams of the Co- and Ni-doped $BaFe_2As_2$ are similar, showing a homogeneous commensurate long-range static AF ordered phase competing with superconductivity in the underdoped region and a short-range spin-glass phase near optimal superconductivity [Fig. 5(b)] (Bernhard *et al.*, 2012; Luo *et al.*, 2012; Dioguardi *et al.*, 2013; Lu *et al.*, 2013, 2014). There is no evidence for a conventional magnetic quantum critical point near optimal superconductivity, and the AF order disappears in the superconducting phase with increasing Co or Ni doping in a first order fashion (Bernhard *et al.*, 2012; Luo *et al.*, 2012; Dioguardi *et al.*, 2013; Lu *et al.*, 2013, 2014).

The electron phase diagrams of the Co- and Ni-doped $BaFe_2As_2$ systems have also been mapped out by NMR measurements [Figs. 35(a) and 35(d)] (Ning *et al.*, 2009, 2010; R. Zhou *et al.*, 2013). In the case of $Ba(Fe_{1-x}Co_x)_2As_2$, the NMR experiments on electron-overdoped samples suggest that the absence of quasiparticle excitations with momentum transfer $\mathbf{Q}_{AF}$ between the hole and electron Fermi surfaces results in complete suppression of the low-energy spin fluctuations for $x \geq 0.15$. The insets in Fig. 35(a) show that the hole bands sink below the Fermi surface for $x \geq 0.15$, disallowing interband quasiparticle transitions between the hole and electron Fermi surfaces (Ning *et al.*, 2010). These results are consistent with neutron scattering data on electron-doped $BaFe_{2-x}Ni_xAs_2$, where there is a large (~50 meV) spin gap in the nonsuperconducting sample with $x = 0.3$ (M. Wang *et al.*, 2013).

In addition to determining the electronic phase diagram of $Ba(Fe_{1-x}Co_x)_2As_2$ as shown in Fig. 35(a), the $1/T_1T$ obtained by NMR measurements is also related to the wave vector integral of the low-energy spin dynamic susceptibility $\chi''(\mathbf{Q}, f)$ via $1/T_1T = A/(T-\theta) \sim \sum_{\mathbf{Q}} |A(\mathbf{Q})|^2 \chi''(\mathbf{Q}, f)/f$, where θ is the Curie-Weiss temperature (the temperature at which a plot of the reciprocal molar magnetic susceptibility against the absolute temperature T intersects the T axis), f is the NMR frequency, a is the lattice constant, $|A(\mathbf{Q})|^2 = |A\cos(Q_x a/2)\cos(Q_y a/2)|^2$ is the form factor of transferred hyperfine coupling at the ^{75}As sites, and the wave vector summation of $\mathbf{Q}$ is taken over the entire first Brillouin zone (Ning *et al.*, 2009). By measuring the

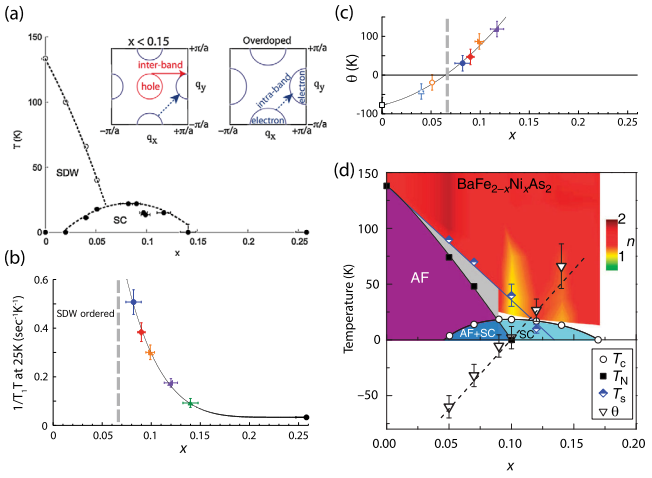

FIG. 35 (color online). NMR determination of the phase diagram for electron-doped iron pnictides. (a) The AF order T_N and T_c in $Ba(Fe_{1-x}Co_x)_2As_2$ as determined from the NMR measurements. The left and right insets are schematic representations of the Fermi surfaces in unfolded first Brillouin zone for the $x < 0.15$ and overdoped nonsuperconducting samples, respectively. The absence of electron-hole Fermi surface nesting is believed to be responsible for the suppression of superconductivity in the overdoped regime. (b) The Co-doping dependence of the strength of the paramagnetic spin excitations as measured by $1/T_1T$ at 25 K ($\geq T_c$). (c) Weiss temperature θ obtained from fitting the interband (electron-hole pocket excitations) AF spin excitations $(1/T_1T)_{\text{inter}}$ with a Curie-Weiss term $(1/T_1T)_{\text{inter}} = C/(T+\theta)$. Here $1/T_1T = (1/T_1T)_{\text{inter}} + (1/T_1T)_{\text{intra}}$, where the intraband scattering can be fitted with a phenomenological form $(1/T_1T)_{\text{intra}} = \alpha + \beta\exp(-\Delta/k_BT)$. From Ning *et al.*, 2010. (d) The electronic phase diagram of $BaFe_{2-x}Ni_xAs_2$ as determined from NMR and transport measurements. From R. Zhou *et al.*, 2013.

Co-doping dependence of $1/T_1T$, one can fit the data with Curie-Weiss law and obtain the electron-doping dependence of θ. Figures 35(b) and 35(c) show the Co-doping dependence of the $1/T_1T$ in the normal state ($T \geq T_c$) and $\theta(K)$, respectively (Ning *et al.*, 2010). The enhancement of $1/T_1T$ and the negative to positive crossing of $\theta(K)$ near vanishing AF order suggest the presence of a magnetic quantum critical point at $x \approx 0.07$ (Ning *et al.*, 2010). Similar NMR data and transport measurements on $BaFe_{2-x}Ni_xAs_2$ suggest the presence of two quantum critical points associated with AF order and the tetragonal-to-orthorhombic lattice distortions, respectively [Fig. 35(d)] (R. Zhou *et al.*, 2013). These results are in direct contrast to the conclusions of neutron scattering and μSR experiments as described earlier, which suggests a weakly first order phase transition from static AF order to superconductivity in electron-doped $BaFe_2As_2$. We note that these NMR measurements have not been carried out for the Co- and Ni-doped samples with incommensurate magnetic order and near optimal superconductivity (Ning *et al.*, 2010; R. Zhou *et al.*, 2013).

Although determining whether a conventional magnetic quantum critical point exists in the iron pnictides is important, it is equally important to understand what happens to the tetragonal-to-orthorhombic lattice distortion in the Co- and Ni-doped $BaFe_2As_2$ phase diagram near optimal superconductivity. From initial high-resolution x-ray diffraction experiments, it was suggested that $Ba(Fe_{1-x}Co_x)_2As_2$ has reentrant behavior near optimal superconductivity, exhibiting a tetragonal-orthorhombic transition above T_c and orthorhombic-tetragonal structural transition below T_c (Nandi *et al.*, 2010). While the overall trends of these results were confirmed by later high-resolution x-ray diffraction experiments on $BaFe_{2-x}Ni_xAs_2$ near optimal superconductivity, the presence of low-temperature incommensurate AF order suggests that the system is still in the orthorhombic phase (Lu *et al.*, 2013). Using resonant ultrasonic spectroscopy, one can measure the temperature dependence of the anisotropic elastic stiffness C_{ij} associated with the tetragonal-orthorhombic lattice distortion in $Ba(Fe_{1-x}Co_x)_2As_2$ (Fernandes *et al.*, 2010; Yoshizawa *et al.*, 2012). Figures 36(a) and 36(b) show temperature dependence of the resonant ultrasonic spectroscopy measured squared resonant frequency f^2 (squares), and of the calculated elastic stiffness (shear modulus) $C_s \equiv C_{66}$ of the tetragonal phase (solid lines) for $BaFe_2As_2$ and $BaFe_{1.84}Co_{0.16}As_2$, respectively (Fernandes *et al.*, 2010). The dramatic softening of the C_{66} shear modulus at temperatures above the tetragonal-orthorhombic lattice distortion temperature T_s has been interpreted as due to the spin nematic phase (Fernandes *et al.*, 2010). Figure 36(c) shows

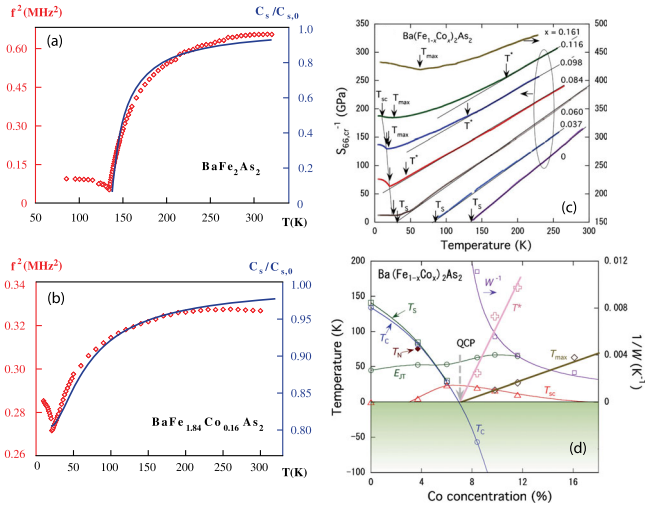

FIG. 36 (color online). The elastic properties of the iron-based superconductor $Ba(Fe_{1-x}Co_x)_2As_2$ as determined from ultrasonic spectroscopy measurements. The temperature dependence of the anisotropic elastic stiffness C_{66} for (a) $BaFe_2As_2$ and (b) $BaFe_{1.84}Co_{0.16}As_2$ as determined from resonant ultrasonic spectroscopy. The solid lines are fits from a model considering spin nematic phase. From Fernandes *et al.*, 2010. (c) Temperature dependence of the inverse of the elastic stiffness $S_{66} = 1/C_{66} = S_{66}^0 + S_{66,\text{Cr}}$, where S_{66}^0 is the normal (background) contribution for $Ba(Fe_{1-x}Co_x)_2As_2$ with different x. (d) Structural and magnetic phase diagram of $Ba(Fe_{1-x}Co_x)_2As_2$ as determined from ultrasonic spectroscopy measurements. A structural quantum critical point is identified near optimal superconductivity. From Yoshizawa *et al.*, 2012.

temperature dependence of the inverse of C_{66} for Co-doping levels of $x = 0$, 0.037, 0.060, 0.084, 0.098, 0.116, 0.161, and 0.245 (Yoshizawa *et al.*, 2012). The resulting phase diagram shown in Fig. 36(d) suggests the presence of a structural quantum critical point near $x \approx 0.07$. While this is consistent with the NMR results of a magnetic quantum critical point (Ning *et al.*, 2009, 2010), it differs from the first order nature of the AF order to superconducting phase transition in electron-doped pnictides determined from neutron and μSR experiments (Bernhard *et al.*, 2012; Dioguardi *et al.*, 2013; Lu *et al.*, 2013, 2014).

In the past, the only way to explore the energy and wave vector dependence of the spin excitations in materials was via inelastic neutron scattering, which in principle can map out the spin excitations in absolute units from low energy to high energy throughout the Brillouin zone as described in Sec. III. However, such a technique suffers from the need for large amounts of single crystals, which may not be available. Recent advances in RIXS provide an alternative method to look for high-energy spin excitations in copper (Tacon *et al.*, 2011) and iron (K.-J. Zhou *et al.*, 2013) based high-T_c superconductors, although the precise RIXS cross section is difficult to calculate and includes couplings to orbital and electronic excitations in addition to magnetic excitations (Ament *et al.*, 2011). For the hole-doped $YBa_2Cu_3O_{6+x}$ family of materials, RIXS measurements showed the existence of damped but well-defined dispersive magnetic excitations, deep in the Stoner continuum of hole-doped cuprates with doping beyond the optimal level (Tacon *et al.*, 2011). The high-energy spin-excitation spectral weights are found to be similar to those of spin waves in the undoped, antiferromagnetically ordered parent material (Tacon *et al.*, 2011). So far, these measurements on hole-doped copper oxide superconductors have not been independently confirmed by inelastic neutron scattering experiments, which mostly probe spin excitations near the AF ordering wave vector instead of near the origin as in RIXS experiments due to the small neutron scattering cross section near Γ (Fig. 4) (Fujita *et al.*, 2012; Tranquada, Xu, and Zaliznyak, 2014). Given that the RIXS cross section is not well known (Ament *et al.*, 2011), it is extremely important to compare inelastic neutron scattering and RIXS experiments on similar samples. Recently, such a comparison was made for high-energy spin excitations of $Sr_2CuO_2Cl_2$ (Plumb *et al.*, 2014).

Figure 37(a) shows a schematic view of the reciprocal space that can be covered by Fe L_3 RIXS shaded by a circle. Squares represent the tetragonal (orthorhombic) Brillouin zone (K.-J. Zhou *et al.*, 2013). Similar to the case of copper oxide superconductors, RIXS by Fe L_3 edge will not be able to cover the same region of the reciprocal space as that of inelastic neutron scattering [Fig. 4(e)]. Figure 37(b) plots Fe L_3 edge x-ray absorption spectrum on $BaFe_2As_2$ collected at 15 K with π polarized incoming light, at $(Q_x, Q_y) = (0, 0)$ (Γ), (0.5,0) (B), and (0.35, 0.35) (C) using orthorhombic reciprocal lattice units [see Fig. 37(a) for the Γ, B, and C positions in reciprocal space]. In addition to the intense Fe 3d fluorescence at around −2 eV energy transfer, there are momentum dispersive excitations centered around 200 meV near the quasielastic peak at zero energy [Fig. 37(b)]. Since the dispersions of these excitations are identical to those of

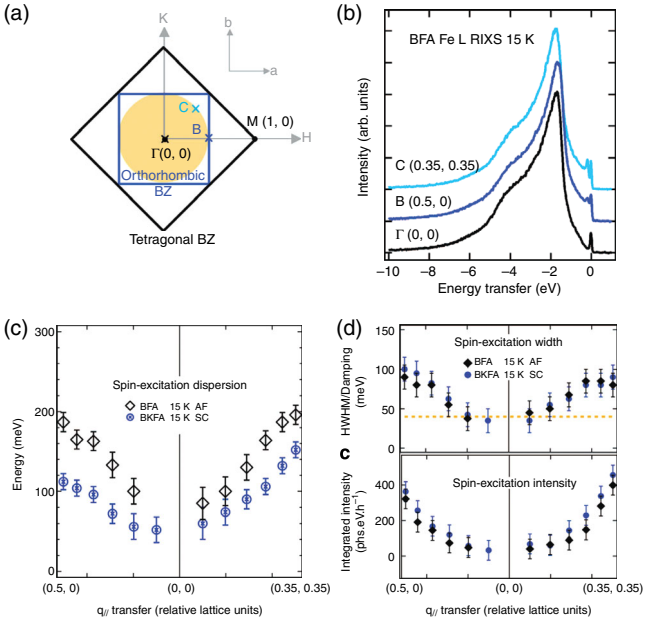

FIG. 37 (color online). RIXS measurements of the high-energy spin excitations in optimally hole-doped $BaFe_2As_2$. (a) Schematic view of the reciprocal space covered by Fe L_3 RIXS is shaded by a circle. Γ, B, and C are the reciprocal space positions at which RIXS spectra were collected. Squares represent the tetragonal (orthorhombic) Brillouin zone. All RIXS spectra use the orthorhombic Brillouin-zone convention for defining relative momentum transfer values. The Γ point is the structural zone center, while Γ-M is the AF ordering wave vector. (b) Three typical RIXS spectra of BFe_2As_2 collected at 15 K with π polarized incoming light, at Γ, B, and C positions in reciprocal space. (c) Dispersion of spin excitations of BFe_2As_2 (BFA) in the AF phase, and $Ba_{0.6}K_{0.4}Fe_2As_2$ (BKFA) in the superconducting phase. (d) Half width at half maximum (HWHM, damping) and integrated intensity of spin excitations of BFA and BKFA. The horizontal dotted line in the upper panel marks the HWHM of the total instrumental resolution of the RIXS experiment (40 meV). From K.-J. Zhou *et al.*, 2013.

spin waves in $BaFe_2As_2$ determined from inelastic neutron scattering [Fig. 37(c)] (Harriger *et al.*, 2011), they are believed to arise from the same spin waves in $BaFe_2As_2$ measured by RIXS (K.-J. Zhou *et al.*, 2013). Similar RIXS measurements on optimally hole-doped superconducting $Ba_{0.6}K_{0.4}Fe_2As_2$ (BKFA) indicate that while the dispersions of spin excitations are softened [Fig. 37(c)], the excitation intensity and widths are unchanged from its undoped parent $BaFe_2As_2$ [Fig. 37(d)] (K.-J. Zhou *et al.*, 2013). This is a surprising result, different from the hole-doping evolution of the high-energy spin excitations in copper oxides (Tacon *et al.*, 2011). While the dispersion of the spin excitations in BKFA determined by RIXS was confirmed by later inelastic neutron scattering experiments, the absolute spin-excitation intensity in BKFA measured by neutrons is much smaller than that of the spin waves in $BaFe_2As_2$ (M. Wang *et al.*, 2013). At present, it is unclear how to reconcile the RIXS and neutron scattering results, although we note that region of the reciprocal space probed by RIXS is different from that probed by inelastic neutron scattering.

As discussed in the Introduction, neutron scattering can measure the overall strength of the magnetic excitations through the local fluctuating moment $\langle \mathbf{m}^2 \rangle$. For a local-moment Heisenberg model with spin S, the integrated spectral weight when integrated over all wave vector and energy space should yield $M_0^2 = M^2 + \langle \mathbf{m}^2 \rangle = g^2 S(S+1)$ in units of μ_B^2. Therefore, one can in principle determine the magnitude of S by measuring elastic (with static ordered moment M in units of μ_B) and inelastic magnetic scattering of the system in absolute units throughout the Brillouin zone, and the outcome should be the same as the local moment S determined from the x-ray emission spectroscopy (XES) (Rueff and Shukla, 2010) and core level photoemission spectra (PES) (Vilmercati *et al.*, 2012). However, the current unpolarized time-of-flight neutron scattering technology can measure only correlated spin excitations, and thus will underestimate the size of the effective spin S when spin excitations become diffusive and broad as in the case of most iron pnictides [except for the true local-moment system $Rb_{0.89}Fe_{1.58}Se_2$ (M. Y. Wang *et al.*, 2011)]. By measuring the local dynamic susceptibility for electron-doped $BaFe_{2-x}Ni_xAs_2$, we see that the magnitude of $\langle \mathbf{m}^2 \rangle$ decreases from $\langle \mathbf{m}^2 \rangle \approx 3.5\ \mu_B^2/\mathrm{Fe}$ for $x = 0$ to $(2.7 \pm 0.1)\ \mu_B^2/\mathrm{Fe}$ for $x = 0.3$, corresponding to $S \approx 1/2$ if we ignore the static ordered moment contribution ($M^2 \approx 0.64\ \mu_B^2/\mathrm{Fe}$ for $x = 0$) to the total magnetic moment ($M_0^2 \approx \langle \mathbf{m}^2 \rangle$) (Luo, Lu *et al.*, 2013; M. Wang *et al.*, 2013).

Figure 38(a) shows the local moment S for various iron-based superconductors in the paramagnetic phase as determined from XES (Gretarsson *et al.*, 2011). Here the material variation of the local moment of Fe can be extracted using the overall shape of the Fe $K\beta$ emission spectra by applying the integrated absolute difference (IAD) analysis. The absolute values of S were obtained by scaling the results to neutron scattering data. Figure 38(b) plots the temperature dependence of the IAD for $Ca_{0.92}Nd_{0.08}Fe_2As_2$, $Ca_{0.78}La_{0.22}Fe_2As_2$, and $Ca_{0.85}Nd_{0.15}Fe_2As_2$ (Gretarsson *et al.*, 2013). The local moments in the Nd- and Pr-doped samples disappear in the cT phase (Goldman *et al.*, 2009), indicating that the Fe^{2+} ions go through a spin-state transition by taking on the low-spin state in the cT phase. Inelastic neutron scattering experiments on $CaFe_2As_2$ also reveal vanishing spin excitations in the cT phase (Soh *et al.*, 2013), similar to the XES results (Gretarsson *et al.*, 2013). Figure 38(c) shows the values of the local Fe moment for various iron pnictides estimated from PES measurements (Vilmercati *et al.*, 2012). We see that the values of $\approx 2\ \mu_B/\mathrm{Fe}$ for $BaFe_2As_2$ and $SrFe_2As_2$ family of iron pnictides, corresponding to $S \approx 1$, are much larger than those obtained by inelastic neutron scattering, and decrease by about 40% in the optimally doped compound, also different from doping dependence results from neutron scattering (Mannella, 2014). As emphasized by Mannella (2014), the PES experiments sample spin excitations on time scales shorter than $10^{-15} - 10^{-16}$ s, while inelastic neutron scattering measurements probing spin excitations up to ~300 meV correspond to time scales on the order of 10–15 fs, at least 1 or 2 orders of magnitude slower than those in PES experiments. Furthermore, PES measurements determine the total uncorrelated spin while present inelastic neutron scattering measures correlated spin excitations near the AF ordering wave vector within the (1,0) Brillouin zone.

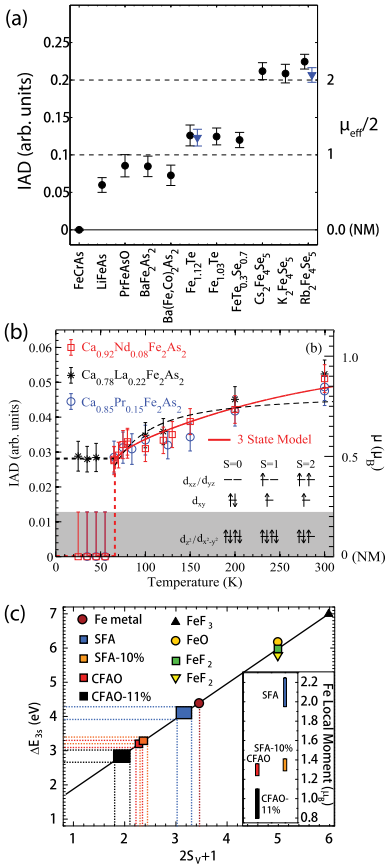

FIG. 38 (color online). Local moments of various iron-based superconductors in their paramagnetic states determined by x-ray emission spectroscopy and core level photoelectron spectroscopy. (a) The IAD values derived from the XES spectra for various samples. The room-temperature data are shown by circles, and the low-temperature IAD values at $T = 15$ K are shown as triangles for $Fe_{1.12}Te$ and $Rb_2Fe_4Se_5$. From Gretarsson *et al.*, 2011. The right-hand axis is scaled to the total (static + fluctuating) moments of $Rb_{0.89}Fe_{1.58}Se_2$. From M. Y. Wang *et al.*, 2011 (Y.-J. Kim, private communication). (b) Temperature dependence of the IAD values for $Ca_{0.92}Nd_{0.08}Fe_2As_2$, $Ca_{0.78}La_{0.22}Fe_2As_2$, and $Ca_{0.85}Nd_{0.15}Fe_2As_2$. From Gretarsson *et al.*, 2013. (c) Estimation of the spin moment on the Fe sites from the multiplet energy separation ΔE_{3S} obtained from the PES measurement. The continuous line is the extrapolation of the linear fit of the ΔE_{3S} values plotted vs $2S_V + 1$ for the Fe ionic compounds FeF_3, FeF_2, and FeO, for which S_V is known to be $5/2$ (FeF_3) and 2 (FeF_2, FeO). Here SFA, SFA-10%, CFAO, and CFAO-11% are $SrFe_2As_2$, $SrFe_{1.76}Co_{0.24}As_2$, CeFeAsO, and $CeFeAsO_{0.89}Fe_{0.11}$, respectively. The linear fit results in the relation $\Delta E_{3S} = 0.94 + 1.01(2S_V + 1)$. From Vilmercati *et al.*, 2012.

I. Comparison of spin excitations in iron-based superconductors

With the discovery of $La_{2-x}Ba_xCuO_4$ family of copper oxide superconductors in 1986 (Bednorz and Müller, 1986), the field of high-T_c superconductivity was born. Although research in high-T_c copper oxide superconductors is still

active with many exciting new results almost 30 years later (Fradkin and Kivelson, 2012; Ghiringhelli *et al.*, 2012), the discovery of iron-based superconductors in 2008 provided an entire new class of materials where high-T_c superconductivity occurs (Kamihara *et al.*, 2008). Since high-T_c copper oxide and iron-based superconductors as well as heavy fermion superconductors are close to AF instability, magnetism may be a common thread for unconventional superconductivity (Scalapino, 2012). If this is indeed the case, it will be interesting to determine the similarities and differences in spin excitations of these superconductors.

As discussed by Fujita *et al.* (2012) and Tranquada, Xu, and Zaliznyak (2014), an important feature of the spin excitations in copper oxide superconductors is the neutron spin resonance and hourglasslike dispersion of the spin-excitation spectra. An hourglass magnetic spectrum is also seen in an insulating, hole-doped antiferromagnet $La_{5/3}Sr_{1/3}CoO_4$ (Boothroyd *et al.*, 2011). Figure 39(a) shows the spin-excitation dispersions of different copper oxide superconductors away from the AF ordering wave vector $\mathbf{Q}_{\rm AF} = (0.5, 0.5)$, where J is the nearest neighbor magnetic exchange coupling ($J \approx 120$ meV) (Fujita *et al.*, 2012; Tranquada, Xu, and Zaliznyak, 2014). While the hourglass dispersion of spin excitations appears to be a ubiquitous feature of different families of hole-doped copper oxide superconductors, they are clearly absent in spin-excitation spectra of electron-doped iron pnictides. For optimally hole-doped iron pnictides, spin excitations change from longitudinally to transversely elongated ellipses centered at $\mathbf{Q}_{\rm AF} = (1, 0)$ on moving from below the resonance energy to above it (M. Wang *et al.*, 2013). This is different from the hourglass dispersion seen in hole-doped copper oxides. Another important feature of the spin-excitation spectra is the electron- and hole-doping evolution of the local dynamic susceptibility. For hole-doped copper oxide superconductors,

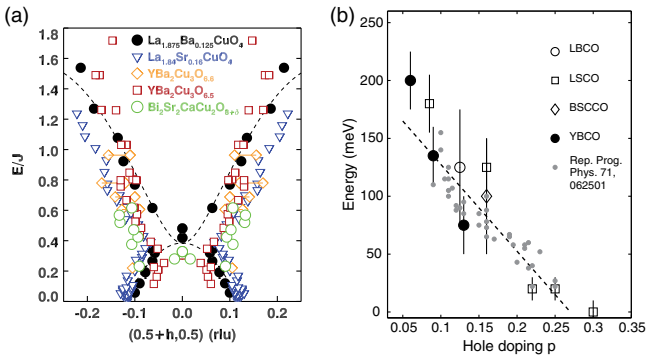

FIG. 39 (color online). The dispersions of spin excitations in various copper oxide superconductors and the energy scale of the spin excitations. (a) Magnetic dispersion relation along the $(0.5 + h, 0.5, 0)_{\rm tetra}$ in various cuprates, corresponding to wave vectors parallel to the Cu-O bonds. The energy is scaled by $J \sim 110$ meV for the AF parent compound La_2CuO_4. (b) Large symbols: Estimates of a doping-dependent energy scale at which magnetic spectral weight falls below half that of the AF state based on inelastic neutron scattering studies of various cuprates. From Stock *et al.*, 2010a. Small circles: Pseudogap energy from various electronic spectroscopies. From Tranquada, Xu, and Zaliznyak, 2014.

the strength of the high-energy magnetic response near $\mathbf{Q}_{\rm AF} = (0.5, 0.5)$ decreases with increasing doping level. To quantify this behavior, Stock *et al.* (2010b) evaluated the hole-doping dependence of the energy at which the local dynamic susceptibility $\chi''(\omega)$ falls below half of that for an undoped AF parent compound. The outcome suggests that the hole dependence of the magnetic energy scale corresponds very well with the pseudogap energy determined from electronic spectroscopies [Fig. 39(b)] (Hüfner *et al.*, 2008). These results indicate that AF spin excitations in copper oxides decrease dramatically with increasing hole doping. Although there are only limited data available for hole-doped iron pnictides (M. Wang *et al.*, 2013), they show a similar trend to that of hole-doped copper oxides. More inelastic neutron scattering experiments on hole-doped iron pnictides are necessary in order to make a detailed comparison between spin excitations in iron- and copper-based high-T_c superconductors.

As discussed in Sec. III.H, recent advances in RIXS allowed a direct study of spin excitations in copper- and iron-based superconductors. However, the results obtained by RIXS for hole-doped iron pnictides disagree with those obtained by inelastic neutron scattering (M. Wang *et al.*, 2013; K.-J. Zhou *et al.*, 2013). RIXS measurements on copper oxide superconductors also find excitations that soften no more than 10% with doping, with negligible change in integrated intensity. While these results are very similar to those obtained on iron pnictides (K.-J. Zhou *et al.*, 2013), they are again in conflict with those of inelastic neutron scattering probing spin excitations near $\mathbf{Q}_{\rm AF} = (0.5, 0.5)$ (Tranquada, Xu, and Zaliznyak, 2014). As the RIXS cross section includes both charge and spin excitations (Ament *et al.*, 2011), it is not known how to directly compare the RIXS intensity with that of the well-established magnetic cross section obtained from inelastic neutron scattering.

In the case of electron-doped copper oxide superconductors, recent RIXS experiments confirmed that magnetic excitations harden across the antiferromagnetism and superconductivity boundary seen originally with neutron scattering experiments (Fujita *et al.*, 2006; Wilson, Li *et al.*, 2006; W. S. Lee *et al.*, 2013). However, RIXS finds a negligible change in the integrated magnetic intensity as a function of electron doping at high energies, again in conflict with neutron scattering results on similar materials (Fujita *et al.*, 2006; Wilson, Li *et al.*, 2006; W. S. Lee *et al.*, 2013). While one can directly compare spin waves measured in neutron scattering experiments with RIXS in the AF ordered phase of copper oxide and iron-based materials due to symmetry of the equivalent Brillouin zones (see dashed box near Γ and shaded box near $\mathbf{Q}_{\rm AF}$ in Fig. 3), there is no physical justification for assuming that the excitations measured by RIXS near the Γ ($\mathbf{Q} = 0$) point are the same as those near $\mathbf{Q}_{\rm AF}$ obtained by neutron scattering for a doped metallic sample (Tranquada, Xu, and Zaliznyak, 2014). Whereas the neutron scattering cross section is well understood, the RIXS cross section is complicated and the significance of the RIXS measurements is unclear at present. Only future RIXS and neutron scattering measurements performed on the same sample at the same region of the reciprocal space will shed new light on our understanding of the spin and electronic excitations as

revealed by RIXS and determine their significance to high-T_c superconductivity.

In addition to copper- and iron-based superconductors, unconventional superconductivity also includes heavy fermion superconductors (Steglich *et al.*, 1979; Stewart, 2001; Löhneysen, H. *et al.*, 2007; Gegenwart, Si, and Steglich, 2008). Compared with iron- and copper-based superconductors, the parent compounds of heavy fermion superconductors are also long-range ordered antiferromagnets but with a magnetic exchange coupling energy scale much lower than that of the AF parents of copper oxide and iron-based superconductors. For example, in a recent study of spin waves in AF ordered $CeRhIn_5$, the parent compound of the $CeCoIn_5$ family of heavy fermion superconductors (Thompson and Fisk, 2012), the dominant in-plane nearest neighbor magnetic exchange coupling is $SJ_0 = 0.74$ meV (Das *et al.*, 2014), much smaller than that of the AF parents of iron-based superconductors (see Table II). In spite of the dramatically reduced energy scale, heavy fermion superconductors still have some interesting features also seen in copper- and iron-based superconductors. A case in point is the neutron spin resonance in heavy fermion superconductors such as UPd_2Al_3 (Sato *et al.*, 2001) and $CeCoIn_5$ (Stock *et al.*, 2008).

Figure 40(a) shows the energy dependence of the spin excitations of $CeCoIn_5$ below and above T_c at $\mathbf{Q}_{AF} = (0.5, 0.5, 0.5)$ (Stock *et al.*, 2008). While the normal state spin excitations are featureless within the probed energy range, superconductivity induces a sharp peak reminiscent of the resonance in iron- and copper-based superconductors. From neutron polarization analysis of the resonance discussed in Sec. III.F, we know that the mode in iron-based superconductors is isotropic, consistent with the singlet-to-triplet excitation of electron Cooper pairs (Eschrig, 2006). If this is indeed the case, application of a magnetic field should Zeeman split the resonance into three peaks arising from a single ground state to a triplet excited state (Dai *et al.*, 2000), where the central field independent peak is longitudinally polarized while the field dependent peaks are transversely polarized (Ismer *et al.*, 2007). Unfortunately, magnetic field experiments on copper oxide (Dai *et al.*, 2000) and iron-based superconductors (Wen *et al.*, 2010; Zhao *et al.*, 2010; S. L. Li *et al.*, 2011) have been unable to determine the ground state of the resonance. Surprisingly, the application of a magnetic field on heavy fermion superconductor $CeCoIn_5$ splits the resonance into two peaks as shown in Figs. 40(b)–40(d) (Stock *et al.*, 2012). This suggests that the resonance in $CeCoIn_5$ is a doublet instead of a singlet-to-triplet excitation. In separate polarized inelastic neutron scattering experiments under a magnetic field, the double peak nature of the resonance was confirmed under a 2 T applied field (Raymond *et al.*, 2012). In addition, the resonance line shape is found to depend on the neutron polarization, suggesting that the resonance is a degenerate mode with three fluctuation channels: a Zeeman split contribution and an additional longitudinal mode (Raymond *et al.*, 2012). While these results on $CeCoIn_5$ are interesting, they still have not conclusively established the doublet or singlet-to-triplet nature of the resonance.

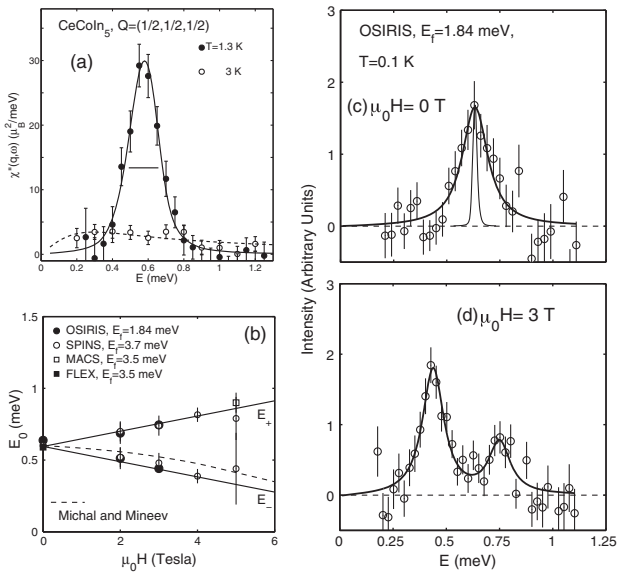

FIG. 40. Neutron spin resonance in heavy fermion superconductor $CeCoIn_5$ and its magnetic field dependence. (a) The imaginary part of the dynamic susceptibility at $\mathbf{Q}_{AF} = (1/2, 1/2, 1/2)$ in the normal (3 K) and superconducting (1.3 K) states. A background scattering taken at $\mathbf{Q} = (0.3, 0.3, 0.5)$ and (0.7,0.7,0.5) was subtracted. The horizontal bar is the instrumental resolution width. From Stock *et al.*, 2008. (b) The peak positions of the field spit resonance as a function of applied field within the *a*-*b* plane. The solid lines are fits to $E_\pm = \hbar\omega_0 \pm g\mu_B\mu_0 H/2$ with $g = 1.92 \pm 0.10$. (c) Resonance at zero applied magnetic field. (d) Identical scan under an applied field of 3 T. A 10 K background was subtracted from the scans. From Stock *et al.*, 2012.

Using established models to calculate the magnetic contributions to the superconducting condensation energy in copper oxide superconductors (Demler and Zhang, 1998; Scalapino and White, 1998), one can in principle estimate the lowering of the magnetic exchange energy in $YBa_2Cu_3O_{6+x}$ family of materials using spin-excitation spectra above and below T_c (Dai *et al.*, 1999; Woo *et al.*, 2006; Dahm *et al.*, 2009). However, the large energy scale of the spin excitations in high-T_c copper oxide superconductors means that it is difficult to obtain the overall spin-excitation spectra in the low-temperature normal state using a magnetic field to eliminate superconductivity (Dai *et al.*, 1999; Woo *et al.*, 2006; Dahm *et al.*, 2009). This makes the estimation of the lowering of the magnetic exchange energy in the low-temperature state ambiguous (Demler and Zhang, 1998; Scalapino and White, 1998). Since heavy fermion superconductors generally have a much smaller energy scale, one can easily obtain the low-temperature normal state spin-excitation spectra using a magnetic field to suppress superconductivity. Figure 41(a) shows the energy dependence of the spin-excitation spectra in the low-temperature normal and superconducting states for $CeCu_2Si_2$ (Stockert *et al.*, 2011), which exhibits superconductivity below $T_c \approx 0.6$ K (Steglich *et al.*, 1979). One can see the opening of a spin gap and clear enhancement in spin excitations above the gap. Using the energy dependence of the dynamic susceptibility in absolute units in the low-temperature normal and superconducting states [Fig. 41(b)], Stockert *et al.* (2011) estimated the lowering of the magnetic exchange energy in $CeCu_2Si_2$

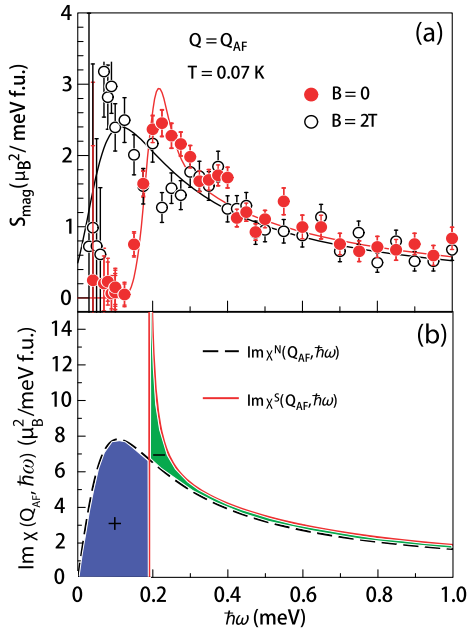

FIG. 41 (color online). Superconductivity-induced changes in spin dynamic susceptibility and magnetic contribution to the superconducting condensation energy in $CeCu_2Si_2$. (a) Energy scans in S-type $CeCu_2Si_2$ at $\mathbf{Q} = \mathbf{Q}_{AF} = (0.215, 0.215, 1.458)$ in the superconducting state at zero field and normal state at $B = 2$ T ($T = 0.07$ K). (b) Imaginary part of the dynamic susceptibility at $\mathbf{Q}_{AF}$ in the normal $[\chi''_N(\mathbf{Q}_{AF}, \hbar\omega)]$ and superconducting $[\chi''_S(\mathbf{Q}_{AF}, \hbar\omega)]$ states. The shaded area marked with a $+$ leads to an increase in magnetic exchange energy ΔE_x, whereas the area marked with a $-$ leads to a decrease in ΔE_x. From Stockert *et al.*, 2011.

and found it to be considerably larger than the superconducting condensation energy. Although the lowering of the magnetic exchange energy is also found to be much larger than the superconducting condensation energy in the superconducting iron pnictides (M. Wang *et al.*, 2013) and chalcogenides (Leiner *et al.*, 2014), these experiments also suffer the problem of not being able to determine the overall spin-excitation spectrum in the low-temperature normal state.

IV. THEORETICAL CONSIDERATIONS

Shortly after the discovery of iron-based superconductors, band structure calculations predicted that the Fermi surfaces of parent compounds would consist of two quasi-two-dimensional near-circular hole pockets centered around the zone center Γ, and two quasi-two-dimensional elliptic electron pockets centered around the (1,0) and (0,1) points in the orthorhombic unfolded Brillouin zone (Fig. 14) (Mazin, 2010; Hirschfeld, Korshunov, and Mazin, 2011). The sign reversed quasiparticle excitations between the hole and electron pockets (nesting) can give rise to the spin-density-wave order observed experimentally (Dong *et al.*, 2008; de la Cruz *et al.*, 2008). In addition, the same quasiparticle excitations in doped superconductors are expected to induce a neutron spin resonance in the superconducting state, which is confirmed by experiments (see Sec. III.B) (Korshunov and Eremin, 2008; Maier and Scalapino, 2008; Maier *et al.*, 2009). Within this weak-coupling analysis, iron-based superconductors and their parents are assumed to be good metals made of itinerant electrons with a spin-density-wave–type AF order. Spin waves and spin excitations can then be calculated using RPA in a multiband Hubbard model with appropriate Fermi surfaces for hole and electron pockets (Knolle and Eremin, 2013). In this approach, the large in-plane effective magnetic exchange coupling anisotropy (Table II) in the spin waves of iron pnictides (Zhao *et al.*, 2009; Harriger *et al.*, 2011) can be understood as due to the ellipticity of the electron pockets (Fig. 14), which induces frustration between the (1,0) and (0,1) wave vectors connecting the hole and electron pockets (Kaneshita and Tohyama, 2010; Knolle *et al.*, 2010). In the underdoped regime where the static AF order coexists and competes with superconductivity (Christianson *et al.*, 2009; Pratt *et al.*, 2009; Wang *et al.*, 2010), spin excitations at (1,0) are determined by the presence of the AF order and associated spin waves, while the excitations at wave vector (0,1) are dominated by the superconductivity and formation of the resonance in the single domain sample (Knolle *et al.*, 2011). However, since most neutron scattering experiments in underdoped iron pnictides were carried out on twinned samples that cannot distinguish the wave vector (1,0) from (0,1) (Christianson *et al.*, 2009; Pratt *et al.*, 2009; Wang *et al.*, 2010), it is unclear how the resonance associated with superconductivity interacts with itinerant electrons contributing to the spin waves. In a systematic study of spin excitations in $BaFe_{2-x}Ni_xAs_2$, the electron-doping evolution of the low-energy spin excitations was found to qualitatively agree with RPA calculations of the nested Fermi surfaces (Luo *et al.*, 2012). However, the high-energy spin excitations are weakly electron-doping independent, and have values much different from that found by RPA calculations (Liu *et al.*, 2012; Luo, Lu *et al.*, 2013; M. Wang *et al.*, 2013). These results suggest that the weak-coupling analysis based on purely itinerant electrons is insufficient to explain the entire spin-excitation spectrum and its electron- or hole-doping evolution.

Although the weak-coupling approach using a Fermi surface nesting picture provides a nice framework to understand static AF order, spin excitations, and their connection with superconductivity in iron-based materials (Mazin, 2010; Hirschfeld, Korshunov, and Mazin, 2011), calculations show that the ordered moment in the AF iron pnictides is around 2 μ_B/Fe (Ma and Lu, 2008), much larger than the largest experimental value (~0.9 μ_B/Fe, see Table I). Furthermore, the ordering wave vectors of the bicollinear AF structure in iron chalcogenides shown in Fig. 2(c) do not match the nesting wave vectors of the Fermi surfaces (Subedi *et al.*, 2008). In the strong-coupling limit, all unpaired electrons, not just itinerant electrons near the Fermi surface, participate in forming magnetic order, much like the magnetic moment of Cu^{2+} in the insulating copper oxides (Fang *et al.*, 2008; Si and Abrahams, 2008; Xu, Müller, and Sachdev, 2008). Here the AF ordered state of iron-based superconductors can be described by a local-moment Heisenberg Hamiltonian with the nearest neighbors (J_{1a}-J_{1b}) and next nearest neighbor (J_2) exchange interactions (Fig. 4) (Fang *et al.*, 2008; Xu, Müller, and Sachdev, 2008; Yildirim, 2008; Dai *et al.*, 2009; Han *et al.*, 2009; Moreo *et al.*, 2009; Yu *et al.*, 2013). In this picture, the large in-plane magnetic exchange coupling

anisotropy in the parent compounds of iron pnictides is understood in terms of the presence of the biquadratic exchange coupling K between the nearest spins in the AF ordered states, which can be mapped onto the J_{1a}-J_{1b} model with a specific relationship between J_{1a}-J_{1b} and J_1-K (Wysocki, Belashchenko, and Antropov, 2011; Yu *et al.*, 2012). This means that the usual local-moment Heisenberg Hamiltonian will be modified to $H = J_1 \sum_{i,\delta} \mathbf{S}_i \cdot \mathbf{S}_{i,\delta} + J_2 \sum_{i,\delta} \mathbf{S}_i \cdot \mathbf{S}_{i+\delta} - K \sum_{i,\delta} (\mathbf{S}_i \cdot \mathbf{S}_{i,\delta})^2$, where J_1 and J_2 are the nearest and next nearest neighbor exchange couplings, respectively, and $\mathbf{S}_i$ is the spin at site i (Wysocki, Belashchenko, and Antropov, 2011; Yu *et al.*, 2012). The calculated dynamical structure factor $S(\mathbf{Q}, \omega)$ forms ellipses in momentum space around $\mathbf{Q}_{\mathrm{AF}} = (\pm 1, 0)$ at low excitation energies. With increasing energy, the elliptic features expand toward the zone boundary and gradually split into two parts, forming a pattern around the wave vector $(\pm 1, \pm 1)$ consistent with neutron scattering experiments (Zhao *et al.*, 2009; Harriger *et al.*, 2011; Wysocki, Belashchenko, and Antropov, 2011; Yu *et al.*, 2012).

By comparing the AF exchange interactions determined from neutron scattering in the parent compounds of iron-based superconductors with those of the superconducting gap functions in the corresponding superconducting materials observed by ARPES, it was argued that the key ingredients in determining the high-T_c superconductivity of iron-based materials are the next nearest neighbor local AF exchange interactions in real space and a Fermi surface topology in reciprocal space that matches the pairing form factor provided by AF interactions (Hu and Ding, 2012). From the analysis of spin-excitation spectra in hole- and electron-doped iron pnictides and magnetic contributions to the superconducting condensation energy (Scalapino, 2012), we find that high-T_c superconductivity is associated with materials having large magnetic exchange couplings and strong itinerant electron-spin-excitation interactions (M. Wang *et al.*, 2013), similar to the large Debye temperatures and strong electron-phonon interactions in high-T_c BCS superconductors (Bardeen, Cooper, and Schrieffer, 1957). Finally, the strong-coupling approach predicts the presence of a quantum critical point separating a paramagnetic metallic phase from an AF phase in phosphorus doped iron pnictides (Dai *et al.*, 2009). Indeed, neutron scattering experiments on powder samples of $CeFeAs_{1-x}P_xO$ suggest the presence of a quantum critical point near $x = 0.4$ controlled by the pnictogen height away from the Fe plane [Fig. 7(a)] (de la Cruz *et al.*, 2010). Similarly, thermodynamic and transport measurements on $BaFe_2(As_{1-x}P_x)_2$ identified a quantum critical point near optimal superconductivity at $x = 0.3$ [Fig. 6(d)] (Shibauchi, Carrington, and Matsuda, 2014). However, recent neutron powder diffraction measurements on $BaFe_2(As_{1-x}P_x)_2$ suggest that structural quantum criticality cannot exist at compositions higher than $x = 0.28$ due to the actual phase stability range (Allred *et al.*, 2014). It is therefore desirable to carry out neutron scattering and μSR experiments on single crystals of $BaFe_2(As_{1-x}P_x)_2$ near $x = 0.3$ to establish the nature of the AF phase transition with increasing P doping. Recent NMR, neutron, and x-ray diffraction experiments indicate that the AF order in $BaFe_2(As_{1-x}P_x)_2$ indeed vanishes in the weakly first order fashion as a function of increasing P doping near $x = 0.3$ (Hu *et al.*, 2015).

While there are many phenomenological reasons for using the strong-coupling approach to understand the electrical transport, spin and charge dynamical properties of iron pnictides and chalcogenides (Fang *et al.*, 2008; Xu, Müller, and Sachdev, 2008; Yildirim, 2008; Dai *et al.*, 2009; Yu *et al.*, 2013), such an approach is incompatible with some spin dynamical properties. For example, in a strict local-moment Heisenberg Hamiltonian, single particle excitations or spin waves should have only transverse components and do not support longitudinal spin excitations in the AF ordered phase of iron pnictides as seen in polarized neutron scattering experiments [Fig. 29(f)] (C. Wang *et al.*, 2013). Furthermore, the electron- and hole-doping evolution of the low-energy spin excitations are consistent with the Fermi surface nesting predictions, but it is unclear whether the data are also compatible with a pure local-moment Heisenberg Hamiltonian (see Sec. III.C). Finally, spin waves of iron chalcogenides are heavily damped at high energies near the zone boundary and exhibit a number of anomalous properties difficult to understand within a local-moment model (Lipscombe *et al.*, 2011; Zaliznyak *et al.*, 2011).

Instead of a strong- or weak-coupling approach, the iron pnictides may be Hund's metals, where the interaction between the electrons is not strong enough to fully localize them to form a Mott insulator, but is sufficient so that the low-energy quasiparticles have much enhanced mass (Haule and Kotliar, 2009). Here the electron correlation strength would be primarily controlled by the Hund's coupling J_H, which depends on the pnictogen heights and tends to align spins of all the electrons on a given Fe atom, and hence enhances spin excitations without appreciably affecting the charge excitations (Yin, Haule, and Kotliar, 2011). This is different from the effect of large Coulomb repulsion U in a Mott insulator, which hampers charge excitations in order to enhance spin fluctuations (Lee, Nagaosa, and Wen, 2006). The electronic excitations in iron-based superconductors are neither fully itinerant nor fully localized, but have a dual nature that can be realistically described by a combination of DFT and DMFT (Kotliar *et al.*, 2006). This idea is similar to the picture where single electron spectral function is composed of coherent and incoherent parts representing electrons near (itinerant electrons) and far away (local moments) from the Fermi surface (Abrahams and Si, 2011).

Using the combined DFT and DMFT method, one can estimate the size of the ordered moment for different iron pnictides and find them to be close to the observed value (Yin, Haule, and Kotliar, 2011). The same method has also been used to calculate the spin-wave spectra in $BaFe_2As_2$ and good agreement was found with neutron scattering experiments (Park, Haule, and Kotliar, 2011; Yin, Haule, and Kotliar, 2014). Finally, the combined DFT and DMFT method has been used to calculate the electron- and hole-doping dependence of the spin-excitation spectrum in absolute units for $Ba_{1-x}K_xFe_2As_2$ and $BaFe_{2-x}Ni_xAs_2$ (M. Wang *et al.*, 2013). Compared with RPA calculations based on the weak-coupling approach (Hirschfeld, Korshunov, and Mazin, 2011), combining DFT and DMFT gives a more realistic estimation of the absolute intensity of the local dynamic susceptibility and can

quantitatively model the electron- and hole-doping evolution of the spin excitations in absolute units (M. Wang *et al.*, 2013). Furthermore, it can account for the pnictogen height dependence of the spin-wave spectra (Zhang *et al.*, 2014a).

The static AF order and spin excitations in iron-based materials can also be understood by hybrid models consisting of local moments on each Fe site and itinerant electrons from the degenerate d_{xz} and d_{yz} orbitals (Kou, Li, and Weng, 2009; Yin, Lee, and Ku, 2010). In this picture, the local moments interact with each other via J_1 and J_2 Heisenberg exchanges, and they are coupled to the itinerant electrons via Hunds rule coupling. Since itinerant electrons are associated only with d_{xz} and d_{yz} orbitals that break the C_4 rotational symmetry of the underlying x-y lattice plane due to their different occupancies, these orbitals can form a Hamiltonian that drives the in-plane magnetic anisotropy, producing unfrustrated collinear AF order and lifting the degeneracy of the (1,0) and (0,1) magnetic states (Kou, Li, and Weng, 2009; Krüger *et al.*, 2009; Lee, Yin, and Ku, 2009; C.-C. Chen *et al.*, 2010; Lv, Krüger, and Phillips, 2010; Yin, Lee, and Ku, 2010). Here the magnetic anisotropy is due to purely electronic ferro-orbital order that spontaneously breaks the rotational symmetry of the underlying lattice and drives the observed magnetic and structural transitions without Fermi surface nesting or magnetic frustration (Krüger *et al.*, 2009; Lee, Yin, and Ku, 2009). Using a fermionic representation of the local moments and a generalized RPA framework, one can calculate the spin-wave spectra of $BaFe_2As_2$ and find that the outcome is consistent with spin excitations in the AF ordered and paramagnetic states obtained from inelastic neutron scattering (Yang, Kou, and Weng, 2010; Leong *et al.*, 2014). In addition, the global phase diagram for the AF and superconducting states calculated from the hybrid model on the mean-field level is qualitatively consistent with experiments (You *et al.*, 2011). At high characteristic temperatures, electrons in more localized orbitals of the multiband system may first form short-ranged AF order. Upon cooling to lower temperatures, the electrons in more itinerant orbitals can be driven into a true static AF ordered or superconducting state via Hund's coupling to the preformed localized AF state. This is analogous to the orbital-selective Mott transition, where itinerant and localized electrons in different orbitals may separate as independent degrees of freedom (Kou, Li, and Weng, 2009; Lv, Krüger, and Phillips, 2010; Yang, Kou, and Weng, 2010; You *et al.*, 2011; Leong *et al.*, 2014).

V. SUMMARY AND OUTLOOK

In this paper, we reviewed the recent progress of neutron scattering studies of the static AF order and spin dynamics in iron-based high temperature superconductors. Soon after the discovery of these materials in 2008 (Kamihara *et al.*, 2008), neutron diffraction measurements at the NIST Center for Neutron Research and High Flux Isotope Reactor at Oak Ridge National Laboratory determined the AF order and crystalline structures of the parent and superconducting compounds (Huang, Qiu *et al.*, 2008; de la Cruz *et al.*, 2008). These measurements established the basis that superconductivity in iron-based materials arises from the suppression of static long-range ordered antiferromagnets, much like copper oxide superconductors (Tranquada, Xu, and Zaliznyak, 2014). When single crystals of the 122 family of iron pnictides and iron chalcogenides became available, the advanced time-of-flight neutron spectrometers at spallation neutron sources at Oak Ridge National Laboratory and ISIS at Rutherford-Appleton Laboratory allowed detailed mapping of the spin-wave spectra throughout the Brillouin zone (Diallo *et al.*, 2009; Zhao *et al.*, 2009). This first occurred only slightly more than one year after the discovery of the iron pnictide superconductors. In copper oxide superconductors (Bednorz and Müller, 1986), the first complete spin-wave spectrum was measured 15 years after its discovery (Coldea *et al.*, 2001). Using the overall spin-wave spectra in the AF ordered iron pnictides, one can fit the dispersion curves with a Heisenberg Hamiltonian, revealing the anisotropic in-plane effective magnetic exchange couplings. This has inspired much discussion on the microscopic origin of the effective magnetic anisotropy as described in Sec. IV.

Since high-quality single crystals of electron- and hole-doped $BaFe_2As_2$ are available, most of the elastic and inelastic neutron scattering experiments have been carried out on these materials. With elastic neutron scattering experiments, one can map out the electron- and hole-doping evolution of the structural and magnetic phase diagrams. For electron-doped materials obtained via Co and Ni substitution of Fe, the tetragonal-to-orthorhombic lattice distortion precedes the AF phase transition, and the static long-range order coexists and/or competes with superconductivity in the underdoped regime. However, the AF order becomes incommensurate with a short-range correlation length near optimal superconductivity, indicating that it is a spin-glass phase in the matrix of the superconducting phase, coexisting and competing with superconductivity (Bernhard *et al.*, 2012; Dioguardi *et al.*, 2013; Lu *et al.*, 2014). NMR measurements on the 1111 family of materials also suggest nanoscale electronic inhomogeneity (Lang *et al.*, 2010). For hole-doped $Ba_{1-x}K_xFe_2As_2$ and $Ba_{1-x}Na_xFe_2As_2$, the structural and magnetic phase transitions are coupled at all doping levels (Avci *et al.*, 2012, 2013, 2014). Near optimal superconductivity, there is a new magnetic phase within the tetragonal structure, possibly associated with a spin nematic phase, and the transition from AF order to superconductivity may also occur in the first order fashion (Avci *et al.*, 2013, 2014). Finally, although transport and NMR measurements suggest the presence of a quantum critical point near $x = 0.3$ for isoelectronically doped $BaFe_2(As_{1-x}P_x)_2$ (Shibauchi, Carrington, and Matsuda, 2014), neutron diffraction measurements have mapped out only the magnetic and structural phase diagram in the underdoped regime (Allred *et al.*, 2014), and the evolution of AF order near optimal superconductivity vanishes in the weakly first order fashion (Hu *et al.*, 2015).

Similar to neutron diffraction work, most of the inelastic neutron scattering studies of spin excitations in iron pnictides have been focused on electron-doped $BaFe_2As_2$. Compared with the undoped parent compounds, electron doping appears to modify spin excitations below ~80 meV while leaving high-energy spin excitations mostly unchanged (Luo, Lu *et al.*, 2013). However, hole doping suppresses high-energy spin excitations and transfers the spectral weight to low

energies (M. Wang *et al.*, 2013). In addition, the wave vector dependence of the low-energy spin excitations in iron pnictides appears to be controlled by the quasiparticle nesting between the hole and electron Fermi surfaces. These results are consistent with the notion that spin excitations in iron pnictides have both local and itinerant character with the electron correlations controlled by the pnictogen height and strength of the Hund's coupling (Haule and Kotliar, 2009; Kou, Li, and Weng, 2009; Yin, Lee, and Ku, 2010). The availability of large single crystals of iron chalcogenides $Fe_{1+y}Te_{1-x}Se_x$ means that spin excitations in these materials have been carefully mapped out (Lumsden *et al.*, 2010; Lipscombe *et al.*, 2011; Zaliznyak *et al.*, 2011). In particular, application of the sum rules of neutron scattering indicate that the integrated spin-excitation intensity of $Fe_{1+x}Te$ is inconsistent with an $S = 1$ Fe^{2+} ground state expected in the presence of a strong crystalline electric field (Stock *et al.*, 2014), suggesting the importance of itinerant electrons even for the iron chalcogenides, which exhibit strong electron correlations and localized moments (Yin, Haule, and Kotliar, 2011).

Compared with electron-doped $BaFe_2As_2$, spin excitations in hole-doped $Ba_{1-x}K_xFe_2As_2$ and isoelectronically doped $BaFe_2As_{2-x}P_x$ iron pnictides are much less studied (C. H. Lee *et al.*, 2011, 2013; C. L. Zhang *et al.*, 2011; M. Wang *et al.*, 2013). Given the recent discovery of the possible spin nematic phase in the tetragonal phase (Avci *et al.*, 2014), it will be interesting to study the evolution of the overall spin excitations in hole and isoelectronically doped iron pnictides. In particular, since the electron pairing symmetry of the heavily hole-doped superconducting $Ba_{1-x}K_xFe_2As_2$ is still unclear (Tafti *et al.*, 2013; Ota *et al.*, 2014), it is important to carry out temperature dependent measurements to study the effect of superconductivity on low-energy spin excitations. A determination of the wave vector and energy of the superconductivity-induced neutron spin resonance will put considerable constraint on the nature of the superconducting pairing state.

Although most neutron scattering work has focused on the 122 family of iron pnictides and iron chalcogenides, the 111 family, including Co-doped NaFeAs and LiFeAs, is equally interesting since these materials may be more correlated than the 122 family (Yin, Haule, and Kotliar, 2011). At present, spin waves throughout the Brillouin zone have been mapped out for NaFeAs (Zhang *et al.*, 2014a). It is important to determine how electron doping affects the spin excitations and to compare the outcome with the pure LiFeAs and Co-doped LiFeAs. Similarly, it is important to study temperature and doping-dependent spin excitations in Se-overdoped $Fe_{1+y}Te_{1-x}Se_x$ and pure FeSe. The case of pure FeSe is particularly interesting as this is the system where the structural phase transition happens without static AF order (Johnston, 2010; Stewart, 2011). A complete understanding of this material may reveal a spin or orbital driven electronic nematic phase. Detailed experiments on other iron-based superconductors and associated materials are necessary to establish the common features of the magnetism in various materials and their connection to high-T_c superconductivity. Neutron scattering, together with RIXS, μSR, and NMR, can play a unique role in our quest to find the microscopic origin of high-T_c superconductivity.

ACKNOWLEDGMENTS

P. D. expresses sincere appreciation to Xingye Lu and Yu Song for preparing the figures for this manuscript. I am also in debt to David Tam, Yu Song, and Qimiao Si for a critical reading of the manuscript. The former and current graduate students and postdocs in my group, including Shiliang Li, Clarina de la Cruz, Jun Zhao, Songxue Chi, Oliver Lipscombe, Leland Harriger, Miaoyin Wang, Mengshu Liu, Meng Wang, Xingye Lu, Huiqiang Luo, Chenglin Zhang, Scott Carr, and Yu Song, have played a key role in obtaining the neutron scattering results reported here. They continue to educate me on the interesting physics in iron-based superconductors. I am in debt to my colleagues G. F. Chen, Elbio Dagotto, Takeshi Egami, DongLai Feng, Kristjan Haule, Stephen Hayden, Jiangping Hu, Gabriel Kotliar, Jeff Lynn, Thomas Maier, Herb Mook, Andriy H. Nevidomskyy, Toby Perring, L.-P. Regnault, Qimiao Si, Yixi Su, Tomo Uemura, Nanlin Wang, Zhiping Yin, and Rong Yu for fruitful collaborations. I also thank Xianhui Chen, Hong Ding, M. H. Fang, D.-H. Lee, Tao Xiang, Haihu Wen, Z. Y. Weng, X. J. Zhou, and friends in the Beijing Forum for high-T_c superconductivity for many helpful discussions over the years. The materials synthesis and neutron scattering efforts on the hole-doped 122 and 111 family of materials are supported by the U.S. DOE, Office of Basic Energy Sciences, under Contract No. DE-SC0012311. The neutron scattering work on the electron-doped 122 family of materials is supported by U.S. NSF, No. DMR-1362219. The combination of RPA calculation and neutron scattering is supported by the U.S. NSF, No. DMR-143606 and No. DMR-1308603. Part of the materials work at Rice University is supported by the Robert A. Welch Foundation Grant No. C-1839.

REFERENCES

Abrahams, E., and Q. Si, 2011, J. Phys. Condens. Matter **23**, 223201.
Allan, M. P., *et al.*, 2013, Nat. Phys. **9**, 220.
Alloul, H., J. Bobroff, M. Gabay, and P. J. Hirschfeld, 2009, Rev. Mod. Phys. **81**, 45.
Allred, J. M., *et al.*, 2014, Phys. Rev. B **90**, 104513.
Ament, L. J. P., M. van Veenendaal, T. P. Devereaux, J. P. Hill, and J. van den Brink, 2011, Rev. Mod. Phys. **83**, 705.
Argyriou, D. N., *et al.*, 2010, Phys. Rev. B **81**, 220503.
Armitage, N. P., P. Fournier, and R. L. Greene, 2010, Rev. Mod. Phys. **82**, 2421.
Aswathy, P. M., J. B. Anooja, P. M. Sarun, and U. Syamaprasad, 2010, Supercond. Sci. Technol. **23**, 073001.
Avci, S., *et al.*, 2011, Phys. Rev. B **83**, 172503.
Avci, S., *et al.*, 2012, Phys. Rev. B **85**, 184507.
Avci, S., *et al.*, 2013, Phys. Rev. B **88**, 094510.
Avci, S., *et al.*, 2014, Nat. Commun. **5**, 3845.
Babkevich, P., M. Bendele, A. T. Boothroyd, K. Conder, S. N. Gvasaliya, R. Khasanov, E. Pomjakushina, and B. Roessli, 2010, J. Phys. Condens. Matter **22**, 142202.
Babkevich, P., B. Roessli, S. N. Gvasaliya, L.-P. Regnault, P. G. Freeman, E. Pomjakushina, K. Conder, and A. T. Boothroyd, 2011, Phys. Rev. B **83**, 180506(R).
Balatsky, A. V., I. Vekhter, and J. X. Zhu, 2006, Rev. Mod. Phys. **78**, 373.

Bao, W., Q. Z. Huang, G. F. Chen, M. A. Green, D. M. Wang, J. B. He, and Y. M. Qiu, 2011, Chin. Phys. Lett. **28**, 086104.
Bao, W., *et al.*, 2009, Phys. Rev. Lett. **102**, 247001.
Bardeen, J., L. N. Cooper, and J. R. Schrieffer, 1957, Phys. Rev. **108**, 1175.
Bednorz, J. G., and K. A. Müller, 1986, Z. Phys. B **64**, 189.
Bernhard, C., *et al.*, 2012, Phys. Rev. B **86**, 184509.
Boothroyd, A. T., P. Babkevich, D. Prabhakaran, and P. G. Freeman, 2011, Nature (London) **471**, 341.
Borisenko, S. V., *et al.*, 2010, Phys. Rev. Lett. **105**, 067002.
Brand, J., A. Stunault, S. Wurmehl, L. Harnagea, B. Bruchner, M. Meven, and M. Braden, 2014, Phys. Rev. B **89**, 045141.
Brown, P. J., T. Chatterji, A. Stunault, Y. Su, Y. Xiao, R. Mittal, T. Brückel, T. Wolf, and P. Adelmann, 2010, Phys. Rev. B **82**, 024421.
Brydon, P. M. R., M. Daghofer, C. Timm, and J. van den Brink, 2011, Phys. Rev. B **83**, 060501(R).
Burrard-Lucas, M., *et al.*, 2013, Nat. Mater. **12**, 15.
Canfield, P. C., and S. L. Bud'ko, 2010, Annu. Rev. Condens. Matter Phys. **1**, 27.
Carr, S. V., D. Louca, J. Siewenie, Q. Huang, A. F. Wang, X. H. Chen, and P. C. Dai, 2014, Phys. Rev. B **89**, 134509.
Carretta, P., R. D. Renzi, G. Prando, and S. Sanna, 2013, Phys. Scr. **88**, 068504.
Castellan, J.-P., *et al.*, 2011, Phys. Rev. Lett. **107**, 177003.
Charnukha, A., *et al.*, 2012, Phys. Rev. Lett. **109**, 017003.
Chen, C.-C., J. Maciejko, A. P. Sorini, B. Moritz, R. R. P. Singh, and T. P. Devereaux, 2010, Phys. Rev. B **82**, 100504.
Chen, F., *et al.*, 2010, Phys. Rev. B **81**, 014526.
Chen, X. H., P. C. Dai, D. L. Feng, T. Xiang, and F.-C. Zhang, 2014, Natl. Sci. Rev. **1**, 371.
Chen, Y., J. W. Lynn, J. Li, G. Li, G. F. Chen, J. L. Luo, N. L. Wang, P. C. Dai, C. de la Cruz, and H. A. Mook, 2008, Phys. Rev. B **78**, 064515.
Chi, S. X., J. A. Rodriguez-Rivera, J. W. Lynn, C. L. Zhang, D. Phelan, D. K. Singh, R. Paul, and P. C. Dai, 2011, Phys. Rev. B **84**, 214407.
Chi, S. X., F. Ye, W. Bao, M. H. Fang, H. D. Wang, C. H. Dong, A. T. Savici, G. E. Granroth, M. B. Stone, and R. S. Fishman, 2013, Phys. Rev. B **87**, 100501.
Chi, S. X., *et al.*, 2009, Phys. Rev. Lett. **102**, 107006.
Christianson, A. D., M. D. Lumsden, S. E. Nagler, G. J. MacDougall, M. A. McGuire, A. S. Sefat, R. Jin, B. C. Sales, and D. Mandrus, 2009, Phys. Rev. Lett. **103**, 087002.
Christianson, A. D., *et al.*, 2008, Nature (London) **456**, 930.
Chu, J. H., J. G. Analytis, K. D. Greve, P. L. McMahon, Z. Islam, Y. Yamamoto, and I. R. Fisher, 2010, Science **329**, 824.
Chu, J.-H., J. G. Analytis, C. Kucharczyk, and I. R. Fisher, 2009, Phys. Rev. B **79**, 014506.
Chubukov, A. V., 2012, Annu. Rev. Condens. Matter Phys. **3**, 57.
Coldea, R., S. M. Hayden, G. Aeppli, T. G. Perring, C. D. Frost, T. E. Mason, S.-W. Cheong, and Z. Fisk, 2001, Phys. Rev. Lett. **86**, 5377.
Dagotto, E., 2013, Rev. Mod. Phys. **85**, 849.
Dahm, T., V. Hinkov, S. V. Borisenko, A. A. Kordyuk, V. B. Zabolotnyy, J. Fink, B. Büchner, D. J. Scalapino, W. Hanke, and B. Keimer, 2009, Nat. Phys. **5**, 217.
Dai, J., Q. Si, J. X. Zhu, and E. Abrahams, 2009, Proc. Natl. Acad. Sci. U.S.A. **106**, 4118.
Dai, P. C., J. P. Hu, and E. Dagotto, 2012, Nat. Phys. **8**, 709.
Dai, P. C., H. A. Mook, G. Aeppli, S. M. Hayden, and F. Doğan, 2000, Nature (London) **406**, 965.
Dai, P. C., H. A. Mook, S. M. Hayden, G. Aeppli, T. G. Perring, R. D. Hunt, and F. Doğan, 1999, Science **284**, 1344.
Das, P., S.-Z. Lin, N. J. Ghimire, K. Huang, F. Ronning, E. D. Bauer, J. D. Thompson, C. D. Batista, G. Ehlers, and M. Janoschek, 2014, Phys. Rev. Lett. **113**, 246403.
Das, T., and A. V. Balatsky, 2011, Phys. Rev. B **84**, 014521.
de la Cruz, C., *et al.*, 2008, Nature (London) **453**, 899.
de la Cruz, C., *et al.*, 2010, Phys. Rev. Lett. **104**, 017204.
Demler, E., and S. C. Zhang, 1998, Nature (London) **396**, 733.
Dhital, C., T. Hogan, Z. Yamani, R. J. Birgeneau, W. Tian, M. Matsuda, A. S. Sefat, Z. Q. Wang, and S. D. Wilson, 2014, Phys. Rev. B **89**, 214404.
Dhital, C., Z. Yamani, W. Tian, J. Zeretsky, A. S. Sefat, Z. Q. Wang, R. J. Birgeneau, and S. D. Wilson, 2012, Phys. Rev. Lett. **108**, 087001.
Diallo, S. O., *et al.*, 2009, Phys. Rev. Lett. **102**, 187206.
Dioguardi, A. P., *et al.*, 2013, Phys. Rev. Lett. **111**, 207201.
Dong, J., *et al.*, 2008, Europhys. Lett. **83**, 27006.
Duffy, J. A., S. M. Hayden, Y. Maeno, Z. Mao, J. Kulda, and G. J. McIntyre, 2000, Phys. Rev. Lett. **85**, 5412.
Eschrig, M., 2006, Adv. Phys. **55**, 47.
Ewings, R. A., T. G. Perring, J. Gillett, S. D. Das, S. E. Sebastian, A. E. Taylor, T. Guidi, and A. T. Boothroyd, 2011, Phys. Rev. B **83**, 214519.
Fang, C., H. Yao, W.-F. Tsai, J. P. Hu, and S. A. Kivelson, 2008, Phys. Rev. B **77**, 224509.
Fang, M. H., H. D. Wang, C. Dong, Z. J. Li, C.-M. Feng, J. Chen, and H. Q. Yuan, 2011, Europhys. Lett. **94**, 27009.
Fawcett, E., H. L. Alberts, V. Y. Galkin, D. R. Noakes, and J. V. Yakhmi, 1994, Rev. Mod. Phys. **66**, 25.
Fernandes, R. M., A. V. Chubukov, and J. Schmalian, 2014, Nat. Phys. **10**, 97.
Fernandes, R. M., L. H. VanBebber, P. C. S. Bhattacharya, D. M. V. Keppens, M. A. McGuire, B. C. Sales, A. S. Sefat, and J. Schmalian, 2010, Phys. Rev. Lett. **105**, 157003.
Fink, J., *et al.*, 2009, Phys. Rev. B **79**, 155118.
Fisher, I. R., L. Degiorgi, and Z. X. Shen, 2011, Rep. Prog. Phys. **74**, 124506.
Fradkin, E., and S. A. Kivelson, 2012, Nat. Phys. **8**, 864.
Friemel, G., W. P. Liu, E. A. Goremychkin, Y. Liu, J. T. Park, O. Sobolev, C. T. Lin, B. Keimer, and D. S. Inosov, 2012, Europhys. Lett. **99**, 67004.
Friemel, G., *et al.*, 2012, Phys. Rev. B **85**, 140511(R).
Fruchart, D., P. Convert, P. Wolfers, R. Madar, J. P. Senateur, and R. Fruchart, 1975, Mater. Res. Bull. **10**, 169.
Fu, M., D. A. Torchetti, T. Imai, F. L. Ning, J.-Q. Yan, and A. S. Sefat, 2012, Phys. Rev. Lett. **109**, 247001.
Fujita, M., H. Hiraka, M. Matsuda, M. Matsuura, J. M. Tranquada, S. Wakimoto, G. Xu, and K. Yamada, 2012, J. Phys. Soc. Jpn. **81**, 011007.
Fujita, M., M. Matsuda, B. Fåk, C. D. Frost, and K. Yamada, 2006, J. Phys. Soc. Jpn. **75**, 093704.
Ge, Q. Q., Z. R. Ye, M. Xu, Y. Zhang, J. Jiang, B. P. Xie, Y. Song, C. L. Zhang, P. C. Dai, and D. L. Feng, 2013, Phys. Rev. X **3**, 011020.
Gegenwart, P., Q. Si, and F. Steglich, 2008, Nat. Phys. **4**, 186.
Ghiringhelli, G., *et al.*, 2012, Science **337**, 821.
Goldman, A. I., D. N. Argyriou, B. Ouladdiaf, T. Chatterji, A. Kreyssig, S. Nandi, N. Ni, S. L. Bud'ko, P. C. Canfield, and R. J. McQueeney, 2008, Phys. Rev. B **78**, 100506(R).
Goldman, A. I., *et al.*, 2009, Phys. Rev. B **79**, 024513.
Graser, S., A. F. Kemper, T. A. Maier, H.-P. Cheng, P. J. Hirschfeld, and D. J. Scalapino, 2010, Phys. Rev. B **81**, 214503.
Gretarsson, H., S. R. Saha, T. Drye, J. Paglione, J. H. Kim, D. Casa, T. Gog, W. Wu, S. R. Julian, and Y.-J. Kim, 2013, Phys. Rev. Lett. **110**, 047003.

Gretarsson, H., *et al.*, 2011, Phys. Rev. B **84**, 100509(R).
Guo, J. G., S. F. Jin, G. Wang, S. C. Wang, K. H. Zhu, T. T. Zhou, M. He, and X. L. Chen, 2010, Phys. Rev. B **82**, 180520(R).
Hamilton, W. C., 1957, Acta Crystallogr. **10**, 629.
Han, M. J., Q. Yin, W. E. Pickett, and S. Y. Savrasov, 2009, Phys. Rev. Lett. **102**, 107003.
Harriger, L. W., O. J. Lipscombe, C. L. Zhang, H. Q. Luo, M. Wang, K. Marty, M. D. Lumsden, and P. C. Dai, 2012, Phys. Rev. B **85**, 054511.
Harriger, L. W., H. Q. Luo, M. S. Liu, T. G. Perring, C. Frost, J. P. Hu, M. R. Norman, and P. C. Dai, 2011, Phys. Rev. B **84**, 054544.
Haule, K., and G. Kotliar, 2009, New J. Phys. **11**, 025021.
Haule, K., J. H. Shim, and G. Kotliar, 2008, Phys. Rev. Lett. **100**, 226402.
Headings, N. S., S. M. Hayden, R. Coldea, and T. G. Perring, 2010, Phys. Rev. Lett. **105**, 247001.
Hiraishi, M., *et al.*, 2014, Nat. Phys. **10**, 300.
Hirschfeld, P. J., M. M. Korshunov, and I. I. Mazin, 2011, Rep. Prog. Phys. **74**, 124508.
Hsu, F. C., *et al.*, 2008, Proc. Natl. Acad. Sci. U.S.A. **105**, 14262.
Hu, D., *et al.*, 2015, Phys. Rev. Lett. **114**, 157002.
Hu, J. P., and H. Ding, 2012, Sci. Rep. **2**, 381.
Hu, J. P., B. Xu, W. M. Liu, N. N. Hao, and Y. P. Wang, 2012, Phys. Rev. B **85**, 144403.
Huang, Q., Y. Qiu, W. Bao, M. A. Green, J. W. Lynn, Y. C. Gasparovic, T. Wu, G. Wu, and X. H. Chen, 2008, Phys. Rev. Lett. **101**, 257003.
Huang, Q., J. Zhao, J. Lynn, G. Chen, J. Lou, N. Wang, and P. C. Dai, 2008, Phys. Rev. B **78**, 054529.
Hüfner, S., M. A. Hossain, A. Damascelli, and G. A. Sawatzky, 2008, Rep. Prog. Phys. **71**, 062501.
Inosov, D. S., J. T. Park, A. Charnukha, Y. Li, A. V. Boris, B. Keimer, and V. Hinkov, 2011, Phys. Rev. B **83**, 214520.
Inosov, D. S., *et al.*, 2010, Nat. Phys. **6**, 178.
Inosov, D. S., *et al.*, 2013, Phys. Rev. B **87**, 224425.
Ishida, S., *et al.*, 2013, Phys. Rev. Lett. **110**, 207001.
Ishikado, M., *et al.*, 2009, J. Phys. Soc. Jpn. **78**, 043705.
Ishikado, M., *et al.*, 2011, Phys. Rev. B **84**, 144517.
Ismer, J. P., I. Eremin, E. Rossi, and D. K. Morr, 2007, Phys. Rev. Lett. **99**, 047005.
Jayasekara, W., *et al.*, 2013, Phys. Rev. Lett. **111**, 157001.
Jesche, A., *et al.*, 2008, Phys. Rev. B **78**, 180504.
Jiang, S., H. Xing, G. F. Xuan, C. Wang, Z. Ren, C. M. Feng, J. H. Dai, Z.-A. Xu, and G. H. Cao, 2009, J. Phys. Condens. Matter **21**, 382203.
Johnston, D. C., 2010, Adv. Phys. **59**, 803.
Johnston, D. C., R. J. McQueeney, B. Lake, A. Honecker, M. E. Zhitomirsky, R. Nath, Y. Furukawa, V. P. Antropov, and Y. Singh, 2011, Phys. Rev. B **84**, 094445.
Kamihara, Y., H. Hiramatsu, M. Hirano, R. Kawamura, H. Yanagi, T. Kamiya, and H. Hosono, 2006, J. Am. Chem. Soc. **128**, 10012.
Kamihara, Y., T. Watanabe, M. Hirano, and H. Hosono, 2008, J. Am. Chem. Soc. **130**, 3296.
Kaneko, K., A. Hoser, N. Caroca-Canales, A. Jesche, C. Krellner, O. Stockert, and C. Geibel, 2008, Phys. Rev. B **78**, 212502.
Kaneshita, E., and T. Tohyama, 2010, Phys. Rev. B **82**, 094441.
Kastner, M. A., R. J. Birgeneau, G. Shirane, and Y. Endoh, 1998, Rev. Mod. Phys. **70**, 897.
Kim, M. G., *et al.*, 2010, Phys. Rev. B **82**, 220503(R).
Kim, M. G., *et al.*, 2011, Phys. Rev. B **83**, 054514.
Kimber, S. A. J., *et al.*, 2008, Phys. Rev. B **78**, 140503.
Kivelson, S. A., I. P. Bindloss, E. Fradkin, V. Oganesyan, J. M. Tranquada, A. Kapitulnik, and C. Howald, 2003, Rev. Mod. Phys. **75**, 1201.
Knolle, J., and I. Eremin, 2013, *In Iron-based superconductors: materials, properties, and mechanisms*, edited by N.-L. Wang, H. Hosono, and P. C. Dai (Pan Stanfod Publishing Pte, Ltd., Singapore), Chap. 9, p. 431.
Knolle, J., I. Eremin, A. V. Chubukov, and R. Moessner, 2010, Phys. Rev. B **81**, 140506(R).
Knolle, J., I. Eremin, J. Schmalian, and R. Moessner, 2011, Phys. Rev. B **84**, 180510(R).
Korshunov, M. M., and I. Eremin, 2008, Phys. Rev. B **78**, 140509(R).
Kotliar, G., S. Y. Savrasov, K. Haule, V. S. Oudovenko, O. Parcollet, and C. A. Marianetti, 2006, Rev. Mod. Phys. **78**, 865.
Kou, S.-P., T. Li, and Z.-Y. Weng, 2009, Europhys. Lett. **88**, 17010.
Kreyssig, A., *et al.*, 2008, Phys. Rev. B **78**, 184517.
Kreyssig, A., *et al.*, 2010, Phys. Rev. B **81**, 134512.
Krüger, F., S. Kumar, J. Zaanen, and J. van den Brink, 2009, Phys. Rev. B **79**, 054504.
Krzton-Maziopa, A., E. V. Pomjakushina, V. Y. Pomjakushin, F. von Rohr, A. Schilling, and K. Conder, 2012, J. Phys. Condens. Matter **24**, 382202.
Ksenofontov, V., G. Wortmann, S. A. Medvedev, V. Tsurkan, J. Deisenhofer, A. Loidl, and C. Felser, 2011, Phys. Rev. B **84**, 180508.
Kuroki, K., S. Onari, R. Arita, H. Usui, Y. Tanaka, H. Kontani, and H. Aoki, 2008, Phys. Rev. Lett. **101**, 087004.
Lamsal, J., G. S. Tucker, T. W. Heitmann, A. Kreyssig, A. Jesche, A. Pandey, W. Tian, R. J. McQueeney, D. C. Johnston, and A. I. Goldman, 2013, Phys. Rev. B **87**, 144418.
Lang, G., H.-J. Grafe, D. Paar, F. Hammerath, K. Manthey, G. Behr, J. Werner, and B. Büchner, 2010, Phys. Rev. Lett. **104**, 097001.
Lee, C. C., W. G. Yin, and W. Ku, 2009, Phys. Rev. Lett. **103**, 267001.
Lee, C. H., P. Steffens, N. Qureshi, M. Nakajima, K. Kihou, A. Iyo, H. Eisaki, and M. Braden, 2013, Phys. Rev. Lett. **111**, 167002.
Lee, C. H., *et al.*, 2011, Phys. Rev. Lett. **106**, 067003.
Lee, P. A., N. Nagaosa, and X. G. Wen, 2006, Rev. Mod. Phys. **78**, 17.
Lee, S.-H., *et al.*, 2010, Phys. Rev. B **81**, 220502.
Lee, W. S., *et al.*, 2013, arXiv:1308.4740.
Leiner, J., *et al.*, 2014, Phys. Rev. B **90**, 100501(R).
Leliévre-Berna, E., *et al.*, 2005, Physica (Amsterdam) **356B**, 131.
Leong, Z. D., W.-C. Lee, W. Lv, and P. Phillips, 2014, Phys. Rev. B **90**, 125158.
Lester, C., J. H. Chu, J. G. Analytis, T. G. Perring, I. R. Fisher, and S. M. Hayden, 2010, Phys. Rev. B **81**, 064505.
Lester, C., J.-H. Chu, J. G. Analytis, S. C. Capelli, A. S. Erickson, C. L. Condron, M. F. Toney, I. R. Fisher, and S. M. Hayden, 2009, Phys. Rev. B **79**, 144523.
Lester, C., J.-H. Chu, J. G. Analytis, A. Stunault, I. R. Fisher, and S. M. Hayden, 2011, Phys. Rev. B **84**, 134514.
Li, L. J., *et al.*, 2009, New J. Phys. **11**, 025008.
Li, S. L., Y. Chen, S. Chang, J. W. Lynn, L. J. Li, Y. K. Luo, G. H. Cao, Z. A. Xu, and P. C. Dai, 2009, Phys. Rev. B **79**, 174527.
Li, S. L., C. de la Cruz, Q. Huang, G. F. Chen, T.-L. Xia, J. L. Luo, N. L. Wang, and P. C. Dai, 2009, Phys. Rev. B **80**, 020504(R).
Li, S. L., X. Y. Lu, M. Wang, H.-Q. Luo, M. Y. Wang, C. L. Zhang, E. Faulhaber, L. P. Regnault, S. Chang, and P. C. Dai, 2011, Phys. Rev. B **84**, 024518.
Li, S. L., *et al.*, 2009, Phys. Rev. B **79**, 054503.
Li, S. L., *et al.*, 2010, Phys. Rev. Lett. **105**, 157002.

Li, W., *et al.*, 2011, Nat. Phys. **8**, 126.
Lipscombe, O. J., G. F. Chen, C. Fang, T. G. Perring, D. L. Abernathy, A. D. Christianson, T. Egami, N. L. Wang, J. P. Hu, and P. C. Dai, 2011, Phys. Rev. Lett. **106**, 057004.
Lipscombe, O. J., S. M. Hayden, B. Vignolle, D. F. McMorrow, and T. G. Perring, 2007, Phys. Rev. Lett. **99**, 067002.
Lipscombe, O. J., *et al.*, 2010, Phys. Rev. B **82**, 064515.
Liu, M. S., C. Lester, J. Kulda, X. Y. Lu, H. Q. Luo, M. Wang, S. M. Hayden, and P. C. Dai, 2012, Phys. Rev. B **85**, 214516.
Liu, M. S., *et al.*, 2012, Nat. Phys. **8**, 376.
Liu, T. J., *et al.*, 2010, Nat. Mater. **9**, 718.
Liu, Z.-H., *et al.*, 2011, Phys. Rev. B **84**, 064519.
Löhneysen, H. v., A. Rosch, M. Vojta, and P. Wölfle, 2007, Rev. Mod. Phys. **79**, 1015.
Lu, X. Y., J. T. Park, R. Zhang, H. Q. Luo, A. H. Nevidomskyy, Q. Si, and P. C. Dai, 2014, Science **345**, 657.
Lu, X. Y., *et al.*, 2013, Phys. Rev. Lett. **110**, 257001.
Lu, X. Y., *et al.*, 2014, Phys. Rev. B **90**, 024509.
Lumsden, M. D., and A. D. Christianson, 2010, J. Phys. Condens. Matter **22**, 203203.
Lumsden, M. D., *et al.*, 2009, Phys. Rev. Lett. **102**, 107005.
Lumsden, M. D., *et al.*, 2010, Nat. Phys. **6**, 182.
Luo, H. Q., X. Y. Lu, R. Zhang, M. Wang, E. A. Goremychkin, D. T. Adroja, S. Danilkin, G. C. Deng, Z. Yamani, and P. C. Dai, 2013, Phys. Rev. B **88**, 144516.
Luo, H. Q., M. Wang, C. L. Zhang, X. Y. Lu, L.-P. Regnault, R. Zhang, S. L. Li, J. P. Hu, and P. C. Dai, 2013, Phys. Rev. Lett. **111**, 107006.
Luo, H. Q., Z. Yamani, Y. C. Chen, X. Y. Lu, M. Wang, S. L. Li, T. A. Maier, S. Danilkin, D. T. Adroja, and P. C. Dai, 2012, Phys. Rev. B **86**, 024508.
Luo, H. Q., *et al.*, 2012, Phys. Rev. Lett. **108**, 247002.
Luo, Y. K., Y. K. Li, S. Jiang, J. H. Dai, G. H. Cao, and Z.-A. Xu, 2010, Phys. Rev. B **81**, 134422.
Lv, W., F. Krüger, and P. Phillips, 2010, Phys. Rev. B **82**, 045125.
Lv, W. C., A. Moreo, and E. Dagotto, 2014, Phys. Rev. B **89**, 104510.
Lv, W. C., J. S. Wu, and P. Phillips, 2009, Phys. Rev. B **80**, 224506.
Lynn, J. W., and P. C. Dai, 2009, Physica (Amsterdam) **469C**, 469.
Ma, F., and Z.-Y. Lu, 2008, Phys. Rev. B **78**, 033111.
Mackenzie, A. P., and Y. Maeno, 2003, Rev. Mod. Phys. **75**, 657.
Maier, T. A., S. Graser, P. J. Hirschfeld, and D. J. Scalapino, 2011, Phys. Rev. B **83**, 100515(R).
Maier, T. A., S. Graser, D. J. Scalapino, and P. Hirschfeld, 2009, Phys. Rev. B **79**, 134520.
Maier, T. A., and D. J. Scalapino, 2008, Phys. Rev. B **78**, 020514(R).
Mannella, N., 2014, J. Phys. Condens. Matter **26**, 473202.
Marty, K., A. D. Christianson, C. H. Wang, M. Matsuda, H. Cao, L. H. VanBebber, J. L. Zarestky, D. J. Singh, A. S. Sefat, and M. D. Lumsden, 2011, Phys. Rev. B **83**, 060509.
Matan, K., R. Morinaga, K. Iida, and T. J. Sato, 2009, Phys. Rev. B **79**, 054526.
Mathias, B. T., H. Suhl, and E. Corenzwit, 1958, Phys. Rev. Lett. **1**, 92.
May, A. F., M. A. McGuire, H. B. Cao, I. Sergueev, C. Cantoni, B. C. Chakoumakos, D. S. Parker, and B. C. Sales, 2012, Phys. Rev. Lett. **109**, 077003.
Mazin, I. I., 2010, Nature (London) **464**, 183.
Mazin, I. I., D. J. Singh, M. D. Johannes, and M. H. Du, 2008, Phys. Rev. Lett. **101**, 057003.
McGuire, M., *et al.*, 2008, Phys. Rev. B **78**, 094517.
McQueeney, R. J., *et al.*, 2008, Phys. Rev. Lett. **101**, 227205.
Mook, H. A., M. Yethiraj, G. Aeppli, T. E. Mason, and T. Armstrong, 1993, Phys. Rev. Lett. **70**, 3490.
Mook, H. A., *et al.*, 2010, Phys. Rev. Lett. **104**, 187002.
Moon, R. M., T. Riste, and W. C. Koehler, 1969, Phys. Rev. **181**, 920.
Moreo, A., M. Daghofer, J. A. Riera, and E. Dagotto, 2009, Phys. Rev. B **79**, 134502.
Mou, D., *et al.*, 2011, Phys. Rev. Lett. **106**, 107001.
Nakayama, K., *et al.*, 2010, Phys. Rev. Lett. **105**, 197001.
Nandi, S., *et al.*, 2010, Phys. Rev. Lett. **104**, 057006.
Ning, F. L., K. Ahilan, T. Imai, A. S. Sefat, R. Jin, M. A. McGuire, B. C. Sales, and D. Mandrus, 2008, J. Phys. Soc. Jpn. **77**, 103705.
Ning, F. L., K. Ahilan, T. Imai, A. S. Sefat, R. Jin, M. A. Mcquire, B. C. Sales, and D. Mandrus, 2009, J. Phys. Soc. Jpn. **78**, 013711.
Ning, F. L., K. Ahilan, T. Imai, A. S. Sefat, M. A. McGuire, B. C. Sales, D. Mandrus, P. Cheng, B. Shen, and H.-H. Wen, 2010, Phys. Rev. Lett. **104**, 037001.
Nomura, T., S. W. Kim, Y. Kamihara, M. Hirano, P. V. Sushko, K. Kato, M. Takata, A. L. Shluger, and H. Hosono, 2008, Supercond. Sci. Technol. **21**, 125028.
Oh, S., A. M. Mounce, S. Mukhopadhyay, W. P. Halperin, A. B. Vorontsov, S. L. Bud'ko, P. C. Canfield, Y. Furukawa, A. P. Reyes, and P. L. Kuhns, 2011, Phys. Rev. B **83**, 214501.
Ota, Y., *et al.*, 2014, Phys. Rev. B **89**, 081103(R).
Paglione, J., and R. L. Greene, 2010, Nat. Phys. **6**, 645.
Park, H., K. Haule, and G. Kotliar, 2011, Phys. Rev. Lett. **107**, 137007.
Park, J. T., *et al.*, 2010, Phys. Rev. B **82**, 134503.
Park, J. T., *et al.*, 2011, Phys. Rev. Lett. **107**, 177005.
Park, J. T., *et al.*, 2012, Phys. Rev. B **86**, 024437.
Parker, D. R., M. J. P. Smith, T. Lancaster, A. J. Steele, I. Franke, P. J. Baker, F. L. Pratt, M. J. Pitcher, S. J. Blundell, and S. J. Clarke, 2010, Phys. Rev. Lett. **104**, 057007.
Pitcher, M. J., D. R. Parker, P. Adamson, S. J. C. Herkelrath, A. T. Boothroyd, R. M. Ibberson, M. Brunelli, and S. J. Clarke, 2008, Chem. Commun. (Cambridge) **45**, 5918.
Plumb, K. W., A. T. Savici, G. E. Granroth, F. C. Chou, and Y.-J. Kim, 2014, Phys. Rev. B **89**, 180410(R).
Pramanik, A. K., M. Abdel-Hafiez, S. Aswartham, A. U. B. Wolter, S. Wurmehl, V. Kataev, and B. Büchner, 2011, Phys. Rev. B **84**, 064525.
Pratt, D. K., W. Tian, A. Kreyssig, J. L. Zarestky, S. Nandi, N. Ni, S. L. Bud'ko, P. C. Canfield, A. I. Goldman, and R. J. McQueeney, 2009, Phys. Rev. Lett. **103**, 087001.
Pratt, D. K., *et al.*, 2011, Phys. Rev. Lett. **106**, 257001.
Qazilbash, M. M., J. J. Hamlin, R. E. Baumbach, L. Zhang, D. J. Singh, M. B. Maple, and D. N. Basov, 2009, Nat. Phys. **5**, 647.
Qian, T., *et al.*, 2011, Phys. Rev. Lett. **106**, 187001.
Qiu, Y. M., *et al.*, 2008, Phys. Rev. Lett. **101**, 257002.
Qiu, Y. M., *et al.*, 2009, Phys. Rev. Lett. **103**, 067008.
Quirinale, D. G., *et al.*, 2013, Phys. Rev. B **88**, 174420.
Qureshi, N., Y. Drees, J. Werner, S. Wurmehl, C. Hess, R. Klingeler, B. Büchner, M. T. Fernández-Díaz, and M. Braden, 2010, Phys. Rev. B **82**, 184521.
Qureshi, N., C. H. Lee, K. Kihou, K. Schmalzl, P. Steffens, and M. Braden, 2014, Phys. Rev. B **90**, 100502(R).
Qureshi, N., P. Steffens, D. Lamago, Y. Sidis, O. Sobolev, R. A. Ewings, L. Harnagea, S. Wurmehl, B. Büchner, and M. Braden, 2014, Phys. Rev. B **90**, 144503.
Qureshi, N., P. Steffens, S. Wurmehl, S. Aswartham, B. Bchner, and M. Braden, 2012, Phys. Rev. B **86**, 060410(R).
Qureshi, N., *et al.*, 2012, Phys. Rev. Lett. **108**, 117001.
Ramazanoglu, M., *et al.*, 2013, Phys. Rev. B **87**, 140509(R).
Raymond, S., K. Kaneko, A. Hiess, P. Steffens, and G. Lapertot, 2012, Phys. Rev. Lett. **109**, 237210.
Ricci, A., *et al.*, 2011, Phys. Rev. B **84**, 060511.

Richard, P., T. Sato, K. Nakayama, T. Takahashi, and H. Ding, 2011, Rep. Prog. Phys. **74**, 124512.
Rodriguez, E. E., D. A. Sokolov, C. Stock, M. A. Green, O. Sobolev, J. A. Rodriguez-Rivera, H. Cao, and A. Daoud-Aladine, 2013, Phys. Rev. B **88**, 165110.
Rodriguez, E. E., C. Stock, P. Zajdel, K. L. Krycka, C. F. Majkrzak, P. Zavalij, and M. A. Green, 2011, Phys. Rev. B **84**, 064403.
Rodriguez, E. E., P. Zavalij, P.-Y. Hsieh, and M. A. Green, 2010, J. Am. Chem. Soc. **132**, 10006.
Rossat-Mignod, J., L. P. Regnault, C. Vettier, P. Bourges, P. Burlet, J. Bossy, J. Y. Henry, and G. Lapertot, 1991, Physica C (Amsterdam) **185–189**, 86.
Rotter, M., M. Tegel, and D. Johrendt, 2008, Phys. Rev. Lett. **101**, 107006.
Rotter, M., M. Tegel, I. Schellenberg, W. Hermes, R. Pöttgen, and D. Johrendt, 2008, Phys. Rev. B **78**, 020503(R).
Rowe, W., J. Knolle, I. Eremin, and P. J. Hirschfeld, 2012, Phys. Rev. B **86**, 134513.
Rueff, J.-P., and A. Shukla, 2010, Rev. Mod. Phys. **82**, 847.
Sadovskii, M. V., 2008, Phys. Usp. **51**, 1201.
Sato, N. K., N. Aso, K. Miyake, R. Shiina, P. Thalmeier, G. Varelogiannis, C. Geibel, F. Steglich, P. Fulde, and T. Komatsubara, 2001, Nature (London) **410**, 340.
Scalapino, D. J., 2012, Rev. Mod. Phys. **84**, 1383.
Scalapino, D. J., and S. R. White, 1998, Phys. Rev. B **58**, 8222.
Sefat, A. S., R. Jin, M. A. McGuire, B. C. Sales, D. J. Singh, and D. Mandrus, 2008, Phys. Rev. Lett. **101**, 117004.
Sefat, A. S., D. J. Singh, L. H. V. Bebber, Y. Mozharivskyj, M. A. McGuire, R. Jin, B. C. Sales, V. Keppens, and D. Mandrus, 2009, Phys. Rev. B **79**, 224524.
Shamoto, S., M. Ishikado, A. D. Christianson, M. D. Lumsden, S. Wakimoto, K. Kodama, A. Iyo, and M. Arai, 2010, Phys. Rev. B **82**, 172508.
Shermadini, Z., H. Luetkens, R. Khasanov, A. Krzton-Maziopa, K. Conder, E. Pomjakushina, H.-H. Klauss, and A. Amato, 2012, Phys. Rev. B **85**, 100501(R).
Shibauchi, T., A. Carrington, and Y. Matsuda, 2014, Annu. Rev. Condens. Matter Phys. **5**, 113.
Shoemaker, D. P., D. Y. Chung, H. Claus, M. C. Francisco, S. Avci, A. Llobet, and M. G. Kanatzidis, 2012, Phys. Rev. B **86**, 184511.
Shull, C. G., and F. A. Wedgewood, 1966, Phys. Rev. Lett. **16**, 513.
Si, Q., and E. Abrahams, 2008, Phys. Rev. Lett. **101**, 076401.
Sidis, Y., *et al.*, 2000, Phys. Rev. Lett. **84**, 5900.
Simonson, J. W., *et al.*, 2012, Proc. Natl. Acad. Sci. U.S.A. **109**, E1815.
Singh, Y., M. A. Green, Q. Huang, A. Kreyssig, R. J. McQueeney, D. C. Johnston, and A. I. Goldman, 2009, Phys. Rev. B **80**, 100403(R).
Soh, J. H., *et al.*, 2013, Phys. Rev. Lett. **111**, 227002.
Song, Y., S. V. Carr, X. Y. Lu, C. L. Zhang, Z. C. Sims, N. F. Luttrell, S. Chi, Y. Zhao, J. W. Lynn, and P. C. Dai, 2013, Phys. Rev. B **87**, 184511.
Song, Y., L.-P. Regnault, C. L. Zhang, G. T. Tan, S. V. Carr, S. X. Chi, A. D. Christianson, T. Xiang, and P. C. Dai, 2013, Phys. Rev. B **88**, 134512.
Speller, S. C., T. B. Britton, G. M. Hughes, A. Krzton-Maziopa, E. Pomjakushina, K. Conder, A. T. Boothroyd, and C. R. M. Grovenor, 2012, Supercond. Sci. Technol. **25**, 084023.
Steffens, P., C. H. Lee, N. Qureshi, K. Kihou, A. Iyo, H. Eisaki, and M. Braden, 2013, Phys. Rev. Lett. **110**, 137001.
Steglich, F., J. Aarts, C. D. Bredl, W. Lieke, D. Meschede, W. Franz, and H. Schafer, 1979, Phys. Rev. Lett. **43**, 1892.
Stewart, G. R., 2001, Rev. Mod. Phys. **73**, 797.
Stewart, G. R., 2011, Rev. Mod. Phys. **83**, 1589.
Stock, C., C. Broholm, J. Hudis, H. J. Kang, and C. Petrovic, 2008, Phys. Rev. Lett. **100**, 087001.
Stock, C., C. Broholm, Y. Zhao, F. Demmel, H. J. Kang, K. C. Rule, and C. Petrovic, 2012, Phys. Rev. Lett. **109**, 167207.
Stock, C., R. A. Cowley, W. J. L. Buyers, C. D. Frost, J. W. Taylor, D. Peets, R. Liang, D. Bonn, and W. N. Hardy, 2010a, Phys. Rev. B **82**, 174505.
Stock, C., R. A. Cowley, W. J. L. Buyers, C. D. Frost, J. W. Taylor, D. Peets, R. Liang, D. Bonn, and W. N. Hardy, 2010b, Phys. Rev. B **82**, 174505.
Stock, C., E. E. Rodriguez, M. A. Green, P. Zavalij, and J. A. Rodriguez-Rivera, 2011, Phys. Rev. B **84**, 045124.
Stock, C., E. E. Rodriguez, O. Sobolev, J. A. Rodriguez-Rivera, R. A. Ewings, J. W. Taylor, A. D. Christianson, and M. A. Green, 2014, Phys. Rev. B **90**, 121113(R).
Stockert, O., *et al.*, 2011, Nat. Phys. **7**, 119.
Subedi, A., L. J. Zhang, D. J. Singh, and M. H. Du, 2008, Phys. Rev. B **78**, 134514.
Suchaneck, A., *et al.*, 2010, Phys. Rev. Lett. **105**, 037207.
Tacon, M. L., *et al.*, 2011, Nat. Phys. **7**, 725.
Tafti, F. F., A. Juneau-Fecteau, M.-È. Delage, S. R. de Cotret, J.-P. Reid, A. F. Wang, X.-G. Luo, X. H. Chen, N. Doiron-Leyraud, and L. Taillefer, 2013, Nat. Phys. **9**, 349.
Tan, G. T., *et al.*, 2013, Phys. Rev. B **87**, 144512.
Tanatar, M. A., N. Spyrison, K. Cho, E. C. Blomberg, G. T. Tan, P. C. Dai, C. L. Zhang, and R. Prozorov, 2012, Phys. Rev. B **85**, 014510.
Tanatar, M. A., *et al.*, 2010, Phys. Rev. B **81**, 184508.
Tapp, J. H., Z. J. Tang, B. Lv, K. Sasmal, B. Lorenz, P. C. W. Chu, and A. M. Guloy, 2008, Phys. Rev. B **78**, 060505(R).
Taylor, A. E., R. A. Ewings, T. G. Perring, J. S. White, P. Babkevich, A. Krzton-Maziopa, E. Pomjakushina, K. Conder, and A. T. Boothroyd, 2012, Phys. Rev. B **86**, 094528.
Taylor, A. E., M. J. Pitcher, R. A. Ewings, T. G. Perring, S. J. Clarke, and A. T. Boothroyd, 2011, Phys. Rev. B **83**, 220514(R).
Taylor, A. E., S. J. Sedlmaier, S. J. Cassidy, E. A. Goremychkin, R. A. Ewings, T. G. Perring, S. J. Clarke, and A. T. Boothroyd, 2013, Phys. Rev. B **87**, 220508(R).
Texier, Y., J. Deisenhofer, V. Tsurkan, A. Loidl, D. S. Inosov, G. Friemel, and J. Bobroff, 2012, Phys. Rev. Lett. **108**, 237002.
Thaler, A., H. Hodovanets, M. S. Torikachvili, S. Ran, A. Kracher, W. Straszheim, J. Q. Yan, E. Mun, and P. C. Canfield, 2011, Phys. Rev. B **84**, 144528.
Thaler, A., N. Ni, A. Kracher, J. Q. Yan, S. L. Bud'ko, and P. C. Canfield, 2010, Phys. Rev. B **82**, 014534.
Thompson, J. D., and Z. Fisk, 2012, J. Phys. Soc. Jpn. **81**, 011002.
Tranquada, J. M., G. Xu, and I. A. Zaliznyak, 2014, J. Magn. Magn. Mater. **350**, 148.
Tranquada, J. M., *et al.*, 1988, Phys. Rev. Lett. **60**, 156.
Tucker, G. S., *et al.*, 2012a, Phys. Rev. B **86**, 024505.
Tucker, G. S., *et al.*, 2012b, Phys. Rev. B **86**, 020503(R).
Uemura, Y. J., 2009, Nat. Mater. **8**, 253.
Vaknin, D., S. K. Sinha, D. E. Moncton, D. C. Johnston, J. M. Newsam, C. R. Safinya, and J. H. E. King, 1987, Phys. Rev. Lett. **58**, 2802.
Vilmercati, P., *et al.*, 2012, Phys. Rev. B **85**, 220503(R).
Vorontsov, A. B., M. G. Vavilov, and A. V. Chubukov, 2009, Phys. Rev. B **79**, 060508(R).
Wakimoto, S., K. Yamada, J. M. Tranquada, C. D. Frost, R. J. Birgeneau, and H. Zhang, 2007, Phys. Rev. Lett. **98**, 247003.
Wakimoto, S., *et al.*, 2010, J. Phys. Soc. Jpn. **79**, 074715.
Wang, C., R. Zhang, F. Wang, H. Q. Luo, L. P. Regnault, P. C. Dai, and Y. Li, 2013, Phys. Rev. X **3**, 041036.
Wang, F., and D. H. Lee, 2011, Science **332**, 200.

Wang, F., F. Yang, M. Gao, Z.-Y. Lu, T. Xiang, and D.-H. Lee, 2011, Europhys. Lett. **93**, 57003.
Wang, M., W. Tian, P. Valdivia, S. X. Chi, E. Bourrret-Courchesne, P. C. Dai, and R. J. Birgeneau, 2014, Phys. Rev. B **90**, 125148.
Wang, M., *et al.*, 2011, Phys. Rev. B **84**, 094504.
Wang, M., *et al.*, 2012, Phys. Rev. B **86**, 144511.
Wang, M., *et al.*, 2013, Nat. Commun. **4**, 2874.
Wang, M. Y., H. Q. Luo, M. Wang, S. X. Chi, J. A. Rodriguez-Rivera, D. Singh, S. Chang, J. W. Lynn, and P. C. Dai, 2011, Phys. Rev. B **83**, 094516.
Wang, M. Y., *et al.*, 2010, Phys. Rev. B **81**, 174524.
Wang, M. Y., *et al.*, 2011, Nat. Commun. **2**, 580.
Wang, M. Y., *et al.*, 2012, Phys. Rev. B **86**, 024502.
Wang, X. C., Q. Q. Liu, Y. X. Lv, W. B. Gao, L. X. Yang, R. C. Yu, F. Y. Li, and C. Q. Jin, 2008, Solid State Commun. **148**, 538.
Wang, Z. W., Z. Wang, Y. J. Song, C. Ma, Y. Cai, Z. Chen, H. F. Tian, H. X. Yang, G. F. Chen, and J. Q. Li, 2012, J. Phys. Chem. C **116**, 17847.
Wen, J., *et al.*, 2013, Phys. Rev. B **88**, 144509.
Wen, J. S., G. Y. Xu, G. D. Gu, J. M. Tranquada, and R. J. Birgeneau, 2011, Rep. Prog. Phys. **74**, 124503.
Wen, J. S., G. Y. Xu, Z. J. Xu, Z. W. Lin, Q. Li, Y. Chen, S. X. Chi, G. D. Gu, and J. M. Tranquada, 2010, Phys. Rev. B **81**, 100513(R).
Wilson, S. D., P. C. Dai, S. L. Li, S. X. Chi, H. J. Kang, and J. W. Lynn, 2006, Nature (London) **442**, 59.
Wilson, S. D., S. L. Li, H. Woo, P. C. Dai, H. A. Mook, C. D. Frost, S. Komiya, and Y. Ando, 2006, Phys. Rev. Lett. **96**, 157001.
Wollan, E. O., and W. C. Koehler, 1955, Phys. Rev. **100**, 545.
Woo, H., P. C. Dai, S. M. Hayden, H. A. Mook, T. Dahm, D. J. Scalapino, T. G. Perring, and F. Doğan, 2006, Nat. Phys. **2**, 600.
Wysocki, A. L., K. D. Belashchenko, and V. P. Antropov, 2011, Nat. Phys. **7**, 485.
Xiao, Y., *et al.*, 2013, Phys. Rev. B **87**, 140408.
Xu, C. K., M. Müller, and S. Sachdev, 2008, Phys. Rev. B **78**, 020501.
Xu, G. Y., Z. J. Xu, and J. M. Tranquada, 2013, Rev. Sci. Instrum. **84**, 083906.
Xu, N., *et al.*, 2013, Phys. Rev. X **3**, 011006.
Xu, Z., *et al.*, 2012, Phys. Rev. Lett. **109**, 227002.
Xu, Z. J., J. S. Wen, G. Y. Xu, Q. Jie, Z. W. Lin, Q. Li, S. X. Chi, D. K. Singh, G. D. Gu, and J. M. Tranquada, 2010, Phys. Rev. B **82**, 104525.
Yang, F., S.-P. Kou, and Z.-Y. Weng, 2010, Phys. Rev. B **81**, 245130.
Ye, F., S. X. Chi, W. Bao, X. F. Wang, J. J. Ying, X. H. Chen, H. D. Wang, C. H. Dong, and M. H. Fang, 2011, Phys. Rev. Lett. **107**, 137003.
Yi, M., *et al.*, 2011, Proc. Natl. Acad. Sci. U.S.A. **108**, 6878.
Yildirim, T., 2008, Phys. Rev. Lett. **101**, 057010.
Yin, W.-G., C.-C. Lee, and W. Ku, 2010, Phys. Rev. Lett. **105**, 107004.
Yin, Z. P., K. Haule, and G. Kotliar, 2011, Nat. Mater. **10**, 932.
Yin, Z. P., K. Haule, and G. Kotliar, 2014, Nat. Phys. **10**, 845.
Ying, T. P., X. L. Chen, G. Wang, S. F. Jin, T. T. Zhou, X. F. Lai, H. Zhang, and W. Y. Wang, 2012, Sci. Rep. **2**, 426.
Yoshizawa, M., *et al.*, 2012, J. Phys. Soc. Jpn. **81**, 024604.
You, Y.-Z., F. Yang, S.-P. Kou, and Z.-Y. Weng, 2011, Phys. Rev. B **84**, 054527.
Yu, G., Y. Li, E. M. Motoyama, and M. Greven, 2009, Nat. Phys. **5**, 873.
Yu, R., Q. Si, P. Goswami, and E. Abrahams, 2013, J. Phys. Conf. Ser. **449**, 012025.
Yu, R., Z. Wang, P. Goswami, A. H. Nevidomskyy, Q. Si, and E. Abrahams, 2012, Phys. Rev. B **86**, 085148.
Yu, R., J. X. Zhu, and Q. Si, 2014, Phys. Rev. B **89**, 024509.
Zaliznyak, I. A., Z. J. Xu, J. M. Tranquada, G. D. Gu, A. M. Tsvelik, and M. B. Stone, 2011, Phys. Rev. Lett. **107**, 216403.
Zhang, C. L., M. S. Liu, Y. X. Su, L.-P. Regnault, M. Wang, G. T. Tan, T. Brückel, T. Egami, and P. C. Dai, 2013, Phys. Rev. B **87**, 081101(R).
Zhang, C. L., *et al.*, 2011, Sci. Rep. **1**, 115.
Zhang, C. L., *et al.*, 2013a, Phys. Rev. B **88**, 064504.
Zhang, C. L., *et al.*, 2013b, Phys. Rev. Lett. **111**, 207002.
Zhang, C. L., *et al.*, 2014a, Phys. Rev. Lett. **112**, 217202.
Zhang, C. L., *et al.*, 2014b, Phys. Rev. B **90**, 140502(R).
Zhang, J. H., R. Sknepnek, and J. Schmalian, 2010, Phys. Rev. B **82**, 134527.
Zhang, Q., *et al.*, 2013, Phys. Rev. B **88**, 174517.
Zhang, Y., *et al.*, 2011, Nat. Mater. **10**, 273.
Zhang, Y., *et al.*, 2012, Phys. Rev. B **85**, 085121.
Zhao, J., D. T. Adroja, D.-X. Yao, R. Bewley, S. L. Li, X. F. Wang, G. Wu, X. H. Chen, J. P. Hu, and P. C. Dai, 2009, Nat. Phys. **5**, 555.
Zhao, J., H. B. Cao, E. Bourret-Courchesne, D. H. Lee, and R. J. Birgeneau, 2012, Phys. Rev. Lett. **109**, 267003.
Zhao, J., W. Ratcliff-II, J. W. Lynn, G. Chen, J. L. Luo, N. Wang, J. Hu, and P. C. Dai, 2008, Phys. Rev. B **78**, 140504(R).
Zhao, J., L. P. Regnault, C. L. Zhang, M. Y. Wang, Z. C. Li, F. Zhou, Z. X. Zhao, C. Fang, J. P. Hu, and P. C. Dai, 2010, Phys. Rev. B **81**, 180505(R).
Zhao, J., C. R. Rotundu, K. Marty, M. Matsuda, Y. Zhao, C. Setty, E. Bourret-Courchesne, J. P. Hu, and R. J. Birgeneau, 2013, Phys. Rev. Lett. **110**, 147003.
Zhao, J., Y. Shen, R. J. Birgeneau, M. Gao, Z.-Y. Lu, D.-H. Lee, X. Lu, H. Xiang, D. Abernathy, and Y. Zhao, 2014, Phys. Rev. Lett. **112**, 177002.
Zhao, J., *et al.*, 2008a, Phys. Rev. Lett. **101**, 167203.
Zhao, J., *et al.*, 2008b, Nat. Mater. **7**, 953.
Zhao, J., *et al.*, 2008c, Phys. Rev. B **78**, 132504.
Zhou, K.-J., *et al.*, 2013, Nat. Commun. **4**, 1470.
Zhou, R., Z. Li, J. Yang, D. L. Sun, C. T. Lin, and G.-Q. Zheng, 2013, Nat. Commun. **4**, 2265.